



EXPERIMENTAL INVESTIGATION OF A SUPERSONIC  
TURBULENT BOUNDARY LAYER  
WITH ADVERSE PRESSURE GRADIENT

THESIS  
Chad S. Hale, B.S.  
Second Lieutenant, USAF

AFIT/GAE/ENY/95D-12

DISTRIBUTION STATEMENT A

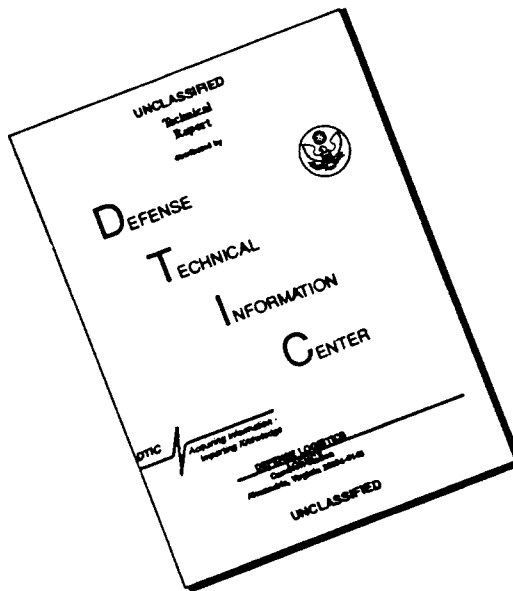
Approved for public release  
Distribution Unlimited

DTIC QUALITY INSPECTED 3

DEPARTMENT OF THE AIR FORCE  
AIR UNIVERSITY  
**AIR FORCE INSTITUTE OF TECHNOLOGY**

Wright-Patterson Air Force Base, Ohio

# **DISCLAIMER NOTICE**



**THIS DOCUMENT IS BEST  
QUALITY AVAILABLE. THE COPY  
FURNISHED TO DTIC CONTAINED  
A SIGNIFICANT NUMBER OF  
PAGES WHICH DO NOT  
REPRODUCE LEGIBLY.**

EXPERIMENTAL INVESTIGATION OF A SUPERSONIC  
TURBULENT BOUNDARY LAYER  
WITH ADVERSE PRESSURE GRADIENT

THESIS  
Chad S. Hale, B.S.  
Second Lieutenant, USAF

AFIT/GAE/ENY/95D-12

19960611 026

DTIC QUALITY INSPECTED 3

The views expressed in this thesis are those of the author  
and do not reflect the official policy or position of the  
Department of Defense or the U. S. Government.

AFIT/GAE/ENY/95D-12

EXPERIMENTAL INVESTIGATION OF A SUPERSONIC  
TURBULENT BOUNDARY LAYER  
WITH  
ADVERSE PRESSURE GRADIENT

THESIS

Presented to the Faculty of the School of Engineering  
of the Air Force Institute of Technology  
Air University  
In Partial Fulfillment of the  
Requirements for the Degree of  
Master of Science in Aeronautical Engineering

Chad S. Hale, B.S.  
Second Lieutenant, USAF

December 1995

Approved for public release; distribution is unlimited

### *Acknowledgments*

To all those who have helped me with this project, I salute you and give you my most heartfelt thanks. I'd especially like to thank Dr. Rodney Bowersox for his unending support and encouragement. Your enthusiasm and drive for accurate LDV measurements have helped to make this research project more meaningful than I had ever imagined. Thanks for calling Joel and me the "AFIT resident experts in LDV." Your encouragement was greatly appreciated. Thanks also goes to the other members of the reading committee, Major Tom Buter and Dr. Milton Franke, for the insights and advice you've provided. Special thanks also goes to Mr. Jay Anderson, and his crew of laboratory technicians, for their diligence and practical "know how". Believe it or not, we didn't damage the expensive LDV system like you thought we would. I'd like to thank Lt. Joel Luker for his incredible help, and for making my LDV measurements while I was off becoming a father.

Most of all, I'd like to thank my patient and understanding wife, Camille, and good-natured daughter, Taylor. I love you and have greatly appreciated your incredible support. Yes, Camille, I'm married to you, and *not* the home computer. You and Taylor have given me great encouragement to finish when I could see the light at the end of the tunnel drawing closer, but felt like the tunnel was caving in around me much faster. Also, thanks goes out to Mom and Dad for the example that you have given me. I've appreciated your love, support, and encouragement. I want to thank you all for encouraging me to apply for the Air Force Institute of Technology even when I was told that ROTC cadets couldn't go to AFIT right after graduation and commissioning.

Chad S. Hale

*Table of Contents*

	Page
<i>Acknowledgments</i> .....	ii
<i>List of Figures</i> .....	vii
<i>List of Tables</i> .....	x
<i>List of Symbols</i> .....	xi
<i>Abstract</i> .....	xiv
<b>1. Introduction</b> .....	<b>1-1</b>
1.1 Background.....	1-1
1.2 Objectives.....	1-3
1.3 Settles and Dodson Criteria.....	1-3
1.4 Synopsis of the Present Investigation.....	1-4
<b>2. Turbulence Analysis</b> .....	<b>2-1</b>
2.1 Governing Equations (Navier-Stokes Equations) .....	2-1
2.2 Reynolds-Averaged Navier-Stokes (RANS) Equations .....	2-2
2.3 Favre-Averaged Navier-Stokes (FANS) Equations.....	2-4
2.4 RANS & FANS Relationship.....	2-5
<b>3. Principles of Laser Doppler Velocimetry</b> .....	<b>3-1</b>
3.1 Overview .....	3-1
3.2 Probe Volume & Interference Pattern.....	3-2
3.3 Calculation of Velocity .....	3-3
3.4 Overcoming Directional Ambiguity .....	3-6
3.5 Validation of Particles .....	3-6

3.5.1 Fringe Count.....	3-7
3.5.2 Particle Acceleration .....	3-7
3.5.3 Spectrum Validation.....	3-7
3.5.4 Doppler Signal Validation.....	3-8
3.6 Coincidence Window .....	3-9
3.7 Forward- vs. Back-Scattering Method.....	3-10
3.8 Seeding Considerations .....	3-11
3.9 Optical Alignment .....	3-12
<b>4. Test Facilities and Equipment .....</b>	<b>4-1</b>
4.1 Wind Tunnel Facilities .....	4-1
4.1.1 Plenum Chamber .....	4-2
4.1.2 Air Supply .....	4-2
4.1.3 Supersonic Nozzle .....	4-2
4.1.4 Test Section .....	4-3
4.2 Laser Doppler Velocimetry System .....	4-5
4.2.1 FiberFlow System.....	4-5
4.2.2 Dantec 3D Traverse System .....	4-9
4.2.3 Burst Spectrum Analyzers.....	4-10
4.2.4 PC Computer and BURSTware Software .....	4-10
4.3 Seeder Apparatus.....	4-11
4.4 Flow Visualization .....	4-12
4.5 Computer Resources.....	4-13
4.5.1 Personal Computer .....	4-13
4.5.2 AFIT Computer Resources.....	4-13

<b>5. Experimental Procedures .....</b>	<b>5-1</b>
5.1 Traverse Positioning.....	5-1
5.2 Optical Alignment .....	5-1
5.2.1 Forward-scatter Mode .....	5-2
5.2.2 Optical Axis Alignment.....	5-3
5.2.3 Establishment of Data Profile Origin .....	5-4
5.2.4 Laser Intersection Adjustment.....	5-5
5.3 BURSTware Configuration .....	5-6
5.3.1 Parameter Files .....	5-6
5.3.2 BURSTware Menu Settings .....	5-6
5.3.3 BURSTware Post-processing .....	5-11
5.4 Overview of a Typical Data Profile .....	5-12
<b>6. Data Reduction Procedures .....</b>	<b>6-1</b>
6.1 Calculation of Velocity .....	6-1
6.2 Calculation of Mach Number, Temperature, Density, and Pressure.....	6-1
6.3 Calculation of Boundary Layer, Displacement, and Momentum Thickness.....	6-5
6.4 Calculation of Turbulent Statistics.....	6-5
6.5 Calculation of Wall Shear Stress.....	6-9
6.6 Calculation of Van Driest Velocity Profile.....	6-9
6.7 Calculation of Strain Rates.....	6-11
<b>7. Experimental Results .....</b>	<b>7-1</b>
7.1 Flat Plate Results .....	7-1
7.1.1 Flat Plate Mean Flow Results.....	7-2
7.1.2 Flat Plate Turbulence Results.....	7-5

7.1.2.1 Flat Plate Turbulence Intensities .....	7-5
7.1.2.2 Flat Plate Reynolds Shear Stress .....	7-7
7.2 Pressure Gradient Results.....	7-10
7.2.1 Flow Visualization .....	7-10
7.2.2 Wall Pressure Distribution and Temperature .....	7-11
7.2.3 Pressure Gradient vs. Flat Plate Mean Flow Results .....	7-13
7.2.4 Pressure Gradient vs. Flat Plate Turbulence Results.....	7-19
7.2.4.1 Turbulence Intensities .....	7-19
7.2.4.2 Reynolds Shear Stresses .....	7-21
7.2.4.3 Skin Friction Estimates.....	7-24
7.2.4.4 Intermittency Function .....	7-24
7.2.4.5 Flatness and Skewness .....	7-26
7.2.4.6 Velocity-Velocity Correlation Coefficient and TKE .....	7-28
7.2.5 Pressure Gradient vs. Flat Plate Strain Rates .....	7-30
<b>8. Conclusions and Recommendations.....</b>	<b>8-1</b>
<i>Appendix A: Error Analysis.....</i>	<b>A-1</b>
<i>Appendix B: Data Files .....</i>	<b>B-1</b>
<i>Appendix C: LDV and Flow Field Quality Analysis.....</i>	<b>C-1</b>
<i>Appendix D: CFD Validation.....</i>	<b>D-1</b>
<i>Bibliography .....</i>	<b>BIB-1</b>
<i>Vita .....</i>	<b>VITA</b>

*List of Figures*

	Page
Figure 1-1: Flow Over Compression Ramp Model .....	1-5
Figure 3-1: Fringe Disks of Probe Volume .....	3-2
Figure 3-2: Laser Beam Intersection Pattern.....	3-3
Figure 3-3: Doppler Burst .....	3-4
Figure 3-4: Spectrum Validation .....	3-8
Figure 3-5: Envelope and Pedestal Generation .....	3-9
Figure 3-6: Scattered Light Intensity.....	3-10
Figure 3-7: Magnitude of Light Intensity .....	3-11
Figure 3-8: Possible Optical Alignments .....	3-13
Figure 4-1: AFIT Mach 3.0 Tunnel Schematic .....	4-1
Figure 4-2: Mach 3.0 Nozzle .....	4-3
Figure 4-3: Compression Ramp Model with Test Section .....	4-4
Figure 4-4: Possible Window Configurations .....	4-5
Figure 4-5: Laser Source and FiberFlow System .....	4-7
Figure 4-6: 1D Probe with Adjustable Base.....	4-8
Figure 4-7: 3D Traverse with Probes .....	4-9
Figure 4-8: Six-jet Atomizer and Injector Schematic.....	4-11
Figure 4-9: Shadowgraph and Schlieren Setup .....	4-12
Figure 5-1: Forward-scattering Configuration .....	5-2
Figure 5-2: Data Profile Origin .....	5-4
Figure 6-1: Finite-Difference Grid .....	6-11
Figure 7-1: Flat Plate Velocity Profile, $x = 44$ and $71$ cm .....	7-3

Figure 7-2: Flat Plate Non-dimensional Velocity Profiles, $x = 44$ and $71$ cm .....	7-4
Figure 7-3: Flat Plate Mach Number Profiles, $x = 44$ and $71$ cm .....	7-5
Figure 7-4: Flat Plate $u$ -component Turbulence Intensities .....	7-6
Figure 7-5: Flat Plate $v$ -component Turbulence Intensities .....	7-7
Figure 7-6: Flat Plate Turbulent Shear Stress .....	7-8
Figure 7-7: Flat Plate Intermittency Function .....	7-9
Figure 7-8: Shadowgraph of APG Region .....	7-12
Figure 7-9: Horizontal Knife Edge Schlieren Photograph .....	7-12
Figure 7-10: Vertical Knife Edge Schlieren Photograph .....	7-12
Figure 7-11: Compression Ramp Surface Pressure Distribution .....	7-13
Figure 7-12: Pressure Gradient vs. Flat Plate $\bar{u}$ Velocity .....	7-15
Figure 7-13: Pressure Gradient vs. Flat Plate $u/u_e$ Profile .....	7-15
Figure 7-14: Pressure Gradient vs. Flat Plate Density .....	7-16
Figure 7-15: Pressure Gradient vs. Flat Plate Mach Number.....	7-17
Figure 7-16: Van Driest Velocity Profile .....	7-18
Figure 7-17: Pressure Gradient vs. Flat Plate $u$ -component Turbulence Intensities .....	7-20
Figure 7-18: Pressure Gradient vs. Flat Plate $v$ -component Turbulence Intensities .....	7-21
Figure 7-19: Reynolds Shear Stress .....	7-23
Figure 7-20: Reynolds Shear Stress .....	7-23
Figure 7-21: Pressure Gradient Intermittency Function .....	7-25
Figure 7-22: Pressure Gradient vs. Flat Plate $u$ -component Flatness.....	7-26
Figure 7-23: Pressure Gradient vs. Flat Plate $u$ -component Skewness .....	7-27
Figure 7-24: Pressure Gradient vs. Flat Plate $v$ -component Flatness.....	7-27
Figure 7-25: Pressure Gradient vs. Flat Plate $v$ -component Skewness .....	7-28

Figure 7-26: Velocity-Velocity Correlation Coefficient .....	7-29
Figure 7-27: Pressure Gradient vs. Flat Plate TKE .....	7-30
Figure 7-28: $du/dx$ Strain Rate Comparison .....	7-31
Figure 7-29: $du/dy$ Strain Rate Comparison .....	7-32
Figure 7-30: Simple Turbulence Model .....	7-33
Figure 7-31: $dv/dx$ Strain Rate Comparison .....	7-34
Figure 7-32: $dv/dy$ Strain Rate Comparison .....	7-34
Figure C-1: Record Length Influence on Mach Number .....	C-2
Figure C-2: Record Length Influence on Turbulence Intensity .....	C-2
Figure C-3: Raw vs. Coincident Mach Number .....	C-4
Figure C-4: Raw vs. Coincident Turbulence Intensities .....	C-4
Figure C-5: 2D Comparison of Velocity Profiles.....	C-5
Figure C-6: 2D Comparison of Turbulent Shear Stresses .....	C-6
Figure C-7: Velocity Profile Repeatability Comparison .....	C-8
Figure C-8: Turbulent Shear Stress Repeatability Comparison .....	C-8
Figure D-1: LDV vs. CFD Velocity Profile .....	D-1
Figure D-2: LDV vs. CFD Turbulent Shear Stress .....	D-2

*List of Tables*

	Page
Table 5-1: BURSTware Optical Menu Settings.....	5-7
Table 5-2: Control Volume Measurements Settings .....	5-7
Table 5-3: Sample Traverse Coordinates .....	5-8
Table 5-4: BURSTware Quick Menu Settings.....	5-9
Table 5-5: BURSTware Program Menu Settings .....	5-10
Table 5-6: BURSTware Softkey Menu Settings .....	5-11
Table 7-1: Boundary Layer Edge Conditions.....	7-1
Table 7-2: Flat Plate Boundary Layer Thickness .....	7-10
Table 7-3: Pressure Gradient Boundary Layer Thickness.....	7-19
Table 7-4: Skin Friction Estimates.....	7-24
Table A-1: Repeatability Velocity Errors .....	A-3
Table A-2: LDV Velocity Errors.....	A-3
Table A-3: Error Summary .....	A-5
Table B-1: Tabulated Data by Figure Number.....	B-1
Table B-2: Flat Plate, $x = 44$ cm .....	B-2
Table B-3: Flat Plate, $x = 71$ cm (Part 1) .....	B-3
Table B-4: Flat Plate, $x = 71$ cm (Part 2) .....	B-4
Table B-5: Flat Plate, $x = 71$ cm, 8 Samples .....	B-5
Table B-6: Adverse Pressure Gradient, $x = 68$ cm.....	B-6
Table B-7: Adverse Pressure Gradient, $x = 71$ cm.....	B-7
Table B-8: APG, $x = 71$ cm, Single Component .....	B-8
Table C-1: Repeatability Confidence Intervals .....	C-7

*List of Symbols*

English

BW	Bandwidth
C	Coefficient
d	Distance
	Diameter
h	Enthalpy
k	Thermal conductivity
M	Mach number
m	Mass
N	Record length
Pr	Prandtl number
p	Pressure
Q	Total velocity
q	Heat flux
R	Gas constant
Re	Reynolds number
Re/m	Reynolds number per meter
r	Recovery factor
T	Temperature
	Period
TKE	Turbulent kinetic energy

$t$	Time
$u, v$	Velocity components (Cartesian)
$x, y, z$	Cartesian coordinates
$Y$	Model height from flat plate

### Greek

$\beta$	Clauser pressure gradient parameter
$\delta$	Boundary layer thickness
$\delta_{ij}$	Kronecker delta
$\phi$	Optical rotation angle
$\gamma$	Ratio of specific heats
	Intermittency function
$\lambda$	Laser wavelength
$\mu$	Viscosity
$\Theta$	Momentum thickness
$\theta$	Beam separation angle
	Probe off-axis angle
$\rho$	Density
$\tau$	Shear stress

### Subscripts

$\infty$	Freestream condition
----------	----------------------

aw	Adiabatic wall
B	Bragg cell
D	Doppler
e	Boundary layer edge quantities
f	Fringe
i	Incompressible
i,j,k	Indicial notation
o	Reference condition
w	Wall

#### Superscripts

$( )^F$	Favre averaged quantity
$( )''$	Favre fluctuating component
$\tilde{( )}$	Favre mean component
$( )^R$	Reynolds averaged quantity
$( )'$	Reynolds fluctuating component
$\overline{( )}$	Reynolds mean component
$( )^T$	Turbulent

*Abstract*

EXPERIMENTAL INVESTIGATION OF A SUPERSONIC TURBULENT BOUNDARY  
LAYER WITH ADVERSE PRESSURE GRADIENT

Laser Doppler Velocimetry (LDV) measurements were made to quantify the effect of adverse pressure gradient on the compressible turbulent flow structure in a Mach 2.9 boundary layer ( $Re/m = 1.75 \times 10^7$ ). Measurements included profiles of 2-D mean velocities, turbulence intensities, Reynolds shear stresses, intermittency, flatness and skewness. In addition, mean strain rates were also measured. The boundary layer measurements were acquired for both flat plate and compression ramp models. LDV measurements were made at two locations on the compression ramp model at 68 cm and 71 cm downstream of the nozzle throat. At these locations,  $\beta \approx 1.12$  and -0.94, respectively. Flow visualization was accomplished by nanosecond shadowgraph and schlieren photography. Results indicate that the adverse pressure gradient increased the Reynolds shear stresses by 190% and turbulence intensities by 24% of the flat plate values. In the favorable pressure gradient region, these quantities were decreased by 52% and 7% with respect to the adverse pressure gradient values, respectively.

# **Experimental Investigation of a Supersonic Turbulent Boundary Layer with Adverse Pressure Gradient**

## *1. Introduction*

### *1.1 Background*

The study of aerodynamics has been improved by the numerical capabilities of present day computers to model, or simulate, naturally occurring flow structures. Computational fluid dynamics (CFD) creates a mathematical model that approximates these flow structures. By using numerical methods, many flow structures may be evaluated without the necessity of building a model, and performing wind tunnel experiments. Turbulent flow, which can be characterized by the unsteady Navier-Stokes equations, is usually present when flows have high Reynolds numbers. Due to the large variation in the spatial and temporal length scales of the turbulent flow structure, closed form solutions to practical high Reynolds number problems are not possible. Current computational capabilities are not able to handle these problems within a reasonable amount of time. For example, flow over a cylinder of  $Re_D = 10^7$  would require  $10^{22}$  numerical operations. A computer that is capable of one operation per nanosecond would require 320,000 years to complete this analysis [34]. Thus, turbulent flow solutions are typically derived from time-averaged approximations, such as the Reynolds and Favre averaging methods. The time-averaged form of the governing equations is solved by casting the dependent variables into the sum of a mean and fluctuating component. Because of the non-linear terms in the unsteady Navier-Stokes equations, this process introduces additional cross-correlations of

fluctuating terms, resulting in more unknowns than governing equations. Turbulence modeling attempts to relate these new terms to other flow parameters to provide enough equations to close the system.

Wilcox [35] has stated that “an ideal model should introduce the minimum amount of complexity while capturing the essence of the relevant physics.” In the past, researchers have extended empirically based incompressible models to high-speed flows on an ad hoc basis. This is a natural progression because a great deal of incompressible boundary layer research has been conducted. The use of these incompressible models for compressible flow fields has had limited success [3].

Turbulence modeling has progressed as greater knowledge and understanding of turbulent flow structures has increased. Turbulence models are developed by making both observations and assumptions about the flow, and then generating a model. The numerical results are then compared to experimental results to determine the validity of the model. If the model predicts the actual flow characteristics quite well, then it is extended to more complex flow situations to determine its robustness. If the model fails, then it is discarded, and further observations and assumptions are required.

Thus, accurate experimental data are required in order to generate accurate turbulence models. There has been extensive research into the nature of turbulent boundary layers, both in the subsonic and supersonic regimes. Most of these investigations have studied the turbulent boundary layer flowing over a flat plate. A great deal of knowledge has been gained, but unfortunately, aerodynamic flows encounter more than just flat plates. Of particular interest, is the study of turbulent boundary layers with pressure gradient effects. The effects of pressure gradients tend to cause large changes in the turbulent flow structure. These types of flow are prevalent in both internal and external flows.

## *1.2 Objectives*

The primary objective of this research was to investigate experimentally the importance of adverse pressure gradients (APG) on supersonic turbulent boundary layers. A great deal of studies published in the literature have investigated the effects of adverse pressure gradients on turbulent boundary layers (see Refs. [4, 9, 13, 22, 24, 29, 33]). These studies were made with conventional probe and hot-wire anemometry techniques. The present study used Laser Doppler Velocimetry (LDV) to measure the mean and fluctuating velocities. Several other researchers have used LDV to make supersonic turbulent boundary layer measurements over a flat plate (see Refs. [12, 18-19, 25]). After an extensive literature search, it was determined that this is the first investigation to use modern LDV technique as a means to investigate a supersonic turbulent boundary layer subject to an adverse pressure gradient. This clear lack of data was also mentioned by Spina [28].

A second objective of the present study was to provide accurate empirical data to validate the turbulence models created by computational fluid dynamicists. Accurate data are required to complete this task. This was in fact accomplished, as Fick [14] has validated a  $k-\omega$  turbulence model [35] against the present LDV results.

A third objective is to compare the present LDV results with the conventional and hot-wire anemometry results generated by Dotter [9] in the same AFIT Mach 3.0 wind tunnel with the same compression ramp model. In this manner, the validity of the assumptions used to decompose the fluctuating turbulent terms of that data may be accessed.

## *1.3 Settles and Dodson Criteria*

This experiment was conducted with the intent of satisfying the criteria established by Settles and Dodson [26] to provide a valid database of experimental results for turbulence modeling and CFD code validation. This criteria is summarized below:

1. *Baseline Applicability*: All candidate studies must be experiments involving turbulent flows in either the supersonic or hypersonic Mach number range (i.e.  $M \approx 3.0$  or higher).
2. *Simplicity*: All candidate studies passing this criterion must involve experimental geometries sufficiently simple that they may be modeled by CFD methods without enormous difficulty.
3. *Specific Applicability*: All candidate studies passing this criterion must be capable of providing some useful test of turbulence modeling.
4. *Well-defined experimental boundary conditions*: All incoming conditions (especially the state of the incoming boundary layer) must be carefully documented. For studies claiming “two dimensional” flow, data indicating the extent of the spanwise flow variations should be provided.
5. *Well-defined experimental error bounds*: The experimentor must provide an analysis of the accuracy and repeatability of the data, or error bars on the data themselves. Further, error bounds on the data must be substantiated in a quantifiable manner.
6. *Adequate documentation of data*: Data must be documented and tabulated in a machine-readable form.
7. *Adequate spatial resolution of data*: Experiments must present the data of sufficiently high resolution, compared with the scale of the flow in question, that the key features of the flow are clearly resolved.

#### 1.4 Synopsis of the Present Investigation

Laser Doppler Velocimetry (LDV) was used to make mean and fluctuating velocity measurements in the AFIT Mach 3.0 wind tunnel. The measurements were made over flat plate and compression ramp models at the same distance from the nozzle throat. In this manner, the effects of the pressure gradient on the turbulent boundary layer structure could be distinguished from the flat plate effects at the same location. Figure 1-1 presents a schlieren photograph of the present adverse pressure gradient flow field. This figure is included to describe the present flowfield, and the detailed results of Figure 1-1 will be discussed in Chapter 7. Clearly, the shock wave has coalesced outside of the boundary layer. The approximate turbulent boundary layer edge has been designated. The weak lip shocks are results of misalignments between the test sections.

The first step in the analysis was an investigation of the terms that require modeling. Chapter 2 presents the governing equations of turbulent flow and a discussion of the utility of

LDV as a flowfield analysis tool. Chapter 3 summarizes the key principles of Laser Doppler Velocimetry. Thirdly, the experiment was designed to meet the objectives described in Section 1.3. Chapters 4 and 5 present the test facilities and equipment, and the experimental procedures developed for use in this study, respectively. Chapter 6 presents the data reduction techniques used to extract the mean and turbulent flow properties. After the research scope was defined, the testing was performed, and the results analyzed. The results and discussion are given in Chapter 7. Finally, conclusions and recommendations are given in Chapter 8.

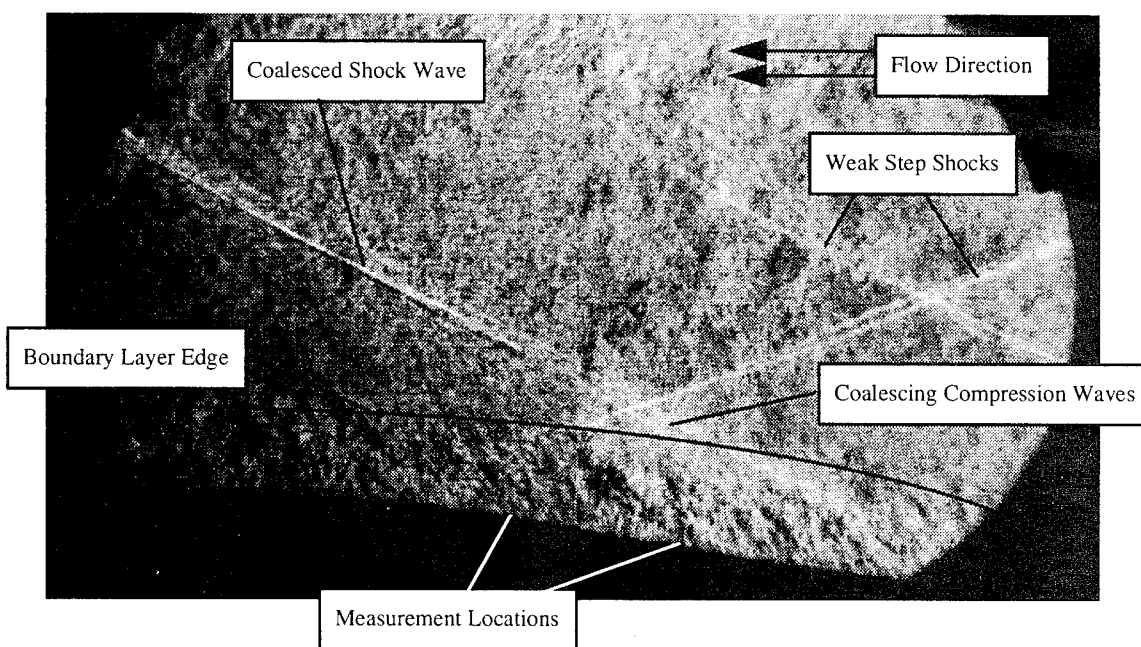


Figure 1-1: Flow Over Compression Ramp Model

## 2. Turbulence Analysis

Turbulent flow, which is governed by the unsteady Navier-Stokes equations, is characterized by temporal and spatial scales which vary over several orders of magnitude. Thus, closed form solutions to practical high Reynolds number problems are not possible with current or near future computer capabilities. Hence, engineers and scientists must rely on approximate time-average methods to obtain solutions for turbulent flow. Due to the nonlinear nature of the Navier-Stokes equations, this procedure results in additional fluctuation cross-correlation terms. The turbulence "closure" problem is the science or art of developing formulations to close the system (i.e., provide enough equations for the unknowns). This chapter presents the formal derivations of both the Reynolds and Favre averaged compressible Navier-Stokes equations.

### 2.1 Governing Equations (Navier-Stokes Equations)

The compressible Navier-Stokes equations govern high speed flow fields where compressibility effects must be considered [34]. Neglecting body forces, the continuity, momentum, and energy equations are given, respectively, by

$$\frac{\partial \rho}{\partial t} + \frac{\partial(\rho u_j)}{\partial x_j} = 0 \quad (2.1)$$

$$\frac{\partial(\rho u_j)}{\partial t} + \frac{\partial(\rho u_i u_j)}{\partial x_j} = -\frac{\partial p}{\partial x_i} + \frac{\partial(\tau_{ij})}{\partial x_j} \quad (2.2)$$

$$\frac{\partial(\rho h_o)}{\partial t} + \frac{\partial(\rho u_j h_o)}{\partial x_j} = \frac{\partial p}{\partial t} + \frac{\partial(u_i \tau_{ij} - q_j)}{\partial x_j} \quad (2.3)$$

where the stagnation enthalpy, shear stress, and heat flux are respectively defined as:

$$h_o = h + \frac{1}{2} u_i u_i \quad (2.4)$$

$$\tau_{ij} = \mu \left( \frac{\partial u_i}{\partial x_j} + \frac{\partial u_j}{\partial x_i} \right) - \frac{2}{3} \mu \delta_{ij} \frac{\partial u_k}{\partial x_k} \quad (2.5)$$

$$q_j = -k \frac{\partial T}{\partial x_j} \quad (2.6)$$

## 2.2 Reynolds-Averaged Navier-Stokes (RANS) Equations

The Reynolds-averaged Navier-Stokes equations [1] are derived when time averaged flow properties, like the velocity, are decomposed as

$$u(x, y, z, t) = \bar{u}(x, y, z) + u'(x, y, z, t) \quad (2.7)$$

where  $\bar{u}$  is the time averaged velocity, and  $u'$  is the instantaneous fluctuating turbulent component. The time averaged quantity  $\bar{u}$  is defined by

$$\bar{u} \equiv \frac{1}{\Delta t} \int_{t_0}^{t_0 + \Delta t} u dt \quad (2.8)$$

where the  $\Delta t$  must be finite and large compared to the period of random turbulent fluctuations, but small compared to the mean flow time scale.

Once the decoupled variables are substituted into the Navier-Stokes equations, and the rules of time averaging applied [1]; the RANS equations for continuity, momentum, and energy are obtained:

$$\frac{\partial \bar{\rho}}{\partial t} + \frac{\partial (\bar{\rho} \bar{u}_j + m_j^R)}{\partial x_j} = 0 \quad (2.9)$$

$$\frac{\partial (\bar{\rho} \bar{u}_i + \bar{\rho}' \bar{u}'_i)}{\partial t} + \frac{\partial (\bar{\rho} \bar{u}_i \bar{u}_j)}{\partial x_j} = -\frac{\partial \bar{p}}{\partial x_i} + \frac{\partial (\bar{\tau}_{ij} + \tau_{ij}^R)}{\partial x_j} \quad (2.10)$$

$$\frac{\partial (\bar{\rho} \bar{e}_o + \bar{\rho}' \bar{h}'_o)}{\partial t} + \frac{\partial (\bar{\rho} \bar{h}_o \bar{u}_j)}{\partial x_j} = \frac{\partial (\bar{u}_i \bar{\tau}_{ij} + \bar{u}'_i \bar{\tau}'_{ij} - q_j - q_j^R)}{\partial x_j} \quad (2.11)$$

where the Reynolds averaged compressible turbulence terms are given as

$$m_i^R = -\bar{\rho}' \bar{u}'_i \quad (2.12)$$

$$\tau_{ij}^R = -\bar{\rho} \bar{u}'_i \bar{u}'_j - \bar{u}_i \bar{\rho}' \bar{u}'_j - \bar{u}_j \bar{\rho}' \bar{u}'_i - \bar{\rho}' \bar{u}'_i \bar{u}'_j \quad (2.13)$$

$$q_i^R = \bar{\rho} \bar{h}'_o \bar{u}'_i + \bar{h}_o \bar{\rho}' \bar{u}'_i + \bar{u}_i \bar{\rho}' \bar{h}'_o + \bar{\rho}' \bar{h}'_o \bar{u}'_i \quad (2.14)$$

and

$$\bar{\tau}_{ij} \approx \mu \left[ \left( \frac{\partial \bar{u}_i}{\partial x_j} + \frac{\partial \bar{u}_j}{\partial x_i} \right) - \frac{2}{3} \delta_{ij} \frac{\partial \bar{u}_k}{\partial x_k} \right] \quad (2.15)$$

The averaging process eliminates several key turbulent characteristics, e.g. frequency, phase, and wavelength of turbulent motion [3]. For incompressible flows, the apparent mass flux ( $m_i^R$ ) and the last three terms of the turbulent shear stress ( $\tau_{ij}^R$ ) and turbulent heat flux ( $q_i^R$ ) are zero.

### 2.3 Favre-Averaged Navier-Stokes (FANS) Equations

The Favre-averaged Navier-Stokes equations [3] are based on mass-weighted time averages. The mass-weighted time average velocity is decomposed as

$$u(x, y, z, t) = \tilde{u}(x, y, z) + u''(x, y, z, t) \quad (2.16)$$

where the Favre mean value is defined as:

$$\tilde{u} \equiv \frac{\overline{\rho u}}{\overline{\rho}} \quad (2.17)$$

and  $u''$  is the instantaneous fluctuating turbulent component. Note, unlike  $\overline{u}'$ ,  $\overline{u}'' \neq 0$ . The Favre-averaged continuity, momentum, and energy equations are:

$$\frac{\partial \overline{\rho}}{\partial t} + \frac{\partial (\overline{\rho} \tilde{u}_j)}{\partial x_j} = 0 \quad (2.18)$$

$$\frac{\partial (\overline{\rho} \tilde{u}_i)}{\partial t} + \frac{\partial (\overline{\rho} \tilde{u}_i \tilde{u}_j)}{\partial x_j} = -\frac{\partial \tilde{p}}{\partial x_i} + \frac{\partial (\overline{\tau}_{ij} + \tau_{ij}^F)}{\partial x_j} \quad (2.19)$$

$$\frac{\partial (\overline{\rho} \tilde{e}_o)}{\partial t} + \frac{\partial (\overline{\rho} \tilde{h}_o \tilde{u}_j)}{\partial x_j} = \frac{\partial (\tilde{u}_i \overline{\tau}_{ij} + \overline{u'_i \tau'_{ij}} - \overline{q}_j - q_{ij}^F)}{\partial x_j} \quad (2.20)$$

where the fluctuating Favre averaged turbulent terms are

$$\tau_{ij}^F = -\overline{\rho u'_i u''_j} \quad (2.21)$$

$$q_i^F = \overline{\rho h'_o u''_i} \quad (2.22)$$

and, neglecting viscosity fluctuations,

$$\bar{\tau}_{ij} \approx \mu \left[ \left( \frac{\partial \tilde{u}_i}{\partial x_j} + \frac{\partial \tilde{u}_j}{\partial x_i} \right) - \frac{2}{3} \delta_{ij} \frac{\partial \tilde{u}_k}{\partial x_k} \right] \quad (2.23)$$

#### 2.4 RANS & FANS Relationship

Because of the nature of the Favre-averaged method, there is no explicit appearance of the density-velocity correlations as with the Reynolds-averaged equations. Thus, the compressible FANS equations closely resemble the incompressible Reynolds-averaged form. For this reason, Favre averaging is almost universally adopted in the aerospace community [3].

By decomposing a flow parameter, say the streamwise velocity component,  $u$ , by both methods, and equating, the relation between Reynolds and Favre-averaged variables is determined:

$$\bar{u} - \tilde{u} = -\frac{\overline{\rho' u'}}{\overline{\rho}} = \bar{u}'' \quad (2.24)$$

Also,

$$u'' = u' + \overline{u''} \quad (2.25)$$

In addition, through the above identities, the Favre and Reynolds shear stresses are related by:

$$\overline{\rho u'_i u''_j} = \overline{\rho u'_i u'_j} + \overline{\rho u''_i u''_j} \quad (2.26)$$

Since the second term on the right hand side of Eq. (2.26) is fourth order, it is small compared to the second order shear stresses. Thus,

$$\tau_{ij}^R \approx \tau_{ij}^F \quad (2.27)$$

Therefore, LDV can provide accurate estimates of the Favre averaged shear stress.

### *3. Principles of Laser Doppler Velocimetry*

This chapter presents a brief overview of the basic principles behind Laser Doppler Velocimetry. This information provides a sound foundation upon which the proper system settings, given in Chapter 5, were based.

#### *3.1 Overview*

The Laser Doppler Velocimetry (LDV) system has been developed into a research tool of unique capabilities. This technique can measure particle velocities in a small flow volume that are very close to a solid surface, without disturbing the flow field. As the name implies, LDV makes use of lasers and a Doppler frequency shift to calculate the velocity of a gaseous flow. Seed particles, such as smoke, latex spheres, or olive oil, are introduced into the flow field. As these particles pass through the probe volume, the laser light is scattered. Photomultiplier optics are used to measure the Doppler shift, which is the difference between the frequency of the scattered and transmitted light. Based on the wavelength and optical setup of the laser, the particle's velocity can be measured [10, 17].

A 3D component LDV system enables velocity measurements in three orthogonal directions. The present study used the system in a configuration to measure velocity components in two of these directions. Measurements in each direction are facilitated by a single channel, fringe mode setup. The combined efforts of two of these components allowed measurements of the u- and v-velocities along the x- and y-directions, respectively (see Figure 3-1).

### 3.2 Probe Volume & Interference Pattern

The transmitting optics split each wavelength of laser light into two beams. These beams are passed through a lens which causes them to intersect. The intersection of the beams creates the probe volume or measurement volume, which is ellipsoidal in shape. This shape is a result of the Gaussian intensity profiles of the laser beams [8]. The size of the probe volume is determined by the wavelength and diameter of the laser beam, and separation distance of the emitted beams. Figure 3-1 shows the probe volume.

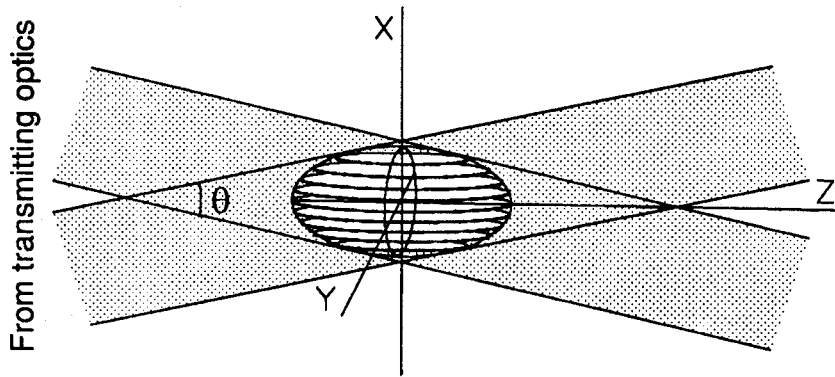


Figure 3-1: Fringe Disks of Probe Volume [8]

The intersection of the two coherent laser beams creates an interference pattern, known as interference fringes. Due to the 3D nature of the laser beam, the interference fringes actually appear as fringe disks. Because the beams intersect at the beam waists, or narrowest width of the beam, the wave fronts are nearly parallel; thus, the interference fringes will be parallel. Parallel fringes are important characteristics because of the resulting uniform velocity-frequency correlation over the entire probe volume [8]. The fringe spacing,  $d_f$ , is given by

$$d_f = \frac{\lambda/2}{\sin(\theta/2)} \quad (3.1)$$

where  $\lambda$  is the laser wavelength, and  $\theta$  is the angle between the two incident beams. With the fringe spacing determined, the velocity of the particle can be determined by measuring the time that elapses as the particle passes through the probe volume. Figure 3-2 shows the geometry of the intersecting laser beams.

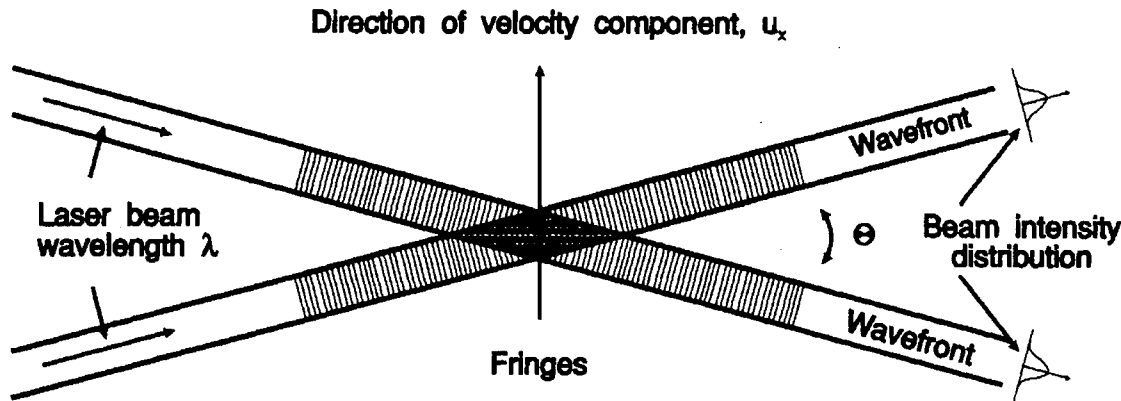


Figure 3-2: Laser Beam Intersection Pattern [7]

### 3.3 Calculation of Velocity

The laser optics include both transmitting and receiving optics. A photomultiplier, or PM tube, is used to help the photodetector sensor convert the scattered light into a continuous signal. The frequency of the signal depends on the motion of the particle; higher frequencies are associated with faster moving particles. As the particle traverses the probe volume and crosses the fringe patterns, a series of “on” and “off” signals are created. From this signal, the time to traverse the probe volume can be measured. Since both the fringe spacing and traverse time are known, the particle velocity can be determined.

The direction that the velocity is to be measured is assumed perpendicular to the bisector of the beam intersection angle  $\theta$  and lies in the plane formed by the transmitted laser beams. The velocity of a particle passing through the probe volume is given by

$$u_x = f_D \frac{\lambda/2}{\sin(\theta/2)} \quad (3.2)$$

where  $f_D$  is the Doppler frequency. The Doppler frequency is determined by analyzing the signal, or Doppler burst, created as a particle passes through the probe volume. Figure 3-3 shows a typical Doppler burst. The maximum points indicate when the particle has passed through a fringe, while the minimum points indicate when the particle is between fringes. The time interval between each peak, or period  $T_D$ , is the time required for a particle to cross a fringe disk in the probe volume. The corresponding Doppler frequency is given by  $f_D = 1/T_D$ .

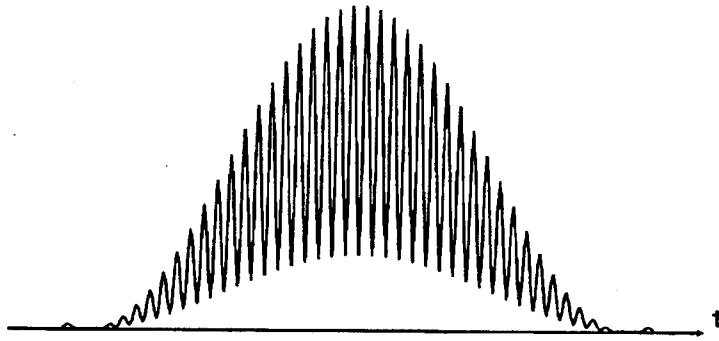


Figure 3-3: Doppler Burst [7]

The frequency of the Doppler shift signal is determined by the Burst Spectrum Analyzer (BSA). The BSA breaks the signal into the envelope and pedestal, and creates a Fast-Fourier Transform (FFT) to match the Doppler signal. This begins when the signal exceeds a threshold voltage, and continues until the signal drops below the threshold voltage. The length of time that the threshold has been exceeded,  $T_m$ , is recorded. The Doppler burst is modeled by using the record length, or  $N$  samples taken  $T_s$  seconds apart. The resulting Doppler frequency is given by

$$f_D = \frac{N}{T_m} \quad (3.3)$$

If the envelope of the Doppler signal exceeds a higher threshold, the input sampling is restarted. The samples stored in the input buffer are deleted, and the sampling process is repeated. This may be repeated several times; each time with a higher threshold voltage. This procedure ensures that the Doppler frequency is determined by the part of the burst with the largest amplitude. With the Doppler frequency determined, the particle's velocity is easily determined by Eq. (3.2).

The bandwidth,  $BW$ , is defined as the range of frequencies (or velocities, depending on the desired units) over which possible frequencies are to be determined. The size of the bandwidth limits the sample time,  $T_s$ , and its associated frequency,  $f_s = 1/T_s$ . The frequency is proportional to the bandwidth, and given by  $f_s = n(BW)$  where  $n$  is greater than one, and predetermined by the BSA configuration. Therefore, the total sampling time is increased as the record length is increased. The sampling time must be less than the time to traverse the control volume [7].

Each of two components of velocity are measured with two separate BSA's and laser beams of different wavelength. The wavelength of each laser beam is programmed into the BSA so that it is dedicated to measuring velocities in the plane of the corresponding laser beams. Thus, a BSA is required for each component of velocity to be measured. A calibration factor,  $C_{fv}$ , gives the relationship between the signal frequency and velocity. The calibration factor is a function of the wavelength and optical configuration, and is given as

$$C_{fv} = \frac{\lambda/2}{\sin(\theta/2)} \quad (3.4)$$

where the units of the calibration factor are  $m/s/MHz$ . The calibration factor also gives the fringe spacing,  $d_f$ , in units of  $\mu m$ .

### *3.4 Overcoming Directional Ambiguity*

The problem of directional ambiguity exists because the frequency of the Doppler signal is independent of the sign of the direction of velocity. The same Doppler signal would be generated for positive and negative velocities of the same magnitude. A phase shift is introduced by passing one of the beams of each wavelength through the Bragg cell. The Bragg cell is a glass cell that includes an oscillating electromechanical transducer. As the each pair of beams passes through the Bragg cell, a frequency phase shift is introduced. The shift in frequency,  $f_B$ , causes the fringes to sweep across the probe volume at a constant velocity in the direction of the desired velocity component. Johnson [16] gives this constant velocity as

$$v_f = d_f f_B \quad (3.5)$$

where  $d_f$  is the fringe spacing. The direction that the particle travels, and thus its corresponding velocity, can be determined from the sweeping fringe motion.

### *3.5 Validation of Particles*

*3.5.1* Unfortunately, not all particles that traverse the probe volume give accurate velocity measurements. Some particles pass through the middle of the volume, while others just barely clip the edge. There are several methods employed by the BSA to filter “bad” particles crossing the probe volume. Those particles that pass the filtering criteria are considered valid particles.

### 3.5.1 Fringe Count

A minimum number of fringes must be crossed by each particle before it can be validated. When measuring highly turbulent flows, particles may enter the probe volume from any direction. Those particles entering the control volume nearly parallel to the fringes will cross fewer fringes than particles entering perpendicular to the fringes. Because the desired measurement direction of velocity is perpendicular to the fringes, particles crossing a few fringes nearly parallel are not accurately representing the correct velocity component. Also, particles passing perpendicular to the fringes, but near the edge of the probe volume, will not pass through enough fringes.

### 3.5.2 Particle Acceleration

Particles that change velocity while passing through the probe volume are not validated. The particle's acceleration may be detected by comparing the time to cross different number of fringes. If the time between crossing each of 10 fringes is different than that of 20 fringes, then the particle's velocity is not constant. Therefore, the accelerating or decelerating particle is not valid, and its contribution is rejected.

### 3.5.3 Spectrum Validation

While computing the Doppler frequency, the BSA compares the intensity of the gathered light at each sample. For example, Figure 3-4 shows the intensity at 32 different sample locations. The two largest local maximum intensities are compared to the overall maximum intensity. Particles are validated if the local maximum is four times less than the global maximum of the spectrum [7].

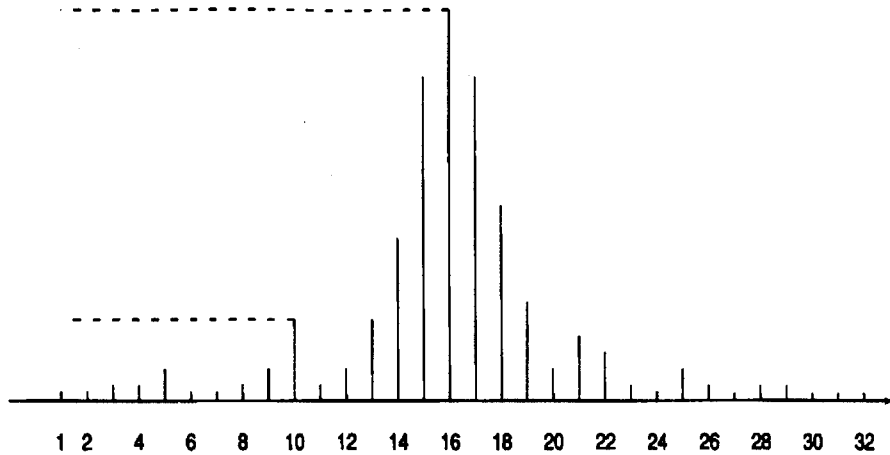


Figure 3-4: Spectrum Validation [7]

### 3.5.4 Doppler Signal Validation

Another form of validation involves analyzing and comparing the pedestal and envelope of the Doppler burst. The pedestal and envelope of the signal are generated through signal processing, as shown in Figure 3-5. These characteristics of the Doppler signal are compared for particle validation. The quality factor, which is a user defined parameter, is the ratio between the envelope and pedestal peak voltages. Particles must have signal amplitudes that exceed the quality factor to be validated.

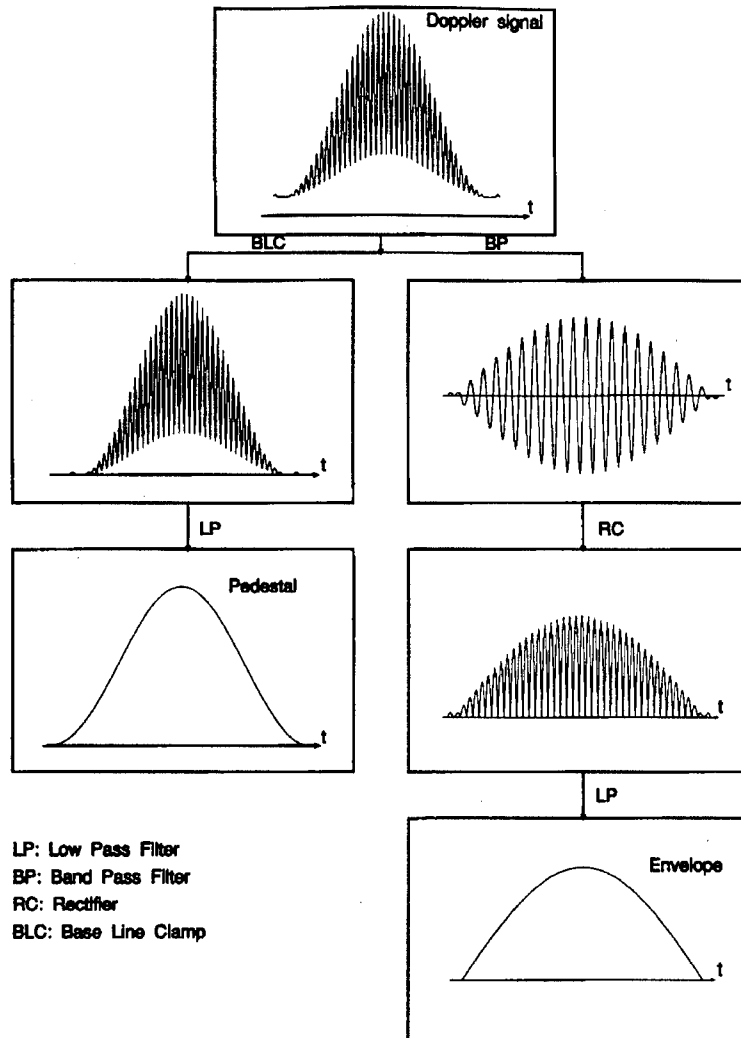


Figure 3-5: Envelope and Pedestal Generation [7]

### 3.6 Coincidence Window

With a two-component LDV system, a particle traversing the probe volume will produce two different Doppler signals; one corresponding to each wavelength of light. Because the two signals are independent of one another, there must be a method of correlating the two bursts. Coincidence processing is the procedure of comparing the arrival time of a particle. It is very important that the BSA's are tracking the same particle through the probe volume space. Otherwise, the two signals would not be correlated, the velocity correlations and turbulent shear

stresses would be artificially low. During data acquisition, the velocity, arrival time, and transit time for each burst are recorded by each BSA. As a particle enters the probe volume, the first BSA signals the second BSA to "look" for the same particle. The coincidence window is the maximum allowable difference in arrival times for the two BSA signals. Coincident bursts are those bursts that meet this criteria. If the coincidence window is exceeded, then the BSA's are not tracking the same particle and the burst is rejected. The size of the coincidence window must be carefully selected so that two burst created by a single particle are correlated, yet must not allow more than one burst from one BSA correlate with a burst from another BSA. Also, the coincidence window must be a fraction of the time that a particle takes to traverse the probe volume.

### *3.7 Forward- vs. Back-Scattering Method*

Doppler bursts are created by collecting and analyzing the light that scatters forward, or ahead, of the particle. It is very important to position the receiving optics in a configuration so that the maximum intensity of the scattered light may be collected. The relative magnitude of the scattered light depends on the size of the seed particle, as seen in Figure 3-6. When the particle diameter,  $d_p$ , is larger than the wavelength of the laser light, a larger intensity of the light is scattered ahead of the particle. Figure 3-7, which is on a radial log scale, indicates that the magnitude of the forward scattered light is several orders of magnitude larger than backward scattered light.

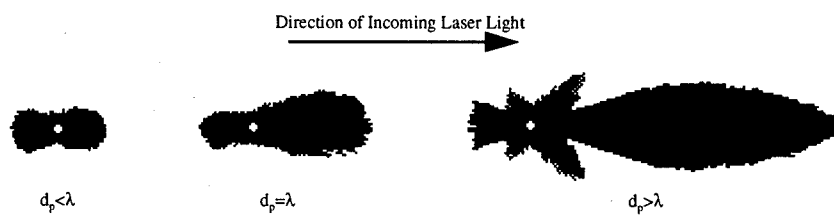


Figure 3-6: Scattered Light Intensity [6]

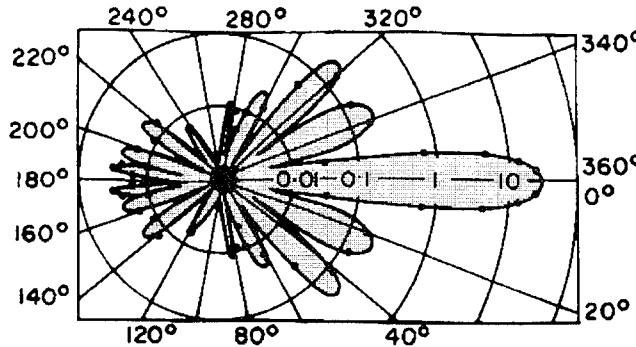


Figure 3-7: Magnitude of Light Intensity [10]

The LDV system may be configured in either back- or forward-scattering collection mode. In order to take advantage of the forward scattered light, the receiving and transmitting optics are configured in forward-scattering mode. In this arrangement, the receiving and transmitting optics are on opposite sides of the desired measurement region, in this case the wind tunnel. Forward-scattering mode enables collection of the larger intensities of light, resulting in stronger Doppler signals.

In some cases, the back-scattering method may be used. In this arrangement, the transmitting optics also act as the receiving optics; thus, only one probe is required. For the present system, the back-scattering mode is a “point-and-shoot” method because the optics are pre-aligned within the probe. Accurate compressible measurements are typically difficult to obtain due to the low power of the scattered light. For this reason, the back-scattering mode was not used in this experiment.

### 3.8 Seeding Considerations

The quality of the LDV measurements depends greatly on the method of seeding the flow. While at times it may be possible to make accurate LDV measurements from particles that occur naturally in the flow field, it is desirable to filter out naturally occurring particles, and then seed the flow with particles of known size and material properties [11]. Particles must be small

enough that they accurately follow the fluid flow field, yet large enough to scatter enough laser light to produce a measurable Doppler signal.

Seeding of particles can occur at different locations in the flow field. In Ref. [11], Elena makes several suggestions for seeding supersonic flows. The flow field upstream of the measurement location must remain undisturbed by introduction of the particles. Injecting the particles at the local mean flow velocity achieves this requirement. Elena also showed that the wake created by injecting seed particles at the wall greatly affects the accuracy of boundary layer measurements.

Particle sizing and material composition are other important factors that affect the accuracy of LDV measurements. Particles must be small enough to follow even the smallest fluid motions. Particles which are too large will lag behind the actual flow velocity, thus experiencing velocity slip. They must be made of material that does not adhere to the wind tunnel or windows. When shock waves are studied, the particles must have fast response times in order to map the rapid changes in flow conditions. High density particles may even change the flow conditions of the flow field being analyzed.

### *3.9 Optical Alignment*

When making LDV measurements, it is possible to align the laser beams in different ways relative to the desired velocity directions, as shown in Figure 3-8. The coordinate system shows the direction of the actual flow velocities, while the black and white circles symbolize the different laser beams. The lighter arrows indicate the direction of positive velocity. With the first method, one pair of laser beams measures the u-component of velocity, while the v-component is measured with the other beams. With the second method, the beams are rotated by an angle, in this case  $45^\circ$  clockwise, so that each laser is measuring a contribution of each

component of velocity. An optical transformation must be used during post-processing to resolve the components of velocity in the actual coordinate system.

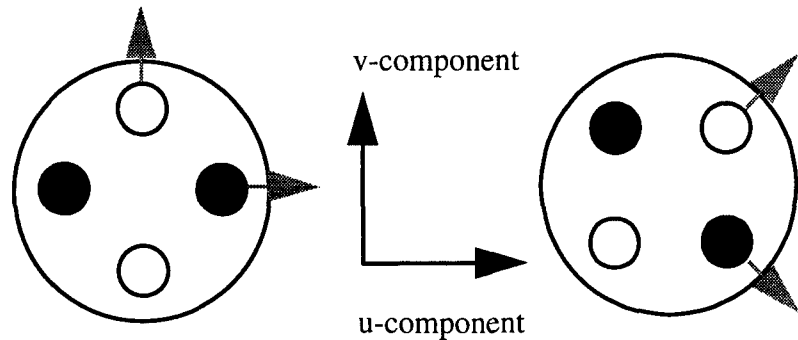


Figure 3-8: Possible Optical Alignments

As described by Elena [11], the problem of angular bias is introduced when the optics are aligned as on the right side of Figure 3-8. When the probe volume is rotated, the number of fringes crossed by a particle could be reduced as the particles may enter the volume almost parallel to the fringes. As mentioned previously, these particles are not validated. Rejecting these signals, results in errors in the calculation of turbulence intensities and the correlation  $\overline{u'v'}$ . Elena and LaCharme [12] reported that the measured values of turbulence intensities and magnitude of  $\overline{u'v'}$  are decreased when the optics are rotated from the original coordinate system.

#### *4. Test Facilities and Equipment*

This chapter discusses the equipment and facilities used in this investigation. The entire experimental investigation was conducted in the AFIT Mach 3.0 ( $Re/m = 1.75 \times 10^7$ ) supersonic wind tunnel. This chapter describes the wind tunnel configuration and Laser Doppler Velocimetry system used in this experiment, including the temperature and pressure measuring apparatus, and flow visualization equipment.

##### *4.1 Wind Tunnel Facilities*

The AFIT supersonic wind tunnel was a blow-down, pressure-vacuum system. High-pressure air was introduced into the settling, or plenum chamber. The end of the tunnel was connected to pressure-vacuum tanks. The combination of high-pressure air and a vacuum provided the necessary conditions to run the tunnel. The layout of the AFIT Mach 3.0 wind tunnel is presented in Figure 4-1.

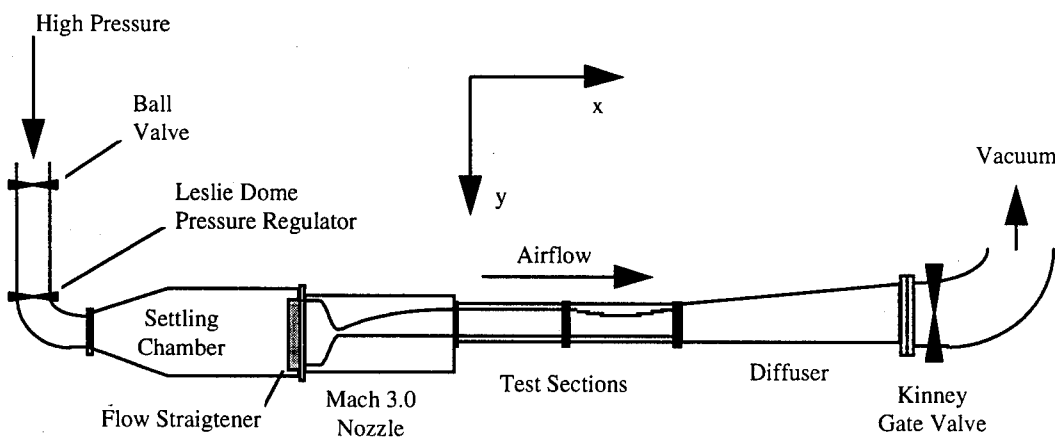


Figure 4-1: AFIT Mach 3.0 Tunnel Schematic

#### 4.1.1 Plenum Chamber

The settling chamber pressure and temperature were maintained at  $2.06 \pm 0.02$  atm, and  $295 \pm 2$  K for all test runs. Plenum chamber pressure and temperature were measured between the flow straightener and the nozzle. The Pitot pressure was measured with an Endevco 0.69 MPa pressure transducer, and the temperature was measured with an Omega Engineering Type K thermocouple.

#### 4.1.2 Air Supply

Two Atlas Copco GAU 807 air compressors provided air at 0.69 MPa. The air was dried by two Pioneer Air Systems, Inc. Model R500A Refrigerant Air Dryers before entering the high-pressure reservoir. The mass flow rate was 0.5 kg/s. A centrifugal moisture and particle separator, with multi-layered high grade filters, was used to cleanse the air before it entered the tunnel.

Two 7.5 hp, 460 V Stokes-Penwalt Model 212-11 MicroVac evacuation pumps were used to evacuate the 16 cubic meter vacuum tank system. The vacuum was maintained by a Stokes-Penwalt seal exhaust pump. Each pump was powered by a Reliance XW Duty Master AC motor. The vacuum-pressure system empties the vacuum tanks to 2 mmHg, or 267 Pa, in approximately 7 minutes. Wind tunnel test runs were performed when the pressure in the vacuum tanks was below 15 mmHg, or 2000 Pa. This configuration provided approximately 25 seconds of constant wind tunnel operation before unstarting conditions occurred.

#### 4.1.3 Supersonic Nozzle

The converging-diverging half-nozzle generated a mean flow Mach number of 3.0. The freestream Reynolds number per meter, based on plenum total temperature and pressure, was calculated as  $Re/m = 1.75 \times 10^7$ . The nozzle exit cross section was 6.35 x 6.35 cm, and the

distance from the throat to the end of the nozzle was 27 cm. Figure 4-2 shows the Mach 3.0 nozzle.

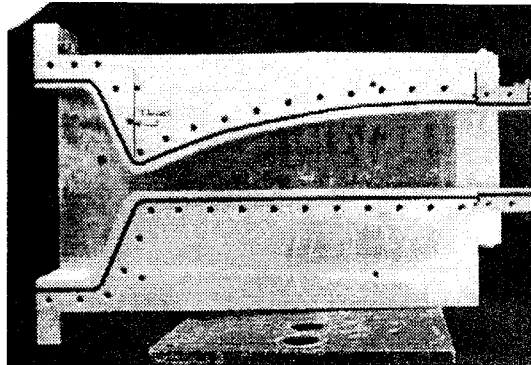


Figure 4-2: Mach 3.0 Nozzle

#### 4.1.4 Test Section

Two test sections measuring 6.35 cm by 6.35 cm in cross-section, and 33.0 cm in length were located directly downstream of the nozzle. The test sections of the tunnel were designed to facilitate simple interchange of models for other users. The walls of the test section, nozzle, and diffuser were made of 1.905 cm thick aluminum alloy. Except for the flat plate measurements at the  $x = 44$  cm location, all other measurements in the present study were made in the second test section. The first test section was fitted with flat plate walls on all sides.

A compression ramp model was fabricated to produce an adverse pressure gradient (APG). After evaluation of the results, it was determined that the model generated regions of both adverse and favorable pressure gradient (FPG). The FPG was generated by the flow expanding around the top of the model. The model was carefully designed to avoid separated flows in the regions where measurements were to be taken. It was also designed so that compression waves would coalesce into a shock outside of the boundary layer. The curved wall generated a mild compression, where the Clauser pressure gradient parameter,  $\beta$ , was roughly

1.12 at 68 cm in the adverse pressure gradient region, and approximately -0.94 in the favorable pressure gradient region at 71 cm. The compression ramp model matched the curve fit given by

$$Y(x) = 1.1858 - 0.541x + 0.0748x^2 - 0.0028x^3 \quad (4.1)$$

where  $Y(x)$  is the change in model height from flat plate entrance conditions, and the x-coordinate is measured from the front of the test section. The units of Eq. (4.1) are centimeters. The standard deviation of the curve fit was 0.0008 cm. The model is symmetric about the mid-length. Figure 4-3 shows the APG model along with the possible window configurations of the test section. The two lines represent the profiles along which the LDV measurements were made. The two asterisks on the profiles indicate the location of the origin for each LDV measurement profile. The model was mounted as the ceiling of the second test section.

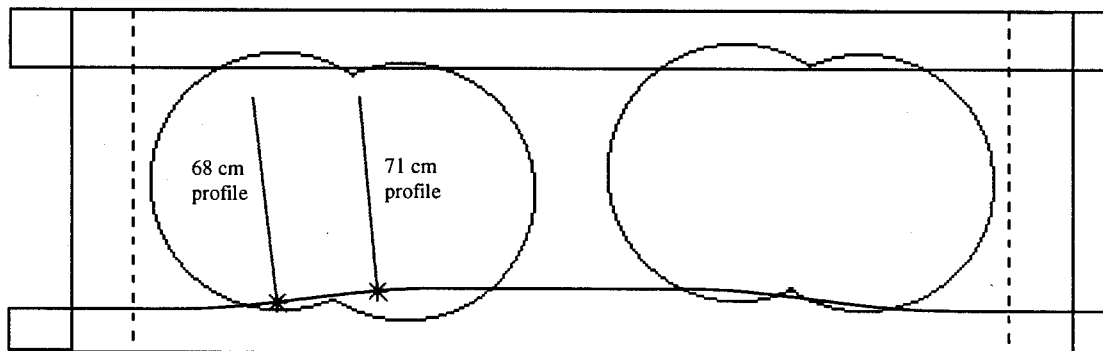


Figure 4-3: Compression Ramp Model with Test Section

The compression ramp model also included pressure taps along its centerline. The surface pressure was measured with an Endevco 0.103 MPa pressure transducer. The first port was located 3 cm behind the front of the model, with seven more ports successively spaced 2.5 cm apart. A surface pressure plot is included in Chapter 7.

Because a forward-scattering configuration was required, each side wall of the test section was modified by adding two 7.62 cm diameter windows. The circular optical quality

glass windows were 1.27 cm thick. They were secured in the walls with pressure gaskets and interchangeable mounting clamps. The moveable clamps allowed adjustment while viewing different sections of the flow field. The windows were offset from the lateral and longitudinal centerline of the wall. Most of the test section was unobstructed because the walls could be mounted on either side of the tunnel test section. Figure 4-4 shows the possible glass window configurations which provided excellent observation for LDV measurements and flow visualization photographs.

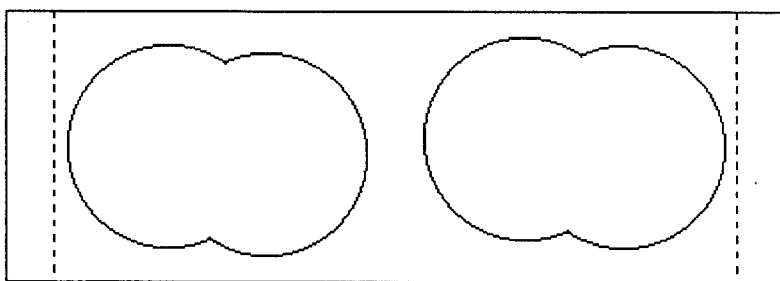


Figure 4-4: Possible Window Configurations

#### 4.2 *Laser Doppler Velocimetry System*

The Dantec FiberFlow three-component Laser Doppler Velocimetry system used in this experiment consisted of the laser and necessary optics to manipulate the beams, and a three-axis traverse that allowed precision positioning of the probe volume. The data processing system included three Burst Spectrum Analyzers (BSA), and software to facilitate data processing and communication with a PC computer. A flow seeder, including injector, was added to the tunnel to introduce seed particles for the LDV measurements.

##### 4.2.1 *FiberFlow System*

The Dantec Measurement Technology 60X FiberFlow system was used to make LDA measurements. The purpose of the FiberFlow system was to generate and manipulate the laser

beams necessary for LDV measurements, and then detect and record the resulting Doppler burst signals. The FiberFlow system consisted of a laser light source, transmitter, photo multiplier tubes, and optical probes with lenses.

The Ion Laser Technology, Model 5500A-00 Ar-ion laser provided a coherent light source. The 300 mW laser, capable of generating laser radiation in the 457 nm to 514.5 nm range was optimized to 275 mW. The laser power supply, Ion Laser Technology Model 5405A operating at 210 Volts and 20 Amps required a 220 VAC power source. The laser was designed to operate in the TEM<sub>00</sub> transverse mode, where the laser power is centered around the optical axis with maximum power in the center. The  $1/e^2$  beam diameter of the laser was 0.82 mm [16].

The FiberFlow 60X41 transmitter, which was equipped with six 60X24 manipulators, served the role of splitting the laser light source into three separate wavelengths, and then delivering these laser beams to the 55X optical probes [6]. The laser was separated into wavelengths of 514.4 nm, 488 nm, and 476.5 nm, which corresponded to the green, blue, and violet beams, respectively. Upon entering the transmitter, the laser light passed through the Bragg cell which introduced a +40 MHz frequency shift,  $f_B$ , to one beam of each wavelength.

After passing through the Bragg cell, the beams passed through the six 60X24 manipulator. The manipulators positioned the laser beam on the exact center of the fiber optic cable by causing the beams to converge. Each manipulator has four adjustments which controlled the beam angle and displacement position of the laser beam relative to the optical axis of the fiber optic cable. The path of the laser beams ran from the manipulators through the fiber optic cables to the optical probes [8]. Figure 4-5 shows the FiberFlow system.

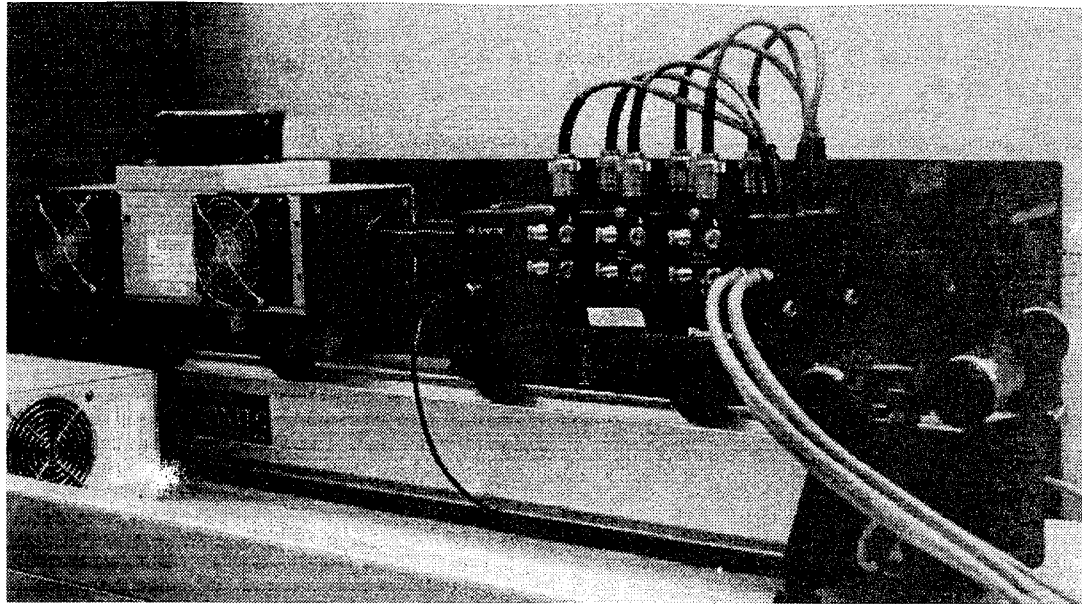


Figure 4-5: Laser Source and FiberFlow System

Each of the 60X optical probes included a fiber optic transducer, distributor unit, and transmitting and receiving fibers [8]. The distributor unit served as an interface between the transducer head, which was connected to the fiber cable, and the transmitting and receiving fibers. Two transmitting fibers are included for each laser beam component; the 2D probe had four transmitting fibers. Two pair of beams, the blue and green beams, ran through the 60X61 2D probe, while the remaining violet beam ran through the 1D 60X60 probe. A 55X12 beam expander, which was used to reduce the measurement volume, was mounted on the 1D probe. The receiving fibers returned the acquired signal to the photo multipliers. The focal length of the 60 mm diameter lens on each probe was 600 mm. Each probe was secured to a micrometer adjustable mount. The 2D probe mount was only able to swivel in the horizontal plane. The 1D probe, which was used as the receiving optics in the forward-scattering configuration, was mounted on a stand that included horizontal swivel and vertical adjustments.

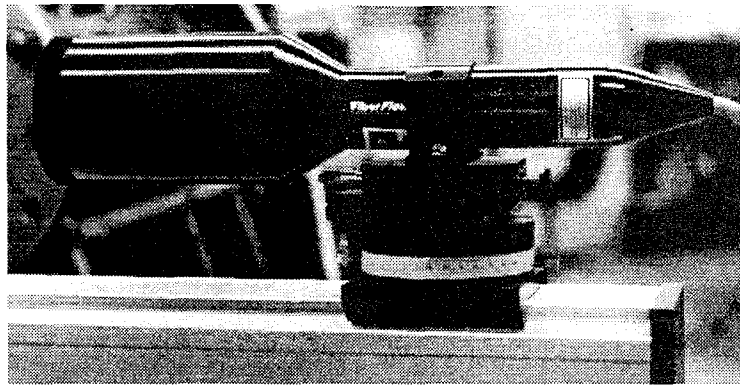


Figure 4-6: 1D Probe with Adjustable Base

To make LDV measurements, the lasers beams must intersect at the same location.

While the 476.5 nm wavelength beam did not actually measure a velocity component, alignment with the probe volume of the 2D lasers ensured proper reception of the scattered light. Poor signal quality resulted when the probe volumes of the transmitting and receiving optics were not properly aligned. The probe mounts were positioned on the ends of a 1.83 m mounting bench on the traverse. The angle of offset for each probe was 3.5° from the mounting bench axis. Based on this offset angle and the 600 mm focal lengths of each lens, the lenses of the receiving and transmitting probes were separated by a distance of 1.2 meters.

Scattered light signals entered the receiving fibers which were connected to the photo multiplier tubes via the fiber optic cables. When high-voltage was applied to the PM tubes, the scattered light signal was converted into a Doppler frequency signal. The 55X35 dual-component tube was used for measurement of the u- and v-components of velocity. While this Dantec LDV system could also be configured for three-component LDV measurements, only the dual-component PM tube was used in this experiment.

#### 4.2.2 Dantec 3D Traverse System

The probe volume for LDA measurements was positioned with the aid of the Dantec 3D traverse. Traverse movement for each axis was controlled by a Whedco DC servo motor and encoder. The encoder converted 1000 pulses into 1 revolution of the traverse axis load screw. Each revolution of the load screw moved the traverse 2 mm. Traverse positioning was accurate to 80 $\mu$ m over a 600 mm range. The three-axis traverse allowed maximum travel of 600 mm in each of three axis directions [5]. Each axis was fitted with limit switches to prevent displacements that would exceed the physical limitations of the traverse. Figure 4-7 shows the traverse configuration with mounting bench and optical probes.

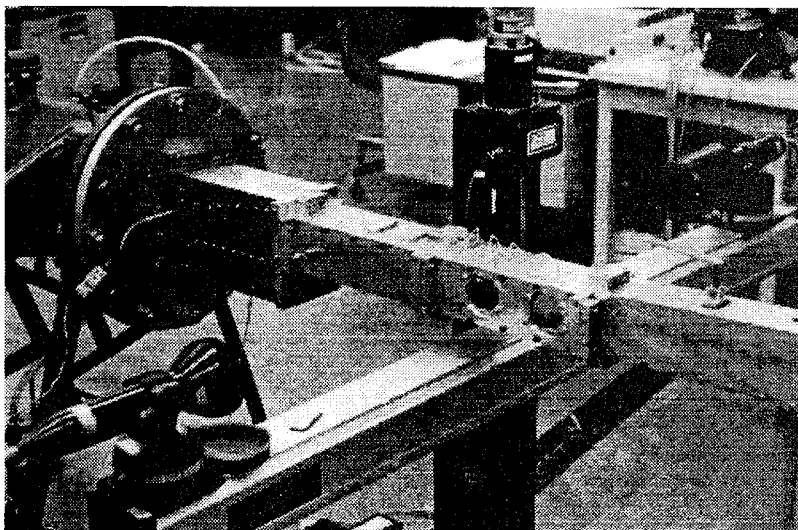


Figure 4-7: 3D Traverse with Probes

The y-axis of the traverse was aligned with the wind tunnel, with the z-axis running perpendicular to the horizon. The traverse's x-axis completed a standard right-hand-rule coordinate system. The traverse was controlled via the BURSTware software. The mounting bench, discussed in the previous section, was aligned with the x-axis of the traverse, or perpendicular to the wind tunnel.

#### 4.2.3 Burst Spectrum Analyzers

The purpose of the BSA's was to perform Fast Fourier transforms (FFT) on the LDA signal. Three BSA's were included in the Dantec 3D Laser Doppler Velocimetry system. Because only two components of velocity were measured, only two of the three BSA's were used. One of the BSA's was a Dantec 57N20 BSA Enhanced model which included keyboard and LED displays on its front panel. The remaining two analyzers were Dantec 57N35 BSA Enhanced Model S units. The 57N20 unit, BSA #1 which contained the 1 MHz reference master clock, measured the velocity component which corresponded to the 514.5 nm wavelength (green) beam. The second BSA, BSA #2, corresponded to the 488 nm wavelength (blue) beam.

Because the 57N35 units require a master clock for coincidence filtering, they were connected to the 57N20 unit with a "sync.bus" connector. The 40 MHz frequency shift, required by the Bragg cell, was generated by BSA #1. The cables from each photo multiplier tube were connected to the BSA corresponding to the particular wavelength of light. The BSA's were connected to the PC computer via an IEEE 488 standard connector interface [7].

#### 4.2.4 PC Computer and BURSTware Software

The BSA settings were controlled with Dantec BURSTware version 3.00 software, which was installed on the local PC computer [5]. This program served as an interface between the user and 3D LDV system. The computer was a Gateway 2000 486DX/33 PC with 4 Mbytes of RAM and a 200 Mbyte harddrive. The BURSTware program was configured to interface with all three BSA's. The only method for controlling BSA #2 and #3, because they lacked display and keyboard controls, was with this software. The traverse was also controlled with the software. BSA settings, such as bandwidth, center frequency, PM tube high-voltage, and data collection mode, could all be controlled and varied with the BURSTware software. The

processed data was exported from the software, and used with other in-house software [23] to present turbulent and mean flow results.

#### 4.3 Seeder Apparatus

The seeder apparatus consisted of two components; the atomizer and an injector. In order to introduce particles of known size and material property into the flow field, a TSI Incorporated Model 9306 6-jet Atomizer was used. The seed particles passed through a Tygon tubing hose placed in an opening in the settling chamber. An injector was mounted approximately 4 cm upstream of the flow straightener. Figure 4-8 shows the atomizer and seeder configuration.

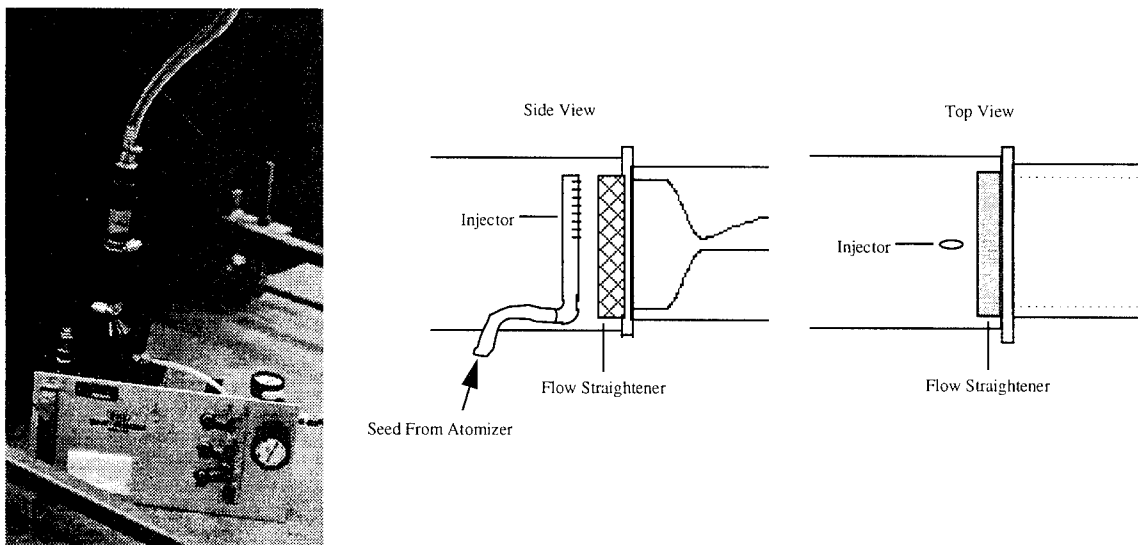


Figure 4-8: Six-jet Atomizer and Injector Schematic

The seed particles were generated by passing 100% pure olive oil through the atomizer. Air at 0.207 MPa entered the atomizer and produced an aerosol flow rate per jet of approximately  $7450 \text{ cm}^3/\text{min}$ . A linear relationship between flow properties and the number of

jets existed; the flow rate doubled when two jets were used. The diameter of the olive oil particles was nominally  $0.6 \mu\text{m}$ [29].

The flow injector was made of 1.25 cm diameter copper tubing. A  $90^\circ$  elbow was fitted on one end of the injector. The copper tubing was flattened to reduce the downstream wake produced. About 25 holes, which spanned a length of 7.5 cm, were cut in the top edge of the injector, which was mounted vertically in front of the flow straightener.. The Tygon tubing passed through a hole in the settling chamber and connected to the atomizer outlet.

#### 4.4 Flow Visualization

Schlieren and shadowgraph techniques were employed to make flow visualization studies. Figure 4-9 shows the flow visualization setup. A Polaroid camera using Type 57 black and white Polaroid film was used along with mirrors of focal length 1.53 m. The light source was a Xenon Nanopulser Model 437B with N787B spark light. The flash duration was 10 nanoseconds.

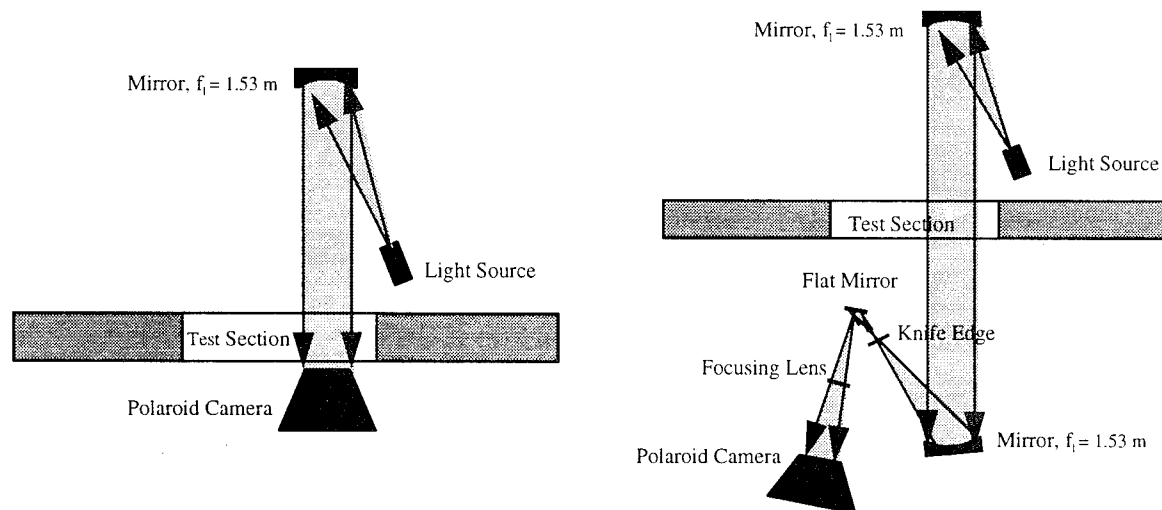


Figure 4-9: Shadowgraph and Schlieren Setup [15]

## *4.5 Computer Resources*

### *4.5.1 Personal Computer*

The author's home personal computer was used for data analysis, and document preparation. The computer was a 486DX33 PC with 8 Mbytes of RAM and a combined harddrive space of 550 Mbytes. Software resources included Microsoft Office v.4.3 applications, Mathsoft MathCad v.5.0+, and Golden Software Grapher v.1.23. Documents were printed on a Hewlett-Packard DeskJet 500 printer. Modem connection to AFIT provided file transfer and remote login capability to the Air Force Institute of Technology UNIX computer network.

### *4.5.2 AFIT Computer Resources*

The computer resources at the school included Sun Sparcstation 20, running in UNIX format, and laboratory PC, running in DOS and Windows. Network connections provided support for file transfer, data processing, and data storage.

## *5. Experimental Procedures*

This chapter describes the experimental procedures used for the present experiment. The primary measurement technique was Laser Doppler Velocimetry (LDV). As mentioned in Chapter 4, the LDV system contained the traverse, optics, and software necessary to perform the experiments. A description of data acquisition is also included.

### *5.1 Traverse Positioning*

The traverse, described in Chapter 4, was placed under the wind tunnel, which was about 1.0 meter above the floor, with its y-axis aligned with the tunnel. Thus, moving the traverse along its y-axis moved the measuring volume along the tunnel's centerline. The 2D optical probe was used to accurately align the traverse. The probe was rotated on its mounting stand until the angular variation from the axis of the mounting bench,  $\theta$ , was zero. Alignment marks on the mounting stand aided with this alignment. With the probe in this configuration, the laser was turned on causing the beams to pass through the optical glass windows on the tunnel. The laser beams produced reflections in the glass windows. The traverse was shifted until the reflections of the four laser beams returned into the 2D optical probe. The axes of the traverse were considered both parallel and perpendicular to the tunnel when this alignment was achieved.

### *5.2 Optical Alignment*

Several important factors were considered for correct optical alignment. These factors included forward-scatter setup, optical axis alignment, measurement profile origin positioning, and laser beam intersection adjustment.

### 5.2.1 Forward-scatter Mode

The Dantec 3D Laser Doppler Velocimetry system can be configured for both forward- and back-scatter collection modes. It was expected and verified during the present experiment, that the back-scatter mode would not generate a measurable signal. Hence, the receiving and transmitting optics were configured for forward-scatter collection mode, as directed in Ref. [6].

In forward-scattering mode, the receiving and transmitting optics are on opposite sides of the region to be analyzed; in this case, the test section of the wind tunnel. The probe mounts were placed near each end of the traverse's mounting bench. The offset angle,  $\theta$ , between the centerline of the mounting bench and the direction of the emitted laser beams was set at  $3.5^\circ$ . Figure 5-1 shows the forward-scattering setup. Both the 1D and 2D optical probes were oriented at this angle. This was the minimum angle that would allow the lasers from the transmitting probe to pass through the tunnel and not directly intersect the lens of the receiving probe. This setup was deemed necessary to insure that the very sensitive photo multiplier tubes were not destroyed. The bias error introduced into the velocity measurements was found to be negligible (See Appendix A).

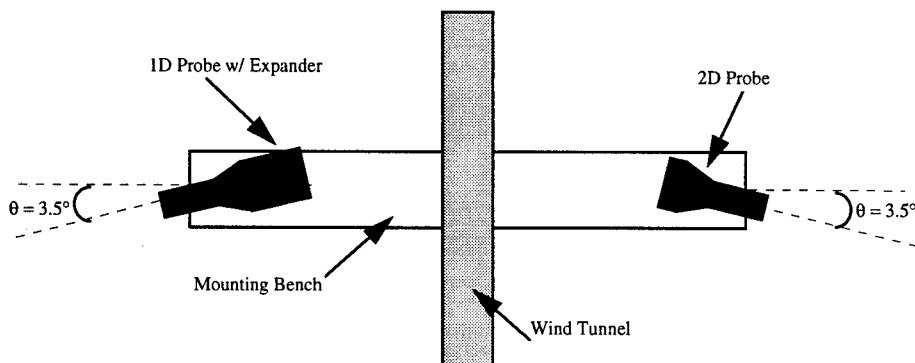


Figure 5-1: Forward-scattering Configuration

### 5.2.2 Optical Axis Alignment

As mentioned in Chapter 3, several optical axis configurations may be used in LDV measurements. To avoid the problems associated with angular bias [11], the optical axes were aligned to directly measure the u- and v-components of velocity. This process also negated the requirement of providing an optical transform for post-processing. The optical axes of the 2D probe were aligned with model test section body intrinsic coordinates; the u-component of velocity was aligned parallel to the wall, with the v-component of velocity normal to the wall. In the case of the flat plate, the u-component of velocity was aligned with the tunnel's x-axis, which corresponded to the y-axis of the traverse.

The orientation of the optics depended on the curvature of the model. Using Eq. (4.1), the slope of the line tangent to the model surface at a particular x-location was given as

$$Y'(x) = -0.541 + 0.14956(x) - 0.0084(x^2) \quad (5.1)$$

where x is measured in centimeters from the front of the test section. LDV measurements were made at two locations for the adverse pressure gradient case, x = 68 cm and x = 71 cm behind the throat of the nozzle, corresponding to positions 8 and 11 cm behind the front of the model, respectively. Flat plate measurements were also made at x = 71 cm, for comparison with the adverse pressure gradient case. These locations were determined by raising the traverse so that the probe volume was positioned just above the tunnel. An index card was placed on the centerline of the tunnel, and the location of the beam was positioned the required distance behind the front of the model. At x = 68 cm, the slope of the tangent line was 0.11788. At x = 71 cm, the slope of the tangent line was 0.08776. These slopes of the tangent lines at 68 and 71 cm corresponded to angular rotations of  $\phi = 6.72^\circ$  and  $\phi = 5.02^\circ$ , respectively, where  $\phi$  was measured relative to the horizon.

Once the proper distance from the nozzle was determined, the traverse was lowered until the beams were on the edge of the model. Clamps on the probe mounting were loosened, and the 2D optical probe was rotated through the angle  $\phi$  until the 488 nm beam (blue) appeared to be aligned parallel to the wall. Because the beams emitted from the probe were perpendicular, the 514.5 nm beam (green) was automatically aligned normal to the wall. In this configuration, the blue and green beams were set to measure the u- and v-components of velocity, respectively. Slight adjustments in the height of the traverse were required during this alignment. The orientation of the beams from the 1D receiving optics did not need to be adjusted relative to the 2D probe beam orientation.

### 5.2.3 Establishment of Data Profile Origin

Prior to making LDV measurements across the boundary layer, the origin for the data profile needed to be established. This location would provide a reference point from which the probe volume was adjusted. With the probe optics already aligned with the model coordinates, establishing the origin was achieved by adjusting the height of the laser beams until the "4 spot pattern" was centered on the edge of the model. In particular, the traverse was positioned so that half of each blue beam passed through the tunnel, and the other half was clipped by the model.

Figure 5-2 shows the origin configuration. The assumption was made that the tunnel was leveled in both its x- and y-axes.

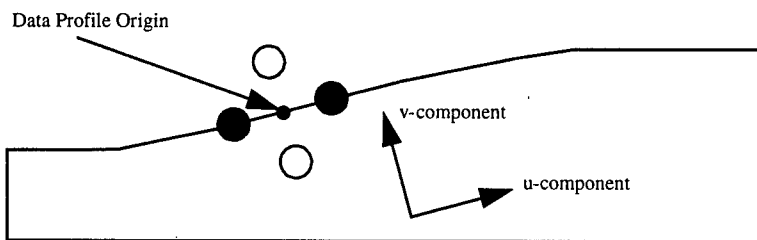


Figure 5-2: Data Profile Origin

#### 5.2.4 Laser Intersection Adjustment

With the optical axes aligned with the tunnel, and data collection origin established, the next step in the process was adjustment of the laser beams to ensure that the receiving optics were focused on the measurement volume, as described in Chapter 3. The violet (476.5 nm) components, which emitted from the receiving optics, were used to focus the optics. The 2D transmitting probe was adjusted such that the 6 beams, 2 of each wavelength, all intersected at the same region in space.

Fine tune alignments were monitored with the BURSTware program. There were two options available for data collection mode: online display, and acquire and save. These modes determine whether the acquired data is saved to disk, or only presented on the monitor. Online display mode was used to adjust the lasers. The BURSTware was configured so that each BSA had a center frequency of zero, and a bandwidth of about 30 m/s. (Details of the BURSTware configuration are found later in this chapter.) The seeder was turned on so that olive oil particles were introduced into the tunnel. Because neither the high-pressure air, or vacuum-suction was applied during laser alignment, the velocity of the particles was nearly zero. With the laser turned on, the particles were illuminated by the laser. The scattered light Doppler signals were detected by each BSA. Data were acquired for approximately 5 seconds. The online display showed the validation percent of each velocity component for the current alignment. By adjusting the micrometers of the 1D probe, the beam intersection alignment was adjusted until the validation percentages for both components were above 90%. The validation percent was the ratio of the number of validated bursts to the total number of detected bursts. The data rate and number of bursts collected were also important considerations during laser alignment. Data rates and number of collected bursts below 4 kHz and 4000 bursts, respectively, were unacceptable. Despite a high validation rate, the lasers were adjusted if either of these parameters was low.

This trial and error task proved to be challenging and time consuming. The validation percentages were very sensitive to slight adjustments; in fact, different validation percentages resulted when the micrometers were returned to previous settings. After the intersection of the laser beams was optimized, the optics of the LDV system were ready to make measurements.

### *5.3 BURSTware Configuration*

#### *5.3.1 Parameter Files*

The profiles, where LDV measurements were taken, were located perpendicular to the wall with the origin at the previously mentioned locations. Data were collected at about 15 locations across the boundary layer. The BURSTware software required a parameter file for each location. The parameter file included all the traverse and BSA settings to make the LDV measurements. All files associated with the same profile had the same filename. The length of these root names was limited to four characters. The run number, which corresponded to the location, was added to the root name. Parameter filenames were limited to six characters because the software used the last two, of the 8 character DOS filename, for other file designations [5]. Examples of parameter filenames were ADV101.par, ADV102.par, FLAT01.par, FLAT02.par, etc. The parameter files at each location were identical, except for a few variations. The center frequency, which corresponded to the mean velocity, was slightly increased as the LDV measurement location approached the edge of the boundary layer.

#### *5.3.2 BURSTware Menu Settings*

By selecting the Setup and Acquire option, the BURSTware entered the mode that would allow input of the necessary parameters. This option enabled parameter file management, optical

setup, BSA and traverse control, and data collection parameter assignment. This section details the BSA settings used for the current investigation.

The BURSTware software required information concerning the optics used by the LDV system. These settings were entered with the Optics option. The calibration factor,  $C_{fv}$ , which provided a direct frequency-velocity relationship, was based on the laser beam wavelength, beam separation distance, and focal length of the lens (see Chapter 3). The calibration factor was equivalent to the fringe spacing in  $\mu\text{m}$ . Table 5-1 summarizes the optical settings used for this investigation.

Table 5-1: BURSTware Optical Menu Settings

	BSA #1	BSA #2
Calibration (m/s/MHz)	8.128	7.709
Wavelength (nm)	514.5	488.0
Beam Separation (mm)	38	38
Focal Length (mm)	600	600

The size of the measurement volume, given in Table 5-2, was a direct result of these optical settings. The coordinate system used by the BURSTware is the same as in Figure 3-1. The probe volumes for both sets of laser beams were very elongated.

Table 5-2: Control Volume Measurements Settings

	BSA #1	BSA #2
Gaussian Beam Diam. (mm)	1.35	1.35
Beam Expander Ratio	1.0	1.0
Beam Collimator Ratio	1.0	1.0
$\Delta X$ (mm)	0.291	0.276
$\Delta Y$ (mm)	0.291	0.276
$\Delta Z$ (mm)	9.199	8.725

When the Acquire option was selected, specific data acquisition parameters could be entered using the traverse location, Quick setup, Softkey setup, Program setup, and Validation menu options. The traverse was moved to the proper data collection position before other settings were adjusted. This precaution was taken to ensure that the laser beams did not directly reflect off the tunnel and back into the optics. Such an event could permanently damage the photo multiplier tubes. Since most of the measurements were taken in the center of the tunnel, the x-location of the traverse was not moved. These locations originated at the origin and were perpendicular to the wall. The equations for the profile at  $x = 68$  was given by

$$z = -8.4832y \quad (5.2)$$

and, the equation for the profile at  $x = 71$  cm was

$$z = -11.3947y \quad (5.3)$$

These equations were derived by using the slopes of the tangent line at each location from Chapter 4. The slope of the normal line was the negative inverse of the slope of the tangent line. A few traverse coordinates for a sample profile across the boundary layer at  $x = 68$  cm are given in Table 5-3. While the accuracy of the traverse was much greater, the BURSTware software limited the traverse location to only  $\pm 0.01$  mm, which as discussed in the error analysis in Appendix A, was the largest source of uncertainty in the velocity measurements near the wall.

Table 5-3: Sample Traverse Coordinates

Parameter file number	Y coordinate	Z coordinate
01	0.07	-0.58
02	0.09	-0.76
03	0.11	-0.93
04	0.15	-1.27
05	0.2	-1.70
06	0.25	-2.12
07	0.3	-2.54

The settings of both BSA's were controlled from the Quick menu. These settings are detailed in Table 5-4. The center frequency and bandwidth gave the velocity range over which possible bursts may be detected. The largest possible bandwidth was selected to ensure collection of a wide range of velocities. With the frequency shift enabled, a wider range of center frequency and bandwidth settings was possible. The record length was the number of samples used by the BSA to digitize a Doppler burst. Signal gain amplified the incoming signal, while the pedestal attenuation reduced the pedestal component of the input signal. The maximum anode current was limited by the type of photo multiplier tubes [8]. The high voltage to the photo multiplier tubes needed to be enabled to allow for measurements within the specified velocity range. The high voltage to BSA #2 was higher because the power of the green beams was less than that of the blue beams.

Table 5-4: BURSTware Quick Menu Settings

		BSA #1	BSA #2
Velocity Units		m/s	m/s
Center Frequency		≈ 480	≈ 390
Bandwidth		325.12	246.7
Shifter Mode		Norm	Norm
Record Length		16	16
Signal Gain (dB)		42	42
High Voltage (V)		1304	1504
Max. Anode Current		1.6	1.6
Pedestal Attenuation		6	6
Duty Cycle (%)		100	100
Dead Time (msec)		0	0
High Voltage On ?		Yes	Yes

After the Quick menu settings were entered, the Program menu settings were entered. The number of bursts to be collected, and type of data to be recorded were selected with this option. For the present investigation, data was collected for 12 seconds, or until 150000 bursts

were recorded by either BSA. Since the timeout criteria was always fulfilled before the maximum number of bursts was collected, the number of bursts varied from location to location. Near the wall, the number of bursts was lower than that in the freestream. In any event, the minimum number of bursts at a single location was 6000. The remaining three settings determined what type of data was recorded in the raw, or pre-coincidence filtering, data files. Transit time is the amount of time the particle was in the control volume. Arrival time, which must be enabled for coincidence filtering, related the time the particle was first detected by the BSA. Obviously, the velocity must be recorded to enable analysis of velocity fluctuations and turbulent quantities. Table 5-5 shows the exact settings used in this experiment.

Table 5-5: BURSTware Program Menu Settings

	BSA #1	BSA #2
Timeout (sec)	12	12
Number of Bursts	150000	150000
Velocity	Yes	Yes
Transit Time	Yes	Yes
Arrival Time	Yes	Yes

The Softkey menu option allowed BSA settings, not included in the Quick menu option, to be entered. Table 5-6 lists the settings used in this study. BSA #2 used the master clock contained in BSA #1. The coincidence mode settings were selected so that the second BSA would search for a burst after it was triggered by the first BSA. Both the pedestal and envelope of the Doppler signal were used for burst detection. The FiFo buffer mode, referred to "first in, first out" mode, allowed simultaneous transmission and storage of data. The FiFo buffer was set at 4000 bursts. Individual Doppler bursts were counted because the data collection mode was set to burst. When 4000 bursts were detected, the data was transferred to storage, and another 4000 bursts were acquired. This process was repeated until the maximum number of requested bursts

was reached, or the timeout setting had expired. The quality factor was the ratio between the envelope and pedestal levels. A Doppler signal was accepted if it had a quality factor equal to or greater than the specified value. The oversize rejection parameter, which rejected oversized particles, was disabled for this experiment.

Table 5-6: BURSTware Softkey Menu Settings

	BSA #1	BSA #2
Timer Clock	Master	Slave
Coincidence Mode	Master	Slave
Arrival Time Base	Internal	Internal
Burst Detection	Both	Both
Oversize Rejection	1	1
Buffer Mode	FiFo	FiFo
Max. Anode Current	1.6	1.6
Quality Factor (%)	50	50
Collection Mode	Burst	Burst

The Validation option allowed the specification of what type of data was to be recorded by each BSA. Only two options were available for this parameter: All Data, or Valid Data. Only valid data was recorded by each BSA for this experiment.

Once these parameters were entered, data collection could take place. The high voltage to the PM tubes was enabled at this time. The Start option initiated data acquisition according to the given parameter settings. The BURSTware was now ready to make LDV measurements with the current settings.

### 5.3.3 BURSTware Post-processing

Once Doppler burst data had been collected, the Process option of the software was used to initiate and monitor data processing and conversion. The type of data to be computed was selected with the Setup option. For this experiment, velocity data, coincidence filtering, and

moment data files were processed. The coincidence window was set at 0.000333 msec. The effects of the size of the coincidence window were evaluated by varying it one order of magnitude above and below 0.000333 msec, with no apparent change in results. An optical transform was not required because the optics were measuring the actual components of velocity. After processing, both pre- and post-coincidence moment files, which included all mean and turbulent statistics from the data collection run, were exported. The default file extension, .lst, was used. These moment files would be used later by other FORTRAN processing codes [23] to determine turbulent statistics, and flow properties. Post-processing took about 5 minutes, which provided enough time to prepare the LDV system for data collection at the next traverse station. In other words, during the time required to empty the vacuum tanks, the data could be processed and reviewed before the traverse was moved to the next data location.

#### *5.4 Overview of a Typical Data Profile*

The following section outlines the experimental procedure for data collection at a single traverse station. While waiting for the vacuum tanks to be evacuated, the measurement volume was moved to the proper station. The wind tunnel was ready to run when the vacuum pressure was below 15 mmHg. With the parameter file prepared, the computer was ready to acquire data. The first step in running the tunnel was to open the vacuum gate valve. Then, the high-pressure solenoid valve was opened. This order, first vacuum, and then high-pressure was imperative. Once the tunnel was started, two jets of the atomizer where opened introducing seed particles into the flow field. A delay time of about 5 seconds allowed the flow field to stabilize. The computer data acquisition was begun after this delay period. Doppler bursts were collected for 12 seconds. The minimum number of bursts collected was 6000. However, in some cases, as many as 135000 bursts were collected. For most of the data, approximately 65000 bursts were

collected. After the data collection period expired, the atomizer was shut off. Finally, the tunnel was shut down, by closing the solenoid switches in reverse order. Turning the seed particles off before shutting off the tunnel evacuated all of the olive oil from the tunnel. This was found to reduce the oil sediments on the windows. During the tunnel recharge time, the newly acquired data was processed.

This same procedure was repeated until the boundary layer had been sufficiently mapped. It should be noted that only two parameter files needed to be created; one for the single-component locations, and one for the two-component stations. Because the first four data acquisition locations of each profile were in close proximity of the wall, only single component velocity measurements were collected. The green beams were clipped by the wall, and an accurate signal was not possible. Thus, BSA #2 was disabled, and the parameter files for these single component runs were configured to only measure the u-component of velocity along the wall. These two files were used as templates for the remaining parameter files. In this manner, the numerous BSA settings were copied into a new parameter file without the need to tediously re-enter each setting.

The deposit of olive oil, and other particles, on the glass windows interfered with the laser beams, by causing the light to be scattered. Hence, the windows of the tunnel were periodically removed and cleaned with distilled water and a very soft cloth, to ensure that the optical glass was not scratched.

Vibrations in the floor due to the vacuum pumps caused slight changes in the micrometer settings; resulting in misalignment of the receiving and transmitting probe volumes. Thus, the lasers were periodically realigned according to the previously mentioned procedure when this occurred.

## 6. Data Reduction Procedures

### 6.1 Calculation of Velocity

The Doppler frequency, as calculated by the Burst Spectrum Analyzer, is converted into the velocity of the particle by using the frequency-velocity calibration factor,  $C_{fv}$ . The calibration factors, as given in Chapter 5, for the u- and v-component of velocity are

$$C_{fv,u} = 8.128 \frac{m/s}{MHz}, C_{fv,v} = 7.709 \frac{m/s}{MHz} \quad (6.1)$$

Recall, these factors are based on the optical setup and wavelength of the laser beams used. Once the instantaneous velocities,  $u$  and  $v$ , are measured, the mean,  $\bar{u}$  and  $\bar{v}$ , and fluctuating,  $u'$  and  $v'$ , components of velocity may be calculated.

### 6.2 Calculation of Mach Number, Temperature, Density, and Pressure

The Mach number at each traverse station was calculated with the local measured velocity and total temperature. The flow was assumed adiabatic. For turbulent flow, mean and fluctuating terms are substituted into the relationship between temperature, stagnation temperature, and Mach number. The adiabatic relation

$$\frac{T_o}{T} = 1 + \frac{\gamma - 1}{2} M^2 \quad (6.2)$$

becomes

$$\bar{T} \left( 1 + \frac{T'}{\bar{T}} \right) = \frac{\bar{T}_o + T'_o}{1 + \frac{\gamma - 1}{2} (\bar{M} + M')^2} \quad (6.3)$$

when the expanded temperatures and Mach number are included. Based on the assumption of small fluctuating Mach numbers and the Strong Reynolds Analogy (SRA), Morkovin [28] derived a first order approximation for the ratio of fluctuating and mean temperature as

$$\frac{T'}{\bar{T}} = -(\gamma - 1) \bar{M}^2 \left( \frac{u'}{u} \right) \quad (6.4)$$

The Strong Reynolds Analogy, based upon the similarity between the compressible momentum and energy equations when  $\text{Pr} = 1$ , states that  $T'_o / \bar{T}_o$  is zero for adiabatic flows. With these assumptions, the local Mach number may be calculated by

$$\bar{M} = \left[ \frac{2\bar{Q}^2}{2\gamma R \bar{T}_o - \bar{Q}^2(\gamma - 1)} \right]^{1/2} \quad (6.5)$$

The Reynolds averaged total velocity,  $\bar{Q}$ , is given by

$$\bar{Q} = \sqrt{\bar{u}^2 + \bar{v}^2} \quad (6.6)$$

This local Mach number is calculated assuming a constant total temperature,  $T_o$ , through the boundary layer. Kistler [20] verified this assumption for the flat plate case. He found that within the supersonic boundary layer ( $M_e \in 1.7, 3.56$ ),

$$\frac{T_{o,\infty} - T_0}{T_{o,\infty} - T_{aw}} \leq 0.6 \quad (6.7)$$

where the adiabatic wall temperature,  $T_{aw}$ , is calculated using the adiabatic recovery factor,  $r \approx \sqrt[3]{\text{Pr}}$ , and the relationship

$$r = \frac{T_{aw} - T_e}{T_{o,\infty} - T_e} \quad (6.8)$$

with,  $T_e$ , being the temperature at the edge of the boundary layer. Assuming  $\text{Pr} = 0.71$ , the recovery factor is  $r = 0.892$ . Eq. (6.7) may be rewritten, in terms of the Mach number at the edge of the boundary layer,  $M_e$ , as

$$\frac{T_{aw}}{T_{o,\infty}} = \frac{1 + r[(\gamma - 1)/2]M_e^2}{1 + [(\gamma - 1)/2]M_e^2} \quad (6.9)$$

For the present flat plate case,  $M_e = 2.9$ , and  $T_{aw}/T_{o,\infty} = 0.932$  from Eq. (6.9). Thus,  $T_o/T_{o,\infty} \approx 0.96$ , which is nearly constant.

To calculate the density, the assumption that the pressure gradient normal to the surface,  $\partial p/\partial n$ , equals zero, was used. While this assumption is valid for the flat plate case, it does not necessarily hold for flows with adverse pressure gradient. Streamlines near a curved wall surface will experience curvature, and a pressure gradient normal to the streamlines will be generated. According to Spina [28], the magnitude of these gradients is

$$\frac{\partial p}{\partial n} \approx \frac{-\rho u^2}{R} = \frac{-\gamma M^2 p}{R} \quad (6.10)$$

where  $R$  is the radius of curvature. The difference in pressure between the wall and boundary layer edge is

$$\Delta p \approx \gamma M_e^2 p_e \left( \frac{\delta}{R} \right) \quad (6.11)$$

The change in pressure at the  $x = 68$  cm APG station was calculated as 12500 Pa. At the  $x = 71$  cm APG location, the change in pressure across the boundary layer was -27500 Pa. The

edge pressure was calculated by assuming that no shocks existed in the freestream. Thus, with constant total pressure along the boundary layer edge, the edge pressure is given as

$$p_e = p_o \left[ 1 + \frac{\gamma - 1}{2} M_e^2 \right]^{\frac{-\gamma}{\gamma - 1}} \quad (6.12)$$

where  $M_e$  was measured as described above.

By assuming constant total temperature and pressure across the boundary layer, the Crocco-Busemann approximation can be used to determine the mean temperature and density,  $\bar{T}$  and  $\bar{\rho}$ , based on the temperature and density at the wall,  $T_w$  and  $\rho_w$  [32]:

$$\frac{\rho_w}{\bar{\rho}} = \frac{\bar{T}}{T_w} = 1 + B' \left( \frac{\bar{u}}{u_e} \right) - A'^2 \left( \frac{\bar{u}}{u_e} \right)^2 \quad (6.13)$$

where, the coefficients are defined as

$$A'^2 = \frac{[(\gamma - 1)/2] r M_e^2}{T_w / T_e} \quad (6.14)$$

$$B' = \frac{1 + [(\gamma - 1)/2] r M_e^2}{T_w / T_e} - 1 \quad (6.15)$$

Using the perfect gas law and the wall temperature, the density at the wall is given by

$$\rho_w = \frac{P_w}{R T_w} \quad (6.16)$$

where  $R$  is the gas constant.

### 6.3 Calculation of Boundary Layer, Displacement, and Momentum Thickness

Boundary layer thicknesses based on both the Mach number ( $\delta_M$ ), and u-component of velocity ( $\delta_u$ ) were calculated. These parameters were calculated to enable comparison between conventional mean flow probe (Pitot and cone-static pressure) data [9] which result in direct measurements of the Mach number and the present LDV data. In this experiment, each boundary layer thickness was based on 99.5% of the edge value. Thus, the velocity and Mach number profiles were non-dimensionalized by the edge values, and the location above the wall where each quantity was 99.5% of the edge value was determined. The compressible displacement,  $\delta^*$ , and momentum,  $\Theta$ , thicknesses are defined, respectively, as

$$\delta^* \equiv \int_0^\infty \left( 1 - \frac{\bar{\rho} \bar{u}}{\rho_e u_e} \right) dy \quad (6.17)$$

and

$$\Theta \equiv \int_0^\infty \frac{\bar{\rho} \bar{u}}{\rho_e u_e} \left( 1 - \frac{\bar{u}}{u_e} \right) dy \quad (6.18)$$

The incompressible displacement thickness,  $\delta_i^*$ , and momentum thickness,  $\Theta_i$ , were also calculated by setting the density ratio,  $\bar{\rho}/\rho_e$ , in Eqs. (6.17) and (6.18) equal to one.

### 6.4 Calculation of Turbulent Statistics

As previously noted in Chapter 2, the characteristics of turbulent flow are analyzed by separating the flow properties into a mean and fluctuating component. Time-averaged quantities are used in the turbulence analysis because the randomness of turbulence makes exact calculation of flow properties impossible. By introducing the separated mean and fluctuating quantities,

statistical correlations involving the fluctuations and their products are introduced into the equations of motion [35]. These statistical methods are used to help provide plausible solutions to the governing equations.

These turbulent statistics also help to characterize turbulent flow. The fluctuating component may be positive or negative; its time average is, by definition, equal to zero. The average size of the fluctuating term is characterized by the root-mean-square (RMS) value of the fluctuation. The RMS value, or standard deviation, is defined as

$$x_{RMS} \equiv \sqrt{\frac{\sum (x')^2}{n}} \quad (6.19)$$

where there are  $n$  samples in the summation term. The variable,  $x$ , may represent either u- or v-component of velocity. The RMS value is also used to determine higher-order moments such as the skewness and flatness factors. The skewness ( $Sk_x$ ), and flatness ( $Fl_x$ ) factors are given by

$$Sk_x \equiv \frac{\sum (x')^3}{x_{RMS}^3 n} \quad (6.20)$$

$$Fl_x \equiv \frac{\sum (x')^4}{x_{RMS}^4 n} \quad (6.21)$$

The skewness factor is a method of quantifying to which side of the mean the majority of data points are. Negative skewness values indicate that more values are below the mean. These two turbulent statistics help determine if there are seeding biasing problems in the LDV results [12]. Equations (6.19) - (6.21) are not the unbiased statistical estimates. The denominator should be divided by  $n - 1$  instead of  $n$ . However, since the minimum number of points exceeded 6000

for all data, this resulted in less than a 0.01% bias. Thus, it was deemed acceptable to use the BURSTware results.

The intermittency factor,  $\gamma_u$ , is another valuable turbulence statistic, that helps to describe the flow. The edge of a turbulent boundary layer is not always turbulent. The turbulence becomes intermittent, where there are intervals of time when the flow is not turbulent. The intermittency factor is the ratio of the flattening factors in the wholly turbulent region to that of the intermittent region. Near the wall, where the flow is wholly turbulent, the flattening factor is near a constant value of 3.0 [21]. Thus, the intermittency factor is given by

$$\gamma_u = \frac{3.0}{Fl_u} \quad (6.22)$$

The distribution of the intermittency function is compared to a Gaussian integral curve given by

$$\gamma_u = 0.5(1 - erf\chi) \quad (6.23)$$

where

$$\chi = \left( \sqrt{2} \frac{\zeta}{\delta_u} \right)^{-1} \left[ \frac{y}{\delta_u} - \varphi \right] \quad (6.24)$$

and

$$erf\chi \equiv \frac{2}{\sqrt{\pi}} \int_0^{\chi} e^{-t^2} dt \quad (6.25)$$

The constants  $\zeta$  and  $\varphi$  are adjusted until the Gaussian curve matches the calculated distribution. The constant  $\zeta$  is the standard deviation of the boundary layer edge from  $\varphi$ . The mean position of the turbulent boundary layer edge is then located at  $y/\delta = \varphi$  [21].

The velocity correlation,  $\overline{u'v'}$ , is one of the new terms that results in the RANS equations. When multiplied by the average density, this term becomes the first term in the Reynolds shear stress, or as discussed in Chapter 2 [Eq. (2.13)], the Favre shear stress. The velocity correlation is given by

$$\overline{u'v'} = \sum (u'v')/n \quad (6.26)$$

The velocity correlation coefficient,  $R_{uv}$ , is defined as

$$R_{uv} = \frac{\overline{u'v'}}{u_{RMS} v_{RMS}} \quad (6.27)$$

This term can be used as a measure of the anisotropy of the turbulent flow. For isotropic flow,  $|R_{uv}| = 1.0$ . The Cauchy-Schartz [2] inequality dictates that  $|R_{uv}| \leq 1.0$ . For incompressible boundary layers, this term is nominally 0.5 [3].

The turbulent kinetic energy (TKE) provides a measure of the turbulent energy within the boundary layer. TKE is defined as

$$TKE \equiv \frac{(u')^2 + (v')^2 + (w')^2}{2} \quad (6.28)$$

The w-component of velocity could not be measured with the configuration of the LDV for the present study. Thus, the fluctuating velocity,  $w'$ , could not be measured. To estimate the value of the TKE, it was assumed that the fluctuations,  $v'$  and  $w'$ , were the same order of magnitude. Hence, the estimated TKE was given by

$$TKE \approx \frac{(u')^2 + 2(v')^2}{2} \quad (6.29)$$

Each of these turbulent quantities and statistics was calculated at each traverse station across the boundary layer. The results, and comparisons, with the data in the literature are given in Chapter 7.

### 6.5 Calculation of Wall Shear Stress

The flat plate wall shear stress,  $\tau_w$ , is an important parameter that will be used later for the inner region (law of wall) van Driest velocity profile. Van Driest [3] gives the relation as

$$\frac{0.242}{A' \sqrt{C_f (T_w/T_e)}} \left[ \sin^{-1} \left( \frac{2A'^2 - B'}{\sqrt{4A'^2 + B'^2}} \right) + \sin^{-1} \left( \frac{B'}{\sqrt{4A'^2 + B'^2}} \right) \right] = \kappa + \log(\text{Re}_x C_f) - \omega \log(T_w/T_e) \quad (6.30)$$

where  $\kappa = 0.41$ ,  $\omega = 0.68$ , and  $A'^2$  and  $B'$  are as previously defined. Eq. (6.30) must be solved iteratively for the skin friction,  $C_f$ . Once the skin friction has been calculated, the wall shear stress may be calculated using

$$\tau_w = \frac{2C_f}{\rho_e u_e^2} \quad (6.31)$$

### 6.6 Calculation of Van Driest Velocity Profile

Van Driest [32] proposed a transformation to the velocity profile, so that compressible flows could be compared. The effective velocity,  $u_{eff}$ , is given by

$$u_{eff} = \frac{u_e}{A'} \left[ \sin^{-1} \left( \frac{2A'^2 (\bar{u}/u_e) - B'}{\sqrt{4A'^2 + B'^2}} \right) + \sin^{-1} \left( \frac{B'}{\sqrt{4A'^2 + B'^2}} \right) \right] \quad (6.32)$$

The effective velocity is non-dimensionalized by the wall-friction velocity,  $u^*$ , where

$$u^* = \sqrt{\frac{\tau_w}{\rho_w}} \quad (6.33)$$

The non-dimensional velocity,  $u_{eff}/u^*$ , is plotted versus another scaled y-coordinate given as

$$y^+ = \frac{yu^* \rho_w}{\mu_w} \quad (6.34)$$

where  $\mu_w$  is the fluid viscosity calculated at the wall temperature. White [34] gives an empirical relationship between these two quantities for the flat plate case:

$$\frac{u_{eff}}{u^*} = \frac{1}{\kappa} \ln y^+ + C + \frac{2\Pi}{\kappa} \sin^2 \left( \frac{\pi}{2} \frac{y}{\delta} \right) \quad (6.35)$$

with  $\kappa = 0.41$  and  $C = 5.0$ . Cole's wake parameter,  $\Pi$ , is given by

$$\Pi \approx 0.8(\beta + 0.5)^{3/4} \quad (6.36)$$

where  $\beta$  is Clauser's equilibrium parameter,

$$\beta \approx \frac{\delta^*}{\tau_w} \frac{dp_e}{dx} \quad (6.37)$$

Equation (6.35) incorporates the overlap log law formulation with Coles law of the wake term. This equation was developed for low-speed data, but the van Driest transformation collapses high-speed data to this form as well. The region below  $y^+ \approx 10$ , where the flow becomes laminar, is called the laminar sublayer. In this region,  $u^+ = y^+$ .

## 6.7 Calculation of Strain Rates

Central-difference strain rates were calculated on the APG model. The central location  $(i,j)$ , was located 71 cm from the throat of the nozzle. Figure 6-1 shows the finite-difference grid.

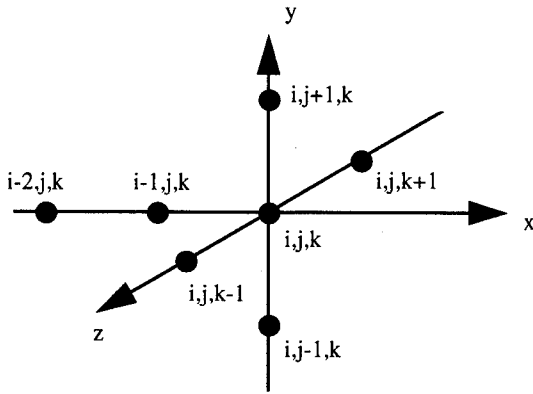


Figure 6-1: Finite-Difference Grid

The central-derivatives at the point  $(i, j, k)$  are estimated as [1]:

$$\left. \frac{d\bar{u}}{dy} \right|_{i,j,k} = \frac{\bar{u}_{i,j+1,k} - \bar{u}_{i,j-1,k}}{y_{i,j+1,k} - y_{i,j-1,k}} \quad (6.38)$$

$$\left. \frac{d\bar{u}}{dz} \right|_{i,j,k} = \frac{\bar{u}_{i,j,k+1} - \bar{u}_{i,j,k-1}}{y_{i,j,k+1} - y_{i,j,k-1}} \quad (6.39)$$

$$\left. \frac{d\bar{u}}{dx} \right|_{i,j,k} = \frac{(dx_1^2)\bar{u}_{i-2,j,k} - (dx_2^2)\bar{u}_{i-1,j,k} + (dx_2^2 - dx_1^2)\bar{u}_{i,j,k}}{(dx_2 dx_1^2 - dx_1 dx_2^2)} \quad (6.40)$$

where  $dx_1 = x_{i-1,j,k} - x_{i,j,k}$  and  $dx_2 = x_{i-2,j,k} - x_{i,j,k}$ . The strain rates for the v-component of velocity may also be calculated by substituting  $\bar{v}$  for  $\bar{u}$  in Eq. (6.38)-(6.40).

## 7. Experimental Results

The results of this investigation are presented in this chapter. Laser Doppler Velocimetry measurements were taken for both the adverse pressure gradient, using the compression ramp model, and the zero pressure gradient, or flat plate case. These measurements were made at three locations downstream of the nozzle; at  $x = 44$  and  $71$  cm for the flat plate, and at  $x = 68$  and  $71$  cm for the compression ramp model. Both the flat plate mean flow and turbulence results of the present study are compared to those results of other researchers. In this way, the LDV methods used in the present study may be validated. Then, the mean flow and turbulence results of the compression ramp model are compared to the flat plate results to determine the effect of the adverse pressure gradient on the turbulent boundary layer. Table 7-1 summarizes the boundary layer edge conditions for all three measurement locations and test models.

Table 7-1: Boundary Layer Edge Conditions

	Flat Plate $x = 44$ cm	Flat Plate $x = 71$ cm	Adverse Pressure $x = 68$ cm	Favorable Pressure $x = 71$ cm
$M_e$	2.87	2.79	2.72	2.51
$u_e$	605.0 m/s	602.0 m/s	596.0 m/s	575.0 m/s
$T_e$	111.0 K	116.0 K	120.0 K	131.0 K
$p_e$	6823.0 Pa	7866.0 Pa	8917.0 Pa	11985.0 Pa
$\rho_e$	0.213 kg/m <sup>3</sup>	0.237 kg/m <sup>3</sup>	0.258 kg/m <sup>3</sup>	0.319 kg/m <sup>3</sup>
$dp_w/dx$	0	0	1250 Pa/cm	-1900 Pa/cm
$\beta$	0	0	1.12	-0.94

### 7.1 Flat Plate Results

LDV measurements were made on the flat plate model in the same location as those made in the pressure gradient case for two reasons. The first reason was to provide a method of

comparing the flat plate LDV results from the present study to those of other accepted data from the literature. A few of these studies have incorporated LDV as the measurement technique (Ref. [12, 18-19, 25]). The second reason for making LDV measurements on the flat plate at the same location was to provide a means of assessing the effects of the adverse pressure gradient on the turbulent boundary layer from those of the flat plate at the same location. In this manner, the effects of the pressure gradient could be distinguished from the flat plate. Using the same AFIT facilities and compression ramp model, Dotter [9] used Pitot and cone static methods, and hot-wire anemometry to perform a similar investigation. Hence, the present data will be compared to those of Dotter as well.

### 7.1.1 Flat Plate Mean Flow Results

The flat plate LDV profile measurements were made at 44 and 71 cm downstream of the nozzle. Both of these locations were chosen to compare with the flat plate and APG results of Dotter. The edge velocities at the 44 and 71 cm flat plate locations were  $605.0\text{ m/s}$  and  $602.0\text{ m/s}$ , respectively. The velocity boundary layer thicknesses based on a 99.5% criteria were 5.73 mm and 9.86 mm.

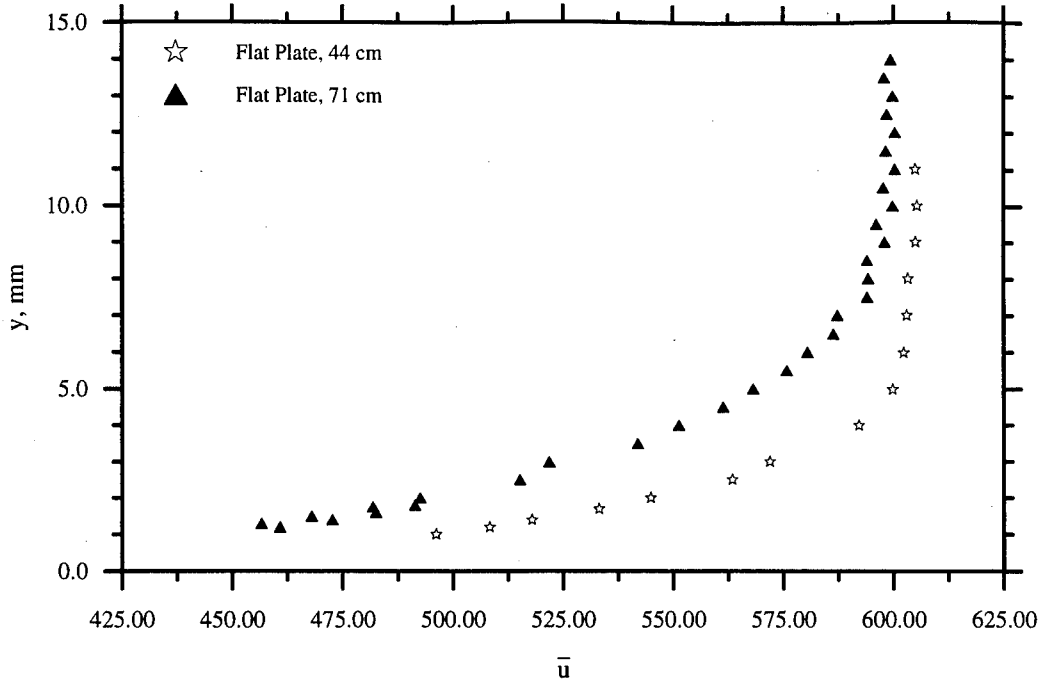


Figure 7-1: Flat Plate Velocity Profile,  $x = 44$  and  $71$  cm

The velocity profiles were non-dimensionalized by the freestream velocity. Figure 7-2 presents the non-dimensionalized velocity profiles versus  $y/\delta$ . Also shown are the Pitot-cone static results from Dotter [9]. As can be seen, the agreement is excellent. Note that Dotter's results were scaled by  $\delta_M$ , the Mach number boundary layer thickness. In order to correctly compare, those results were rescaled to the present boundary layer thickness.

Unfortunately, LDV measurements with the optical quality windows at 44 cm were not possible because the windows could not be placed at this location. Hence, the measurements were taken through 1.91 cm thick Plexiglas. It was anticipated that the LDV results would be distorted. To the contrary, the LDV results matched Dotter's conventional pressure probe results, as is evidenced by the profiles in Figure 7-2.

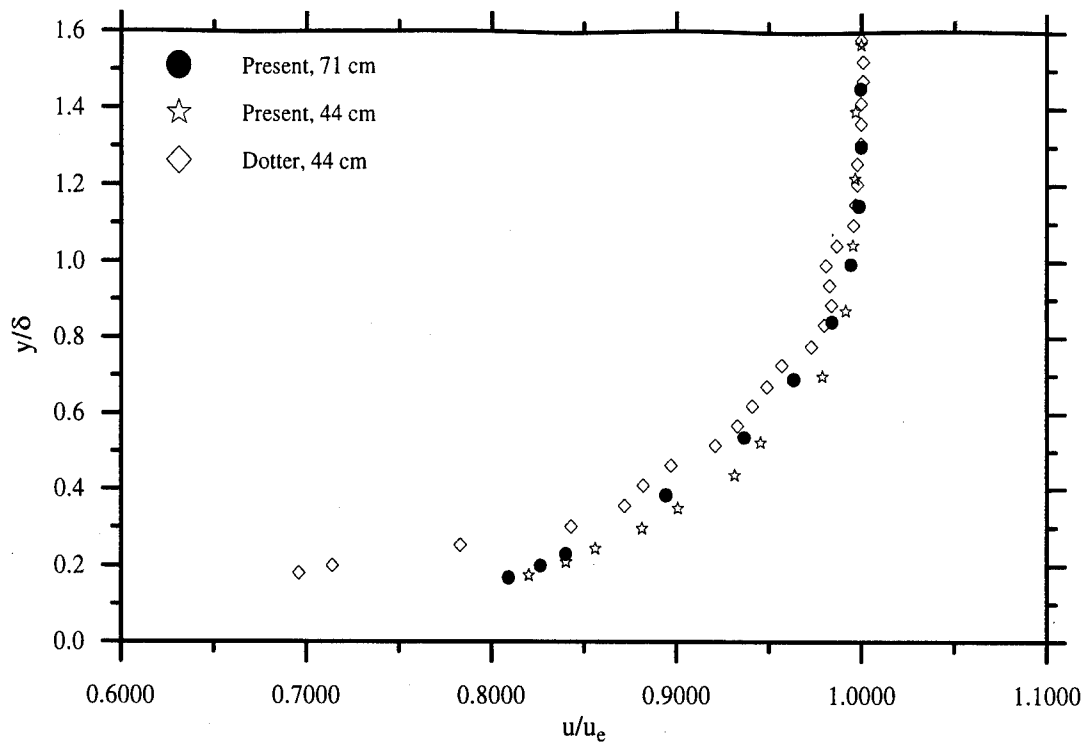


Figure 7-2: Flat Plate Non-dimensional Velocity Profiles,  $x = 44$  and  $71$  cm

The flat plate Mach number profiles at both locations are presented in Figure 7-3. At 44 cm, the edge Mach number measured 2.9 and the Mach based boundary layer thickness,  $\delta_M$ , was 8.20 mm. At 71 cm, the edge Mach number was 2.8, and  $\delta_M$  measured 10.82 mm. As expected, the boundary layer thickness over the flat plate increased between the locations. The difference in Mach number at the two stations was the result of increased boundary layer thickness in the constant area test section.

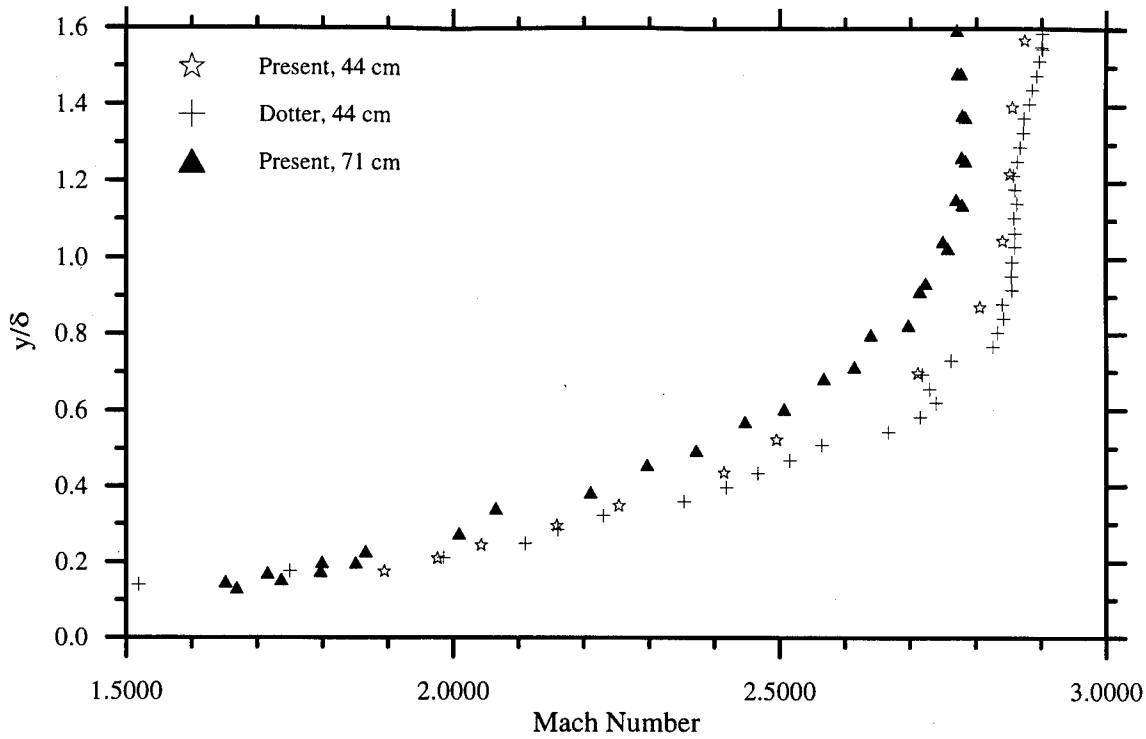


Figure 7-3: Flat Plate Mach Number Profiles,  $x = 44$  and  $71$  cm

### 7.1.2 Flat Plate Turbulence Results

#### 7.1.2.1 Flat Plate Turbulence Intensities

The u- and v-velocity turbulence intensities are presented in Figures 7-4 and 7-5. Elena and LaCharme [12], and Robinson et al. [25] made LDV measurements in Mach 2.9 flat plate flow. Kistler [20] made hot-wire measurements in the listed range of Mach numbers. The Klebanoff curve [21] shows the incompressible turbulence intensities measured with hot-wire anemometry for flat plate flow. Finally, Dotter's [9]  $x = 44$  cm cross-wire results are included. In particular, comparisons with the results of Elena, Robinson, and the present study are important because the LDV technique was used in each case. For both turbulence intensities, the agreement with the present results is remarkable. The present LDV results very closely resemble

the results of Elena and LaCharme. Johnson's v-component turbulence intensity results match slightly better with the present data than the u-component results. The Klebanoff hot-wire data also agrees very well with the present data. However, the Kistler and Dotter turbulence intensity levels were consistently off. This could be a result of the convenient assumption used in both studies that the static pressure fluctuations are zero. These figures also indicate that the freestream turbulence of the AFIT Mach 3.0 wind tunnel was approximately 1.0%.

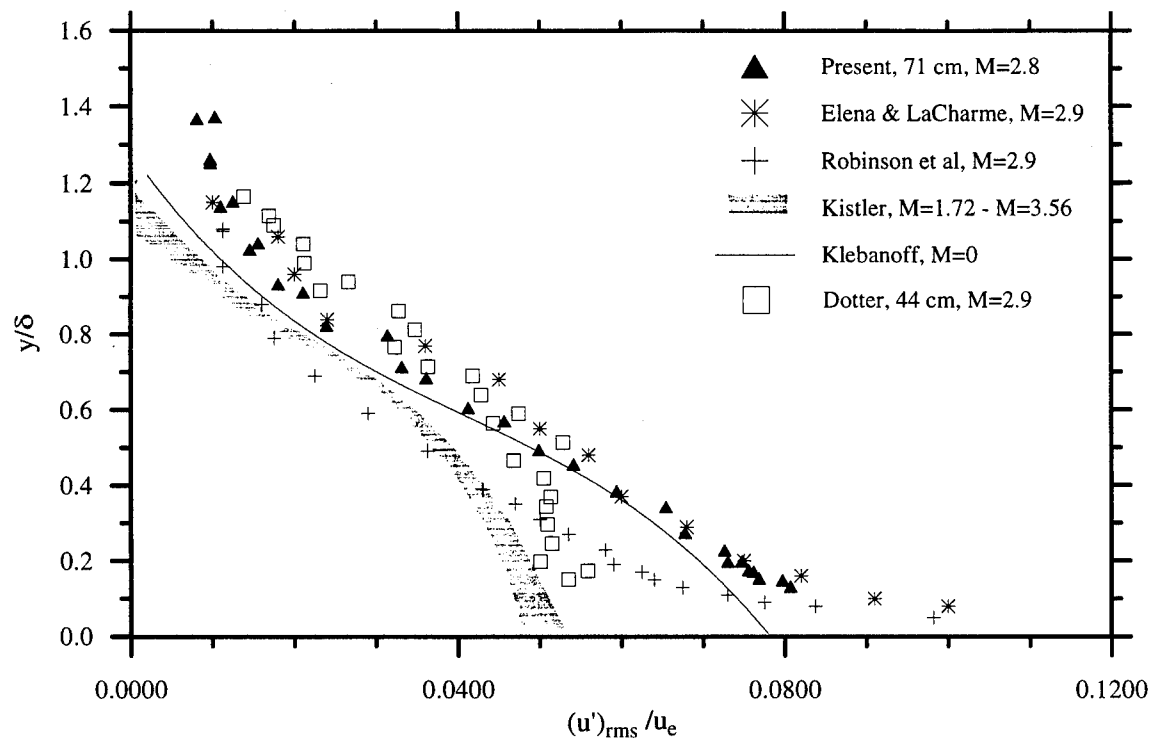


Figure 7-4: Flat Plate u-component Turbulence Intensities

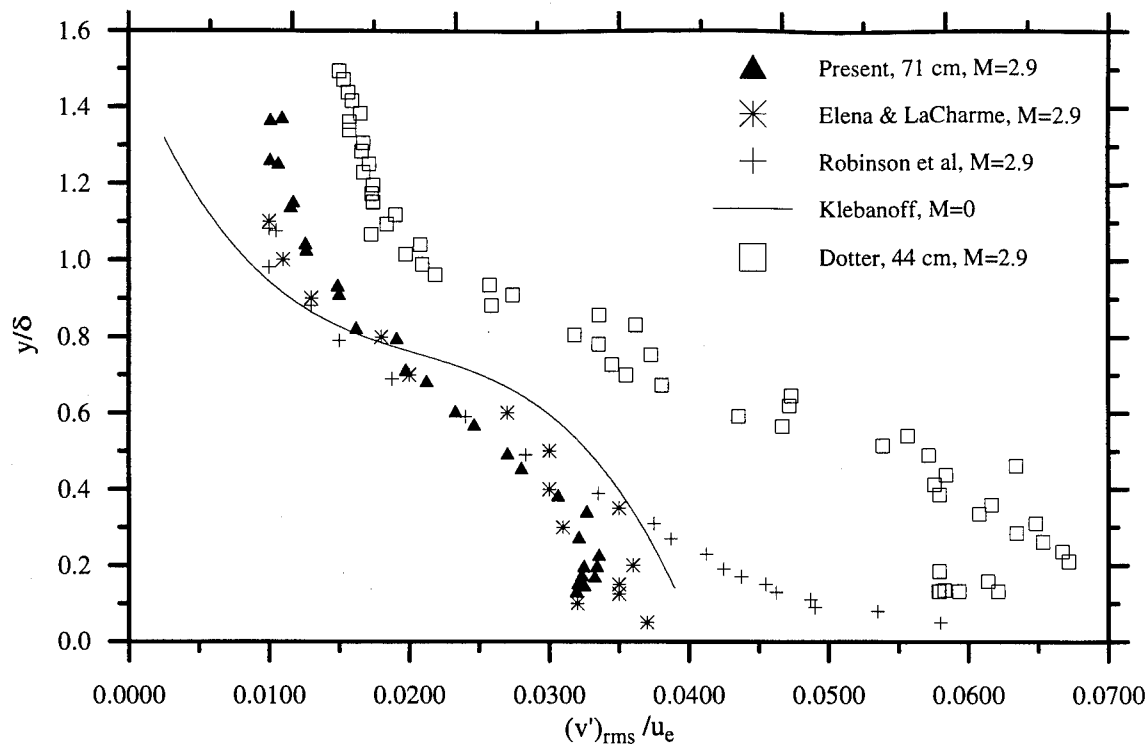


Figure 7-5: Flat Plate v-component Turbulence Intensities

#### 7.1.2.2 Flat Plate Reynolds Shear Stress

The turbulent shear stresses for the flat plate at 71 cm are presented in Figure 7-6. Note, to scale the present results as shown in Figure 7-6, the van Driest skin friction law and Crocco integrals (see Chapter 6) were used. The wall shear stress was estimated as approximately 67 Pa for both flat plate measurement locations. As can be seen, the turbulent shear stresses in the flat plate tend towards the wall shear stress value,  $\tau_w$ , as expected. The present results agree very well with the cross-wire results of Dotter. The difference between the two results are well within the expected experimental scatter.

In addition, the present data also agrees, at least qualitatively, with the results of other researchers. The flat plate LDV results of the other researchers all exhibit a “roll off” in the turbulent shear stress measurements near the wall. This result is attributed to angular bias errors

in the LDV measurements [12], and stationary fringes in the probe volume [17]. As mentioned in Chapter 3, angular bias can lead to low estimates of  $\bar{u}'v'$ . Thus, the low fluctuating velocity cross-correlation causes low estimates in the turbulent shear stress. Because the optics were aligned to avoid the problems of angular bias, and a Bragg cell was used to generate moving fringes, the turbulent shear stress values for the present flat plate LDV measurements approach the predicted wall shear stress values.

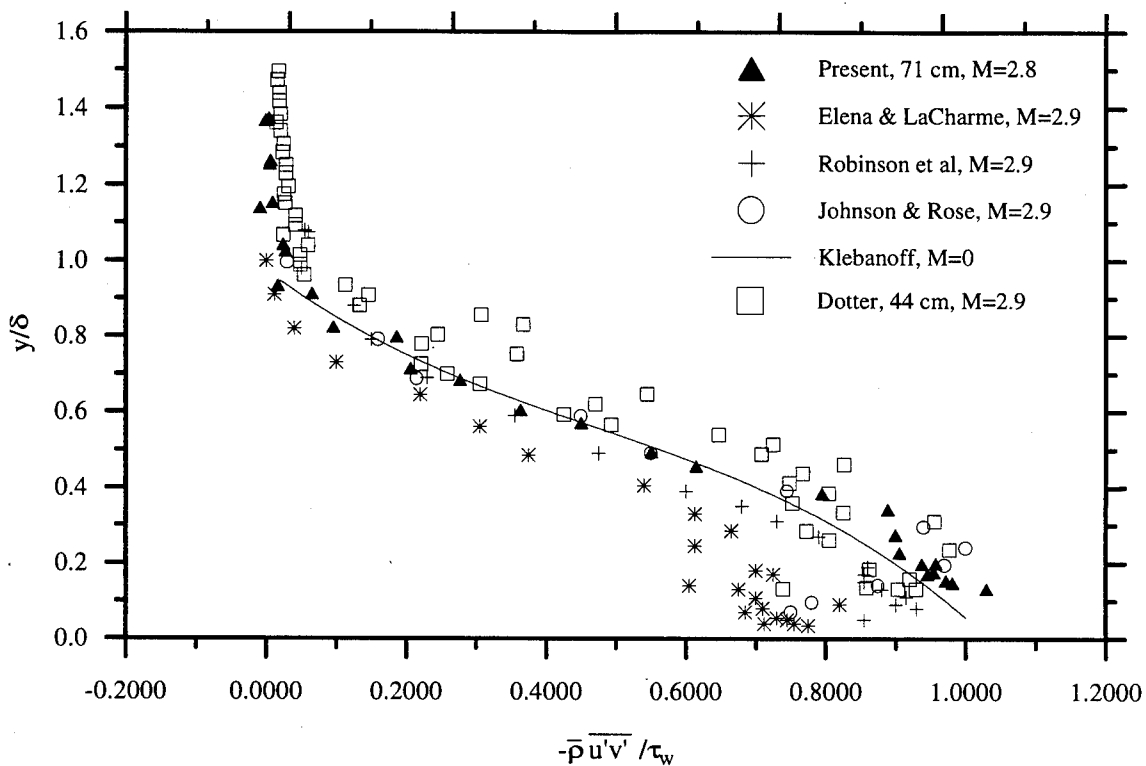


Figure 7-6: Flat Plate Turbulent Shear Stress

The intermittency function, which is a measure of the percentage of time that the boundary layer is turbulent (see Chapter 6), is presented in Figure 7-7. By generating a curve fit, the constants used in the intermittency equation (Eq. 6.24), and thus the mean boundary layer position, about which the turbulence fluctuates, may be determined. For the flat plate case at  $x = 71$  cm, the standard deviation was  $0.2\delta$ , or 1.94 mm about the mean location of  $y/\delta = 0.62$ .

Thus, the flow is intermittently turbulent at 62% of the boundary layer thickness. The results from the present study resemble those of Elena and LaCharme [12] quite well. The scatter in the present data above  $y/\delta = 1.0$  may be attributed to the freestream tunnel turbulence. Near the wall, the flatness,  $F_{l_u}$ , increased due to the wide range of measured velocities.

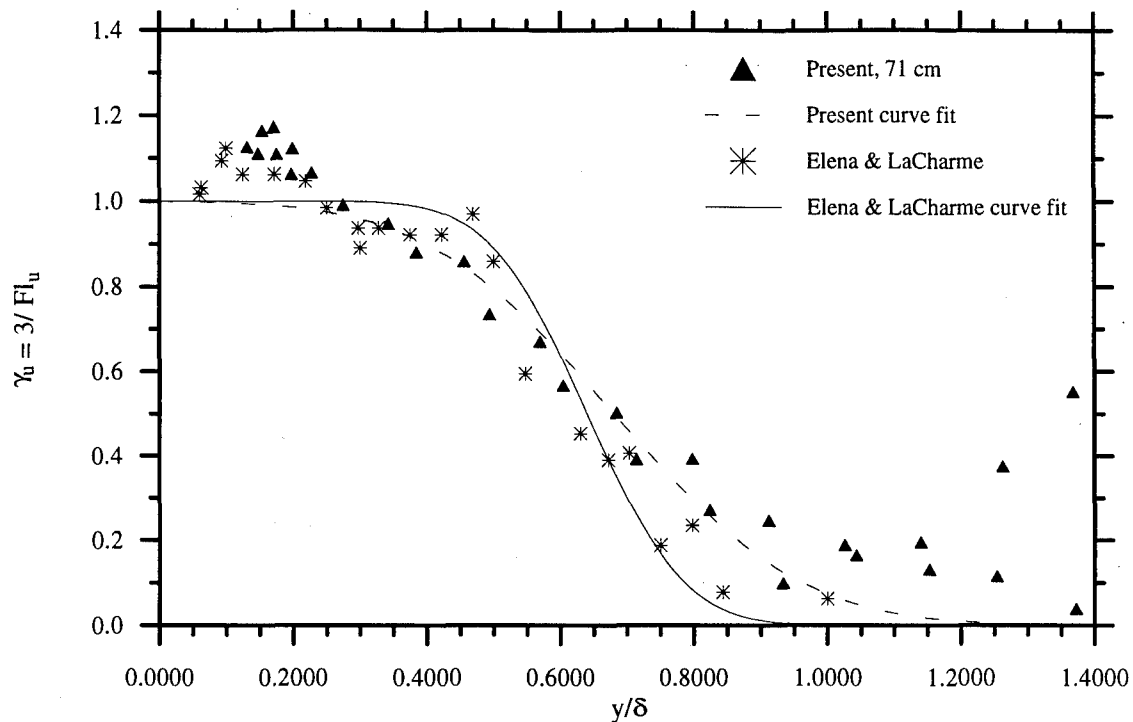


Figure 7-7: Flat Plate Intermittency Function

In summary, this section demonstrates that the LDV technique used in the present study was providing consistent and accurate results. The Mach number profile, turbulence intensities, turbulent shear stress, and intermittency function measured by the present LDV study match other accepted data quite well. The problems associated with angular bias were avoided by the optical arrangement used in the present study. Table 7-2 summarizes the computed flat plate boundary layer, displacement, and momentum thicknesses. With the flat plate comparisons

shown, the next section discusses the effects of the pressure gradient on the turbulent boundary layer. These pressure gradient results were compared to the flat plate results.

Table 7-2: Flat Plate Boundary Layer Thickness

Location	$\delta_u$ (mm)	$\delta_M$ (mm)	$\delta^*$ (mm)	$\Theta$ (mm)	$\delta_i^*$ (mm)	$\Theta_i$ (mm)
$x = 44$ cm	5.74	8.20	0.80	0.920	0.352	0.369
$x = 71$ cm	9.86	10.82	1.31	1.27	0.500	0.615

## 7.2 Pressure Gradient Results

Laser Doppler Velocimetry measurements were made at two locations on the compression ramp model, 71 cm and 68 cm. The first location was chosen so as to provide comparison to Dotter's results at the same location. By observing the surface pressure distribution along the compression ramp model, it was determined that even though the  $x = 71$  cm location was on the upstream side of a compression ramp, it was actually in a region of favorable pressure gradient (FPG). Thus, to enable evaluation of adverse pressure gradient effects, that were not combined with the favorable pressure gradient region, LDV measurements were made 3 cm upstream at the 68 cm location. Both sets of results were also compared to the flat plate LDV results obtained at 71 cm.

### 7.2.1 Flow Visualization

The shadowgraph and schlieren images of the compression ramp region are given in Figures (7-8) through (7-10). Due to the short duration of the flash (10 nanoseconds), the flow appears "frozen", and important qualitative features of the flow field can be observed from these pictures. The flow is from left to right in each photograph. Coalescing compression waves can be seen in the flow over the compression ramp. These waves have coalesced into a shock wave outside of the boundary layer. The weak shock waves at the front of the test section were produced by slight misalignments in the floors of the test section. In the schlieren photographs,

the turbulent eddies of the attached boundary layer can clearly be seen, as well as the non-uniform edge of the turbulent boundary layer. The thickness of the boundary layer decreases in the streamwise direction. From the shadowgraph, the boundary layer thickness at  $x = 68$  and  $71$  cm were estimated as  $7.52$  mm and  $8.67$  mm, respectively. In the schlieren photographs, these same thicknesses were estimated at  $7.37$  mm and  $9.22$  mm, respectively. Referring to Figure 7-10, there appear to have been present very organized turbulent structures, which were aligned at an angle of roughly  $40$ - $60^\circ$  relative to the wall.

### 7.2.2 Wall Pressure Distribution and Temperature

Pressure measurements were made along the compression ramp model centerline. These results, presented in Figure 7-11, show the increase in surface pressure from the constant flat plate value. The locations where LDV measurements were made are indicated by the dashed lines. The surface pressure begins to increase approximately  $3$  cm from the front of the model. Figure 7-11 depicts the favorable pressure gradient (FPG) in the vicinity of  $x = 71$  cm. At this location,  $dp/dx < 0$ , and the flow is expanding around the top of the model. The wall pressure gradient,  $dp_w/dx$ , at  $x = 68$  cm was estimated to be  $1250$  Pa/cm. A numerical analysis of the present study [14] indicated that  $dp_w/dx \approx dp_e/dx$  for the present flow field. These values were used in the estimation of Clauser's equilibrium parameter,  $\beta$ , listed in Table 7-1.

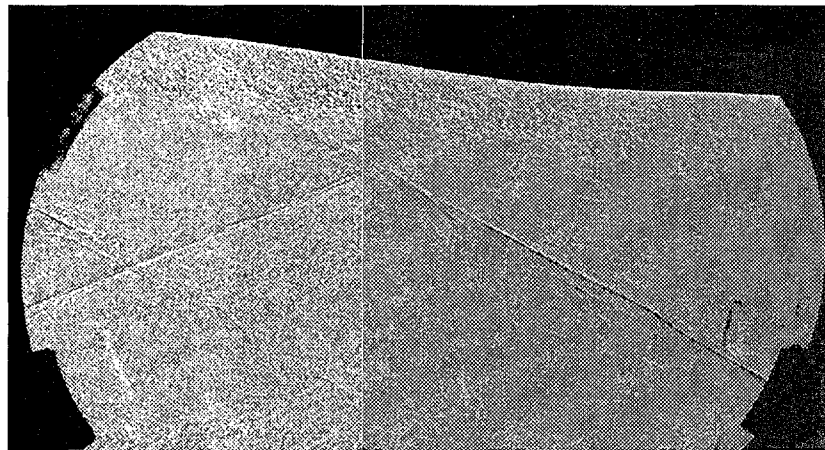


Figure 7–8: Shadowgraph of APG Region

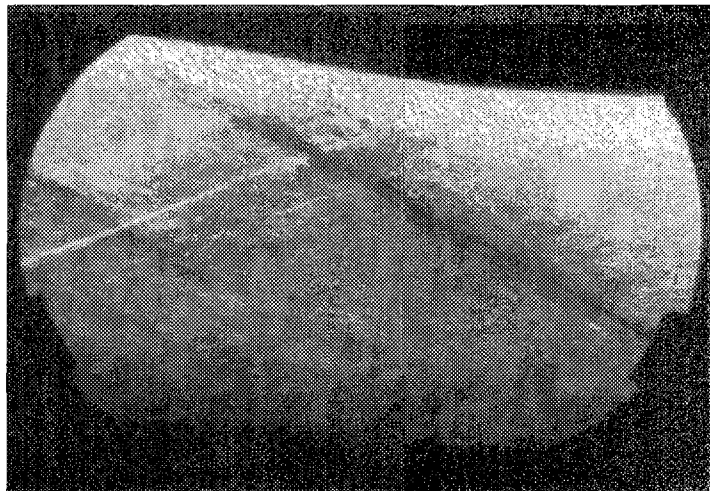


Figure 7–9: Horizontal Knife Edge Schlieren Photograph

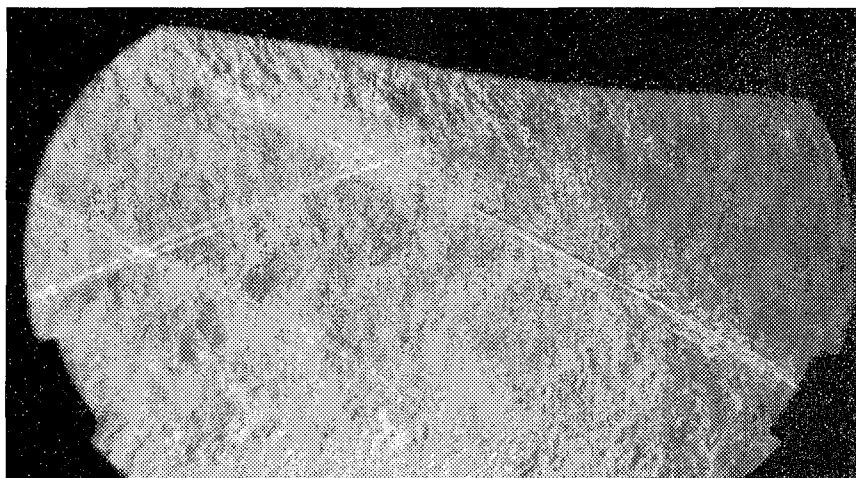


Figure 7–10: Vertical Knife Edge Schlieren Photograph

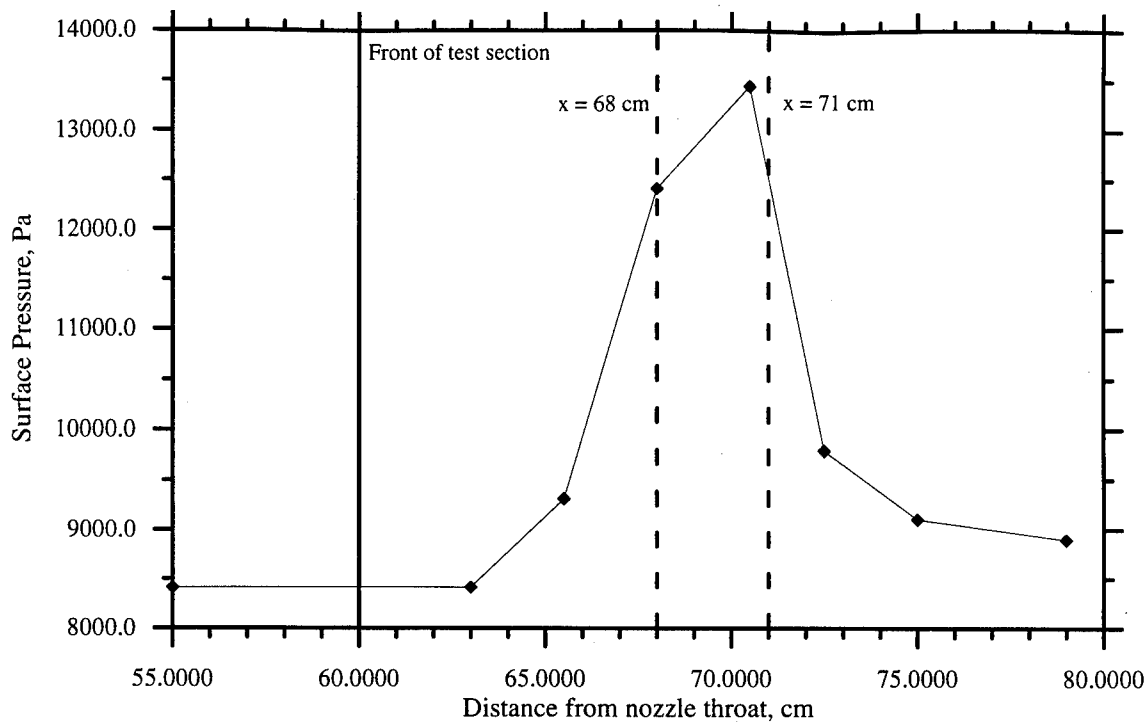


Figure 7-11: Compression Ramp Surface Pressure Distribution

The wall temperature measured 295 K. By using Eq. (6.7) and the freestream reference temperature,  $T_{o,\infty}$ , of 298 K, the adiabatic wall temperature,  $T_{aw}$ , was estimated as 278 K. Even though the calculated adiabatic wall temperature was approximately 6% below the measured wall temperature, the assumption of an adiabatic wall was used in this analysis.

### 7.2.3 Pressure Gradient vs. Flat Plate Mean Flow Results

The mean flow results of the LDV measurements at both  $x = 44$  and  $x = 71$  cm are presented in Figures 7-12 through 7-16. Recall, the main objective is to determine the effects of an adverse pressure gradient on supersonic turbulent boundary layers. To enable these pressure gradient effects to be distinguished from the effects due to the natural evolution of the flat plate boundary layer, both flat plate and pressure gradient results are presented together.

The LDV measurements are compared with the conventional and hot-wire anemometry results of Dotter [9], for both the adverse and favorable pressure gradient regions. Even though Dotter's measurements were made in the FPG region, they are still annotated as APG. Since Dotter used the Mach number boundary layer thickness to scale his results, a scale factor, equal to the ratio of the Mach- and velocity-based boundary layer thicknesses, was used to correlate the data by multiplying it by Dotter's tabulated  $y/\delta$  values. At the 71 cm station, this ratio was 1.30. In all cases, the LDV mean flow results closely resemble those obtained in the previous experiment.

The velocity profiles are presented in Figures 7-12 and 7-13. These figures show the progression of the velocity profiles as moved further down the tunnel. Over the compression ramp, the edge velocity decreases from 600  $m/s$  to about 575  $m/s$  in a distance of 3 cm. Meanwhile, the velocity profiles at 68 cm and 71 cm, for the APG and flat plate cases, respectively, are almost identical. In the latter figure, the velocity has been non-dimensionalized by the boundary layer edge velocity. As expected, all of the profiles collapsed rather well. Dotter's data at both measurement locations seems to bound the LDV results.

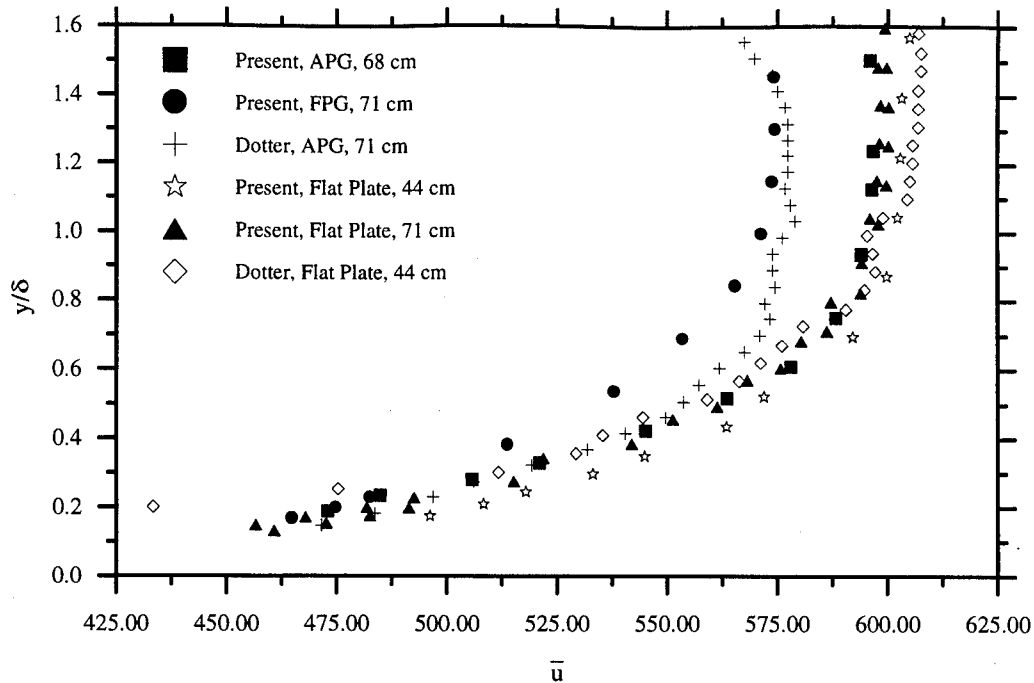


Figure 7-12: Pressure Gradient vs. Flat Plate  $\bar{u}$  Velocity

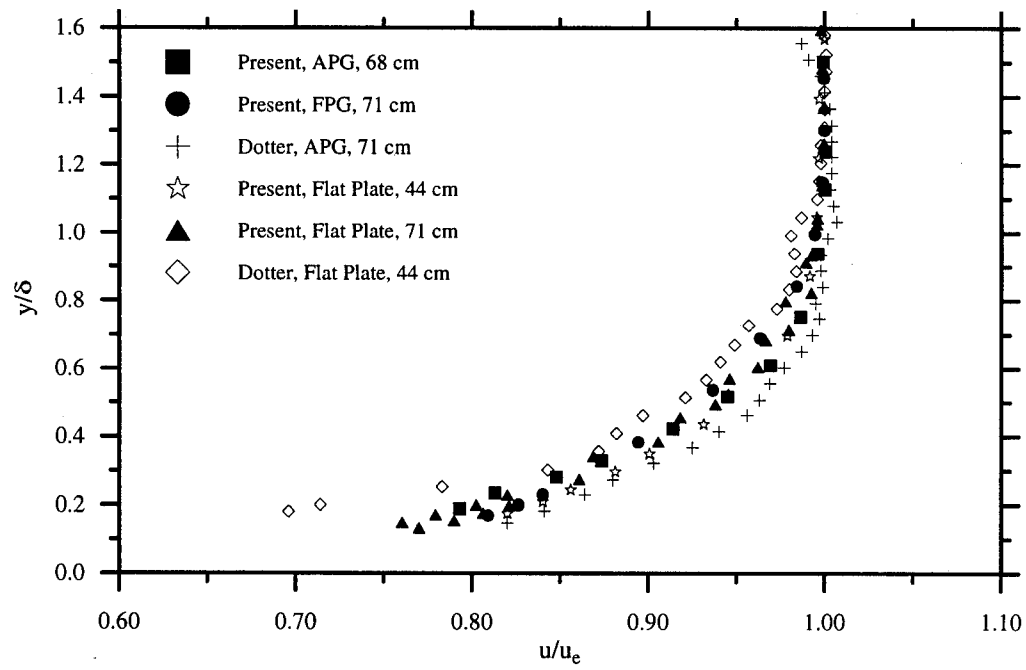


Figure 7-13: Pressure Gradient vs. Flat Plate  $u/u_e$  Profile

The flat plate and pressure gradient density profiles are presented in Figure 7-14. This figure demonstrates the excellent agreement between the LDV and conventional pressure-probe results of Dotter. The compression ramp increased the density at the boundary layer edge. This trend is evident as the profiles decrease in magnitude as the distance down the tunnel is increased. The greatest variation in profile shape occurred at  $x = 68$  cm, where the maximum value is at  $y/\delta = 0.6$ , instead of at the boundary layer edge.

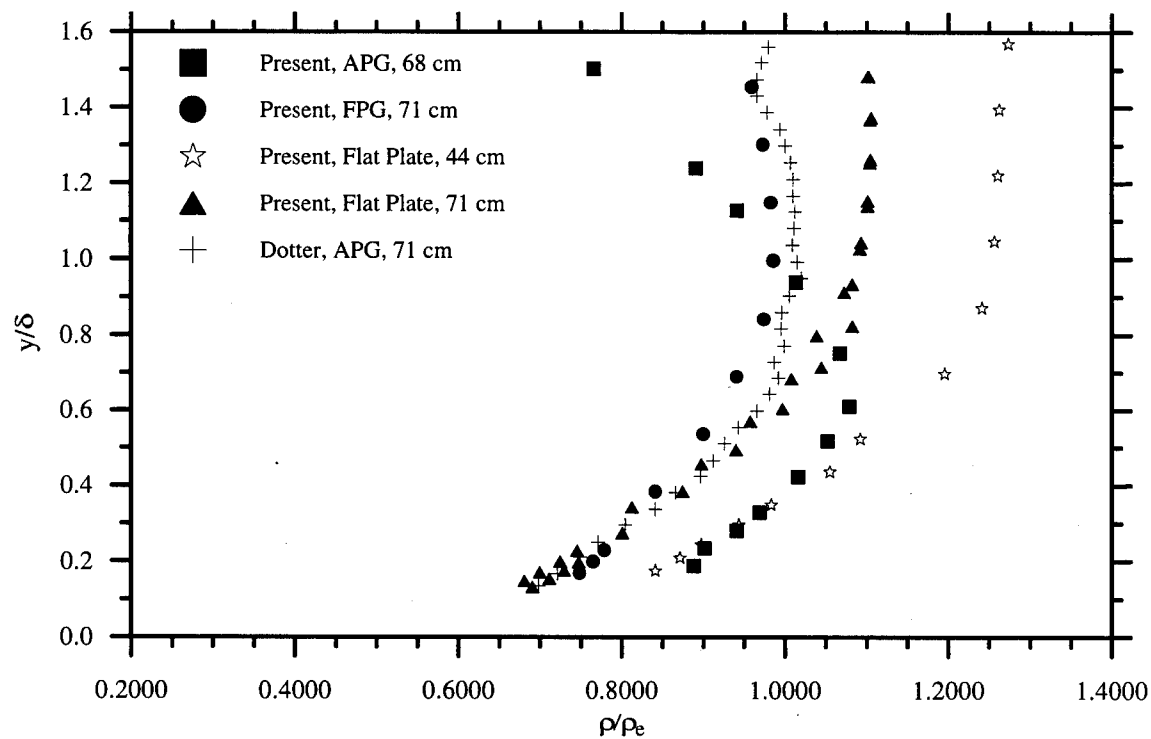


Figure 7-14: Pressure Gradient vs. Flat Plate Density

As with the streamwise velocity comparison above, which displays the Mach number profiles for both the flat plate and APG test sections at each measurement location, Figure 7-15 shows the progression of the boundary layer. The present results and Dotter's results compare

quite well; with the Mach number profiles at  $x = 44$  cm exhibiting remarkable agreement. The flow slows from Mach 2.9 upstream to Mach 2.5 at 71 cm in the compression ramp region. Between the measurement stations at  $x = 68$  and 71 cm, the flow slows from Mach 2.72 to Mach 2.51.

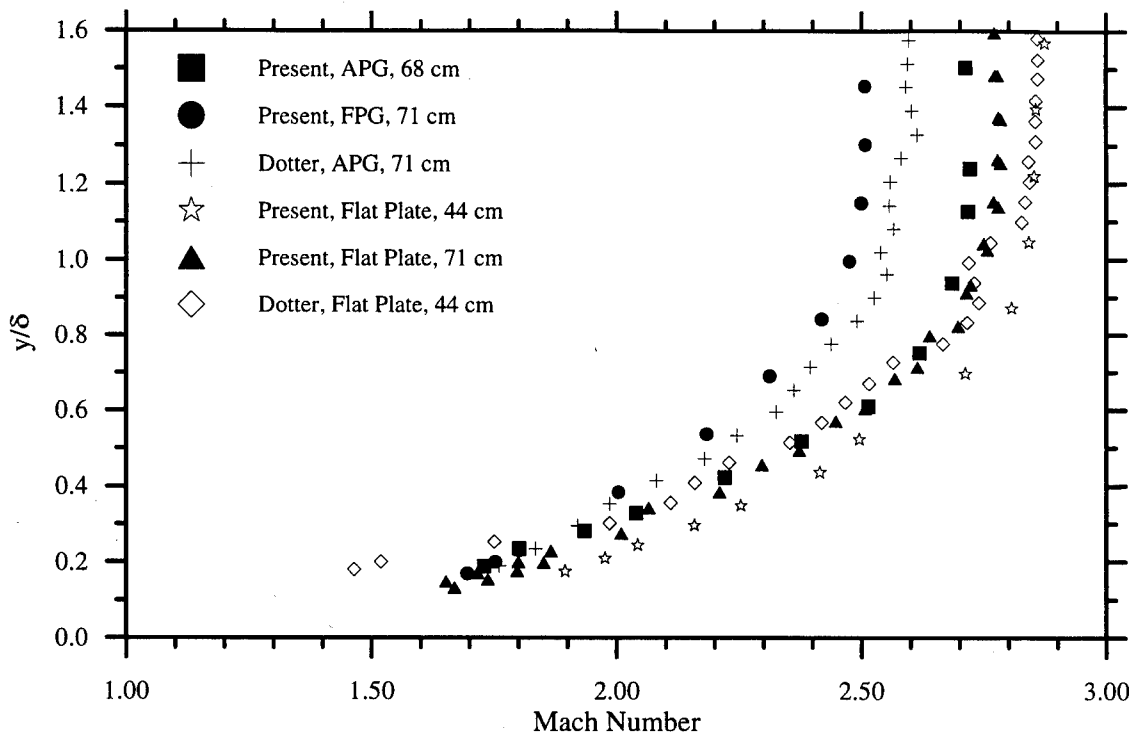


Figure 7-15: Pressure Gradient vs. Flat Plate Mach Number

The van Driest velocity transformation helps to correlate compressible flow data. These results were calculated and are presented in Figure 7-16. The dashed line represents the laminar sublayer, where  $u_{eff}/u^* = y^+$ . The equation of the solid line is given as

$$\frac{u_{eff}}{u^*} = 2.5 \ln(y^+) + 4.9 + 5.12 \sin^2\left(\frac{\pi}{2} \frac{y}{\delta}\right) \quad (7.1)$$

The single component measurements were made closer to the wall than the regular two-component LDV measurements. With single component LDV, the closest station to the wall was  $y^+ \approx 45$ . Overall, the measured LDV velocity profile compared very well with the theoretical values predicted by van Driest. Note, the large uncertainty is due to the estimate of skin friction ( $\pm 10\%$ , Ref. [3]), and possible error in the wall shear stress estimation.

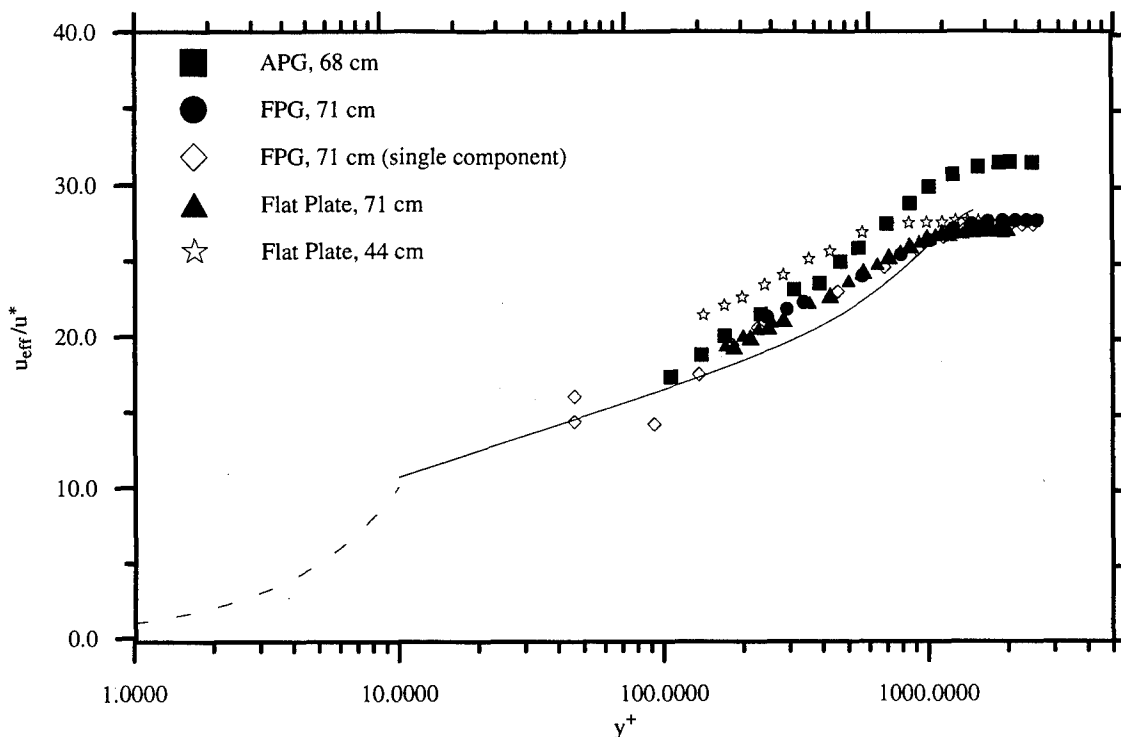


Figure 7-16: Van Driest Velocity Profile

As with the flat plate, the boundary layer, displacement, and momentum thicknesses were calculated in the adverse pressure gradient region. These results are presented in Table 7-3. When compared to the flat plate values, it is evident that the velocity and Mach boundary layer thicknesses decrease as a result of the adverse pressure gradient. Both boundary layer thicknesses at the  $x = 71$  cm station are smaller than those at the 68 cm location. This indicates that the streamlines are being compressed towards the wall, and the APG effects are still present

even in the FPG region at  $x = 71$  cm. These results agree well with the analysis of Sturek [30], who showed that even though the boundary layer thickness is decreasing, mass is being entrained in the boundary layer.

Table 7-3: Pressure Gradient Boundary Layer Thickness

Location	$\delta_u$ (mm)	$\delta_M$ (mm)	$\delta^*$ (mm)	$\Theta$ (mm)	$\delta_i^*$ (mm)	$\Theta_i$ (mm)
$x = 68$ cm	9.09	10.04	1.97	1.26	0.672	0.753
$x = 71$ cm	7.48	8.44	1.95	0.97	0.447	0.565

#### 7.2.4 Pressure Gradient vs. Flat Plate Turbulence Results

The remainder of this chapter presents the comparison of the flat plate and adverse pressure gradient turbulence terms. The turbulence intensities, Reynolds shear stresses, and intermittency function are presented, along with the higher-order moments, such as flatness and skewness. Lastly, the turbulent kinetic energy (TKE) and velocity-velocity correlation coefficient are examined. In all cases, the flat plate results at  $x = 71$  cm, and the results for the compression ramp measurement locations are given in the same figure for ease of comparison.

##### 7.2.4.1 Turbulence Intensities

The turbulence intensities, which give a measure of the magnitude of the fluctuating component, are presented in Figure 7-17 and Figure 7-18. The turbulence intensities (T.I.) for both the u- and v-component increased as a result of the pressure gradient, with the streamwise component exhibiting the largest increase. For the u-component, the maximum turbulence intensity at  $x = 68$  cm, located at  $y/\delta = 0.25$ , was 9.0%. Thus, the adverse pressure gradient caused the streamwise turbulence intensity to increase by 24% of its flat plate value, at the same location in the boundary layer. For the FPG location, the u-component turbulence intensity showed a 14% increase over the flat plate value. For the v-component, the T.I. at both 68 and 71

cm have a maximum value of 3.7% at  $y/\delta = 0.2$ , which results in an 8.1% increase over the corresponding flat plate value. Thus, the FPG effects have reduced the magnification of the turbulence intensities.

It should be noted that the results of the hot-wire analysis were very different. Above  $y/\delta \approx 0.5$ , the hot-wire and LDV u-component T.I. results match quite well. Below this location, the hot-wire results are lower than those of the present study. From Figure 7-18, it appears as if the hot-wire turbulence intensity exhibits the same general trend as the LDV results. Yet, the hot-wire results are magnified by as much as 163% of the LDV values. These trends seem to indicate that the turbulence transformation [9] used to extract the turbulence intensities from the hot-wire analysis may not be valid for flow fields involving pressure gradients.

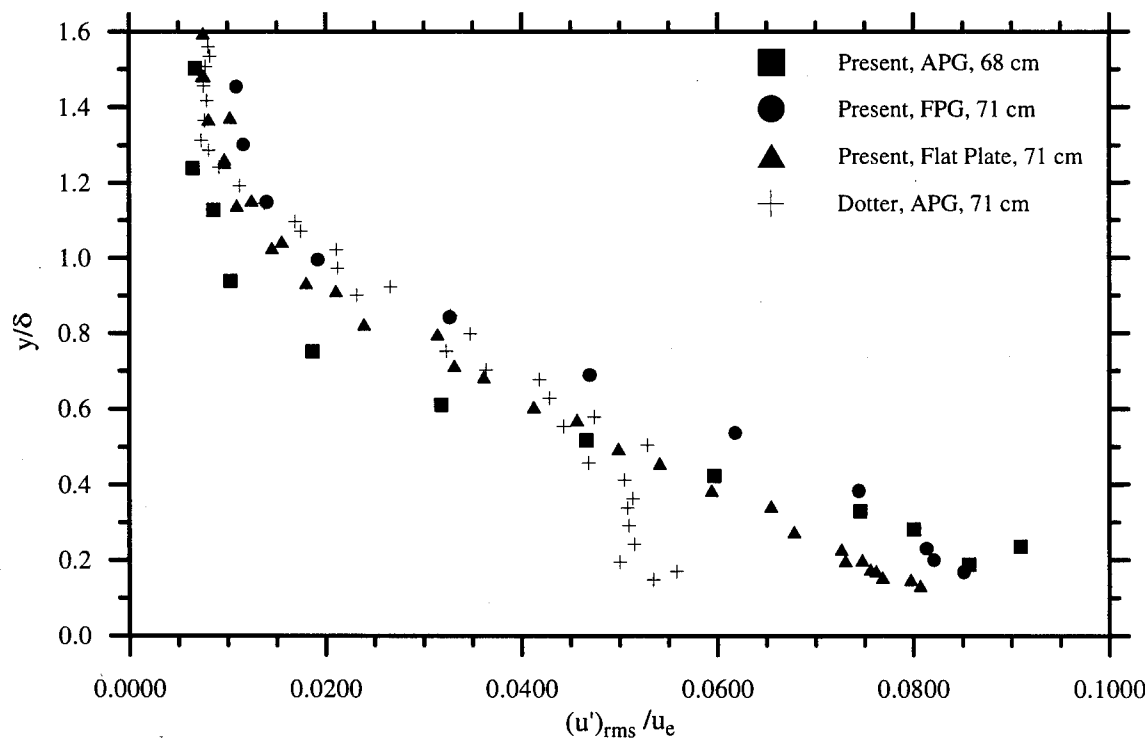


Figure 7-17: Pressure Gradient vs. Flat Plate u-component Turbulence Intensities

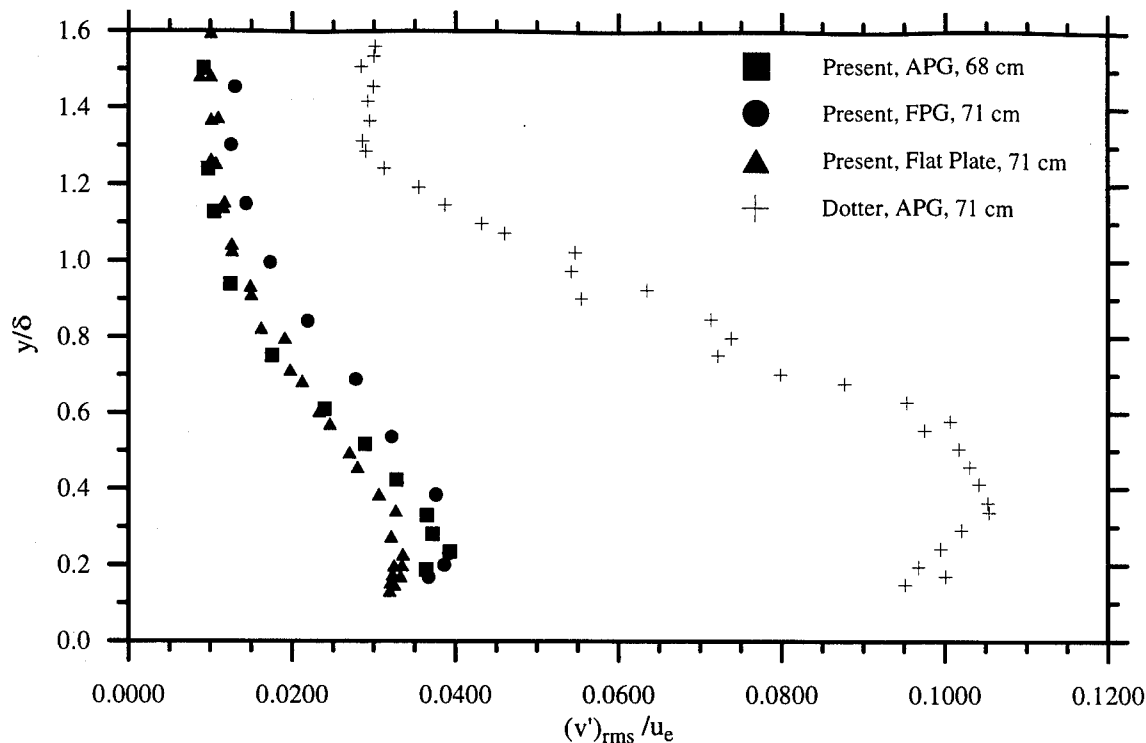


Figure 7-18: Pressure Gradient vs. Flat Plate v-component Turbulence Intensities

#### 7.2.4.2 Reynolds Shear Stresses

The Reynolds shear stresses, which were extremely sensitive to the pressure gradients, are presented in Figures 7-19 and 7-20. In the first figure, the Reynolds shear stress, calculated as the product of the mean density and fluctuating velocity cross correlation,  $\overline{u'v'}$ , at each traverse station, was non-dimensionalized by the flat plate wall shear stress,  $\tau_w$ . Therefore, the 71 cm flat plate results approach unity at the wall. At 71 cm, the Reynolds shear stress in the FPG region increases by 67% of the flat plate value. The 68 cm APG Reynolds shear stress reaches a maximum value of 2.6 at  $y/\delta = 0.25$ , which is an 190% increase over the flat plate value of 0.9 at the same location in the boundary layer. These results agree with Ref. [22] which

showed the turbulent shear stresses had maximum values over the wall shear stress near  $y/\delta \approx 0.3$ .

In Figure 7-20, the Reynolds shear stresses are non-dimensionalized by the mean velocity,  $\bar{u}$ . The 71 cm APG profile seems to exhibit an inflection point near  $y/\delta = 0.7$ , which may be attributed to experimental scatter. The profiles for the flat plate and 68 cm APG case have the same slope, with the APG Reynolds shear stress increased to 133% of the flat plate value at  $y/\delta = 0.2$ . As expected, the Reynolds shear stresses approach zero for locations  $y/\delta > 1.0$ .

As with the hot-wire turbulence intensities, the turbulent shear stresses differ greatly from the LDV results. Because the LDV technique directly measures the mean, fluctuating, and cross-correlation velocity components, which are used in the estimates of the turbulence intensities, and the Reynolds shear stresses, these values are assumed correct. No assumptions or transformations were required to extract these terms as with the hot-wire analysis. These variations indicate that the assumptions used in the hot-wire turbulence transformation may not be valid for pressure gradient supersonic flow.

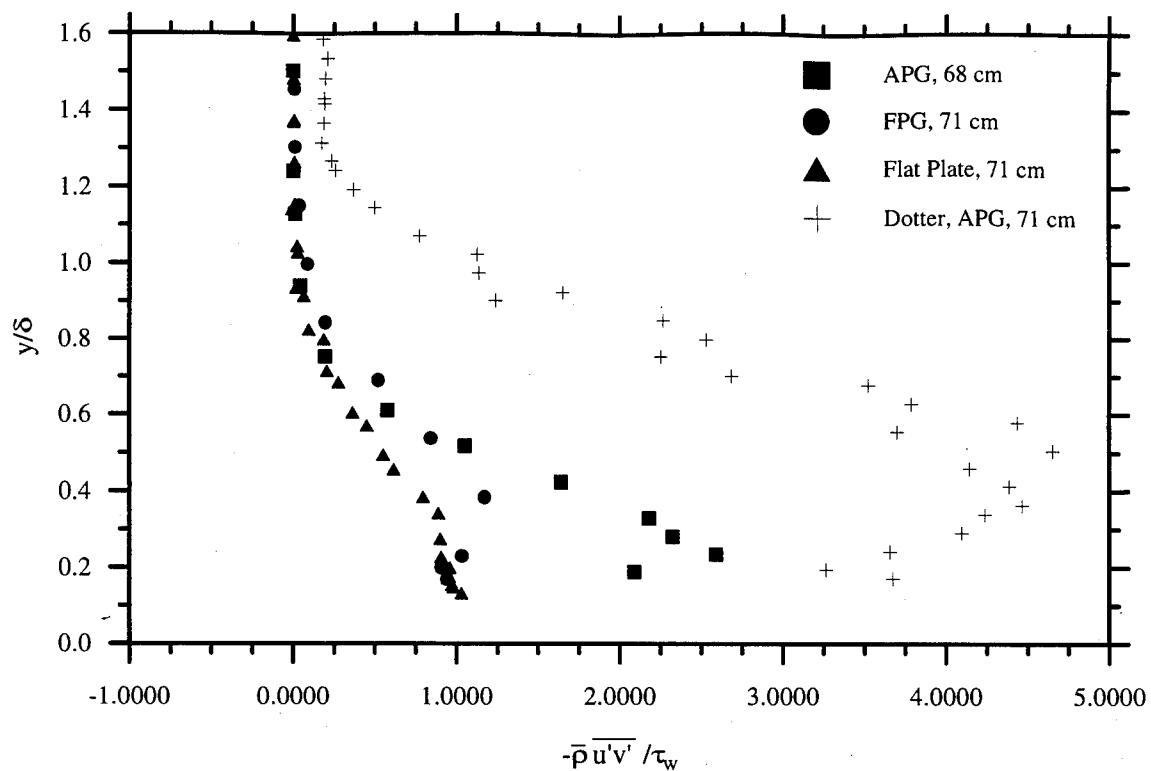


Figure 7-19: Reynolds Shear Stress

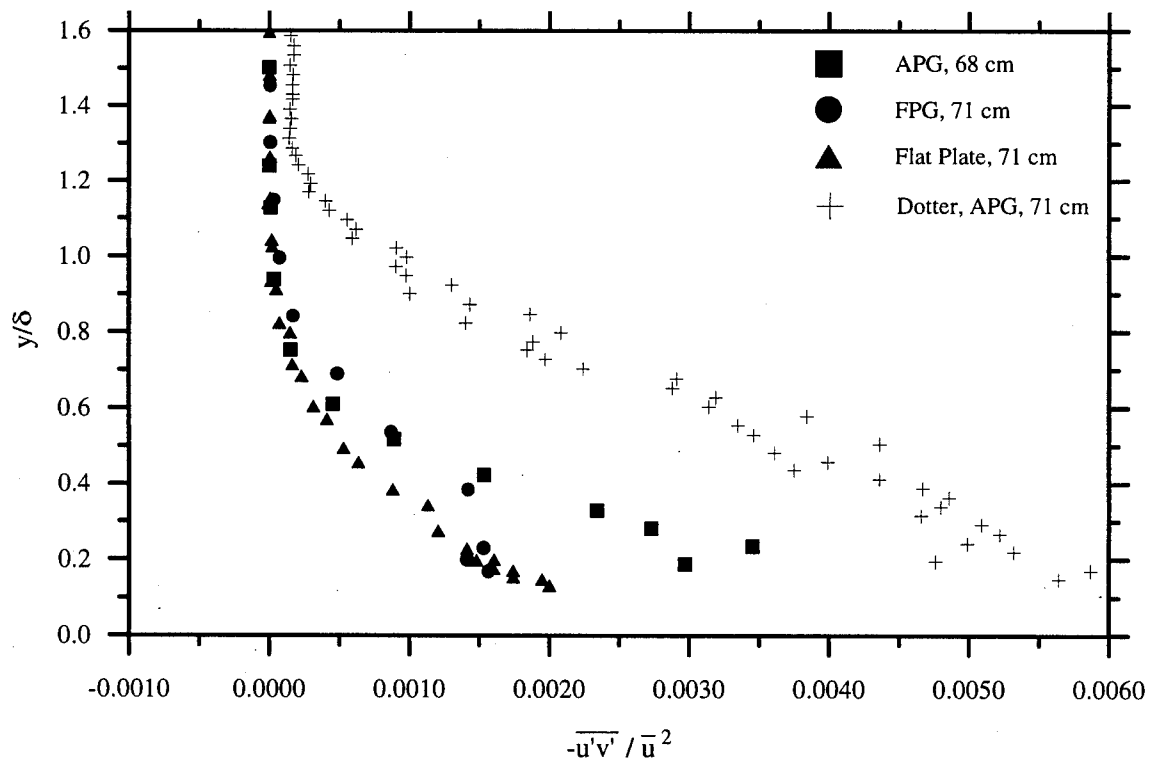


Figure 7-20: Reynolds Shear Stress

### 7.2.4.3 Skin Friction Estimates

In the logarithmic or overlap region of the boundary layer,  $\tau_w \approx \tau_{xy}^T + \frac{dp}{dx} y$ . The results in Figure 7-16 suggest that the near wall measurements were in the log region (i.e.  $y^+ < 300$ ). The wall shear stress,  $\tau_w$ , may be estimated by assuming

$$\tau_w \approx -\rho_w \overline{u'v'} \quad (7.2)$$

Hence, the skin friction coefficient,  $C_f$ , may be accurately estimated as

$$C_f = \frac{2\tau_w}{\rho_e u_e^2} \approx \frac{-2\rho_w \overline{u'v'}}{\rho_e u_e^2} \quad (7.3)$$

Table 7-4 summarizes the results of this skin friction analysis. The adverse pressure gradient doubles the skin friction at the same location. Interestingly, the skin friction of the flat plate and the FPG region are almost the same. The skin friction, then, is reduced by 50% between the  $x = 68$  cm and 71 cm compression ramp locations. The van Driest estimate predicted skin friction values larger than the current estimates. This may be a result of overpredicting the wall shear stress by the methods described in Chapter 6. These results agree well with those of Smith [27] and Spina [28].

Table 7-4: Skin Friction Estimates

Location	Flat Plate, $x = 71$ cm	APG, $x = 68$ cm	FPG, $x = 71$ cm
$C_f$ , current estimate	0.0011	0.0022	0.0010
$C_f$ , van Driest	0.0016	0.0016	0.0016

### 7.2.4.4 Intermittency Function

The intermittency function at both 68 cm and 71 cm is presented in Figure 7-21. Recall, this is a measure of the time that the boundary layer edge is turbulent. Curve fits have been

generated to determine the constants from Eq. (6.24), which give the standard deviation about the mean boundary layer position. For the 68 cm case, the standard deviation was  $0.17\delta$ , or 1.54 mm, about the mean location of  $y/\delta = 0.55$ . For the 71 cm case, the standard deviation was  $0.26\delta$ , or 1.94 mm, about the mean location of  $y/\delta = 0.62$ . Thus, the mean turbulent boundary layer thickness is smaller in a region of greater adverse pressure gradient. When the 71 cm intermittency function is compared to the flat plate boundary layer at the same location, it is interesting to note that the standard deviation and mean location are identical. Also, the mean boundary layer location at the  $x = 68$  cm station is smaller than the flat plate mean location.

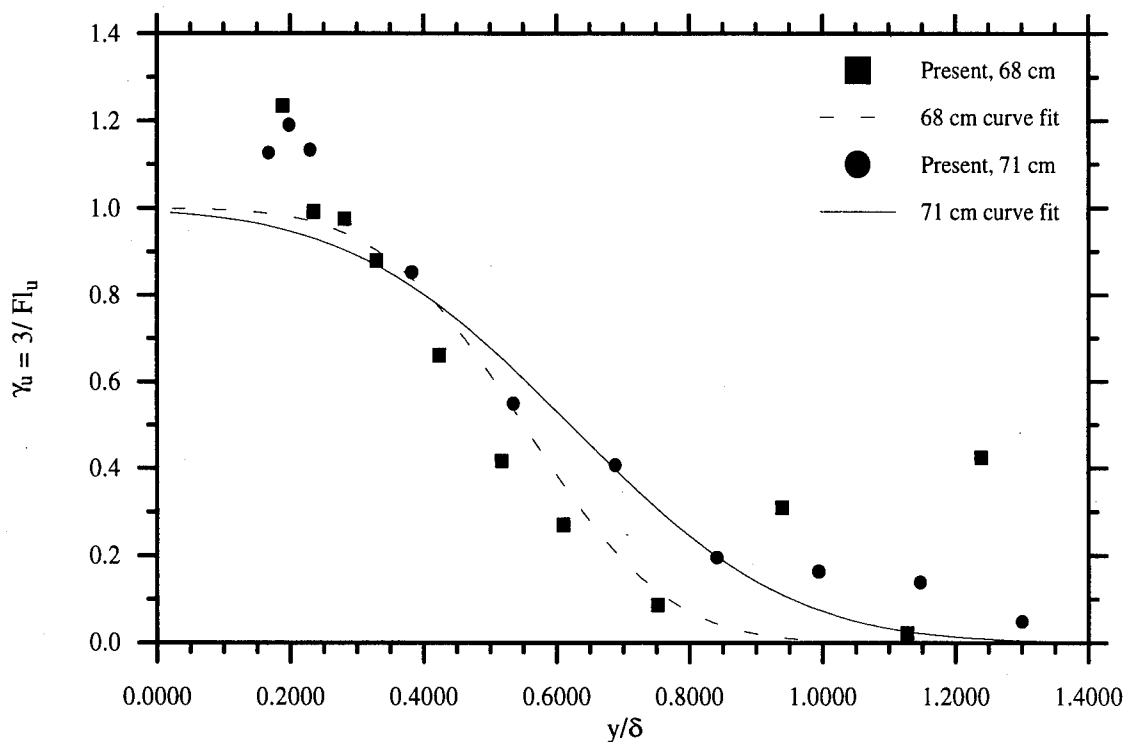


Figure 7-21: Pressure Gradient Intermittency Function

#### 7.2.4.5 Flatness and Skewness

These higher-order turbulent statistics are presented in Figures 7-22 through 7-25. In all cases, the present flat plate values match the Elena and LaCharme [12] flat plate data quite well. The flatness for both components over the flat plate tend to center around zero throughout the boundary layer. The flatness in both the u- and v-components is nearly zero to a location of  $y/\delta \approx 0.8$ . This indicates that the flat plate LDV flatness measurements are not susceptible to much variation. But, these values are magnified by the adverse pressure gradient model; especially at the 68 cm location, where the flatness begins to diverge from zero near  $y/\delta = 0.5$  for both components. The skewness, which helps to determine to which side of the mean the majority of the data lies, is negative for the u-component, yet positive for the v-component. In each case, within the boundary layer, these moments exhibit the trend of the flat plate values as one bound, the 68 cm, or greater adverse pressure gradient as the other bound, with the 71 cm APG case lying somewhere in the middle.

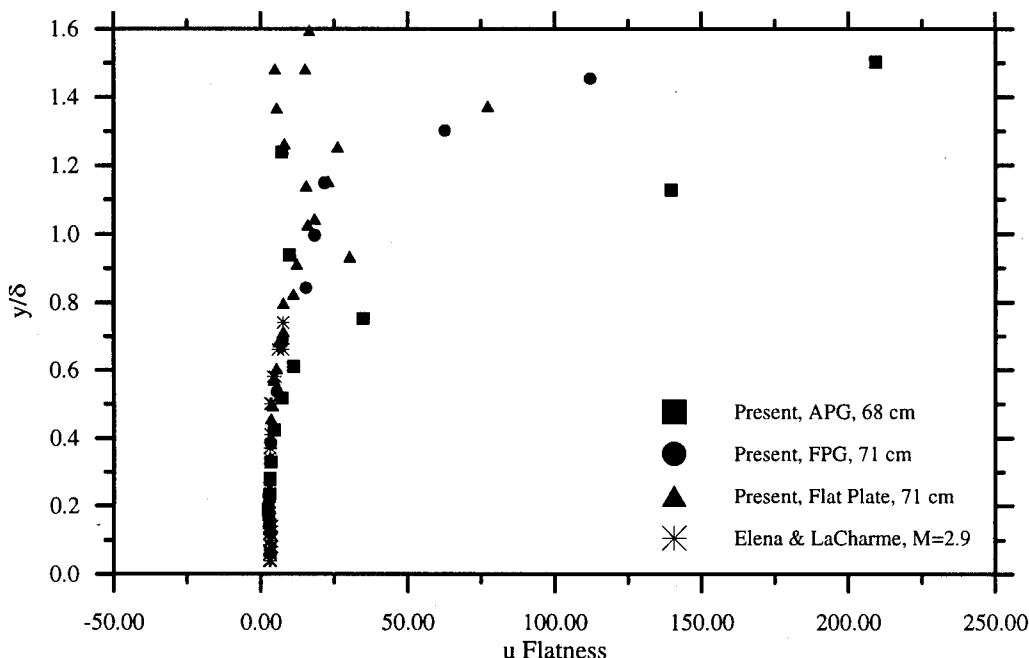


Figure 7-22: Pressure Gradient vs. Flat Plate u-component Flatness

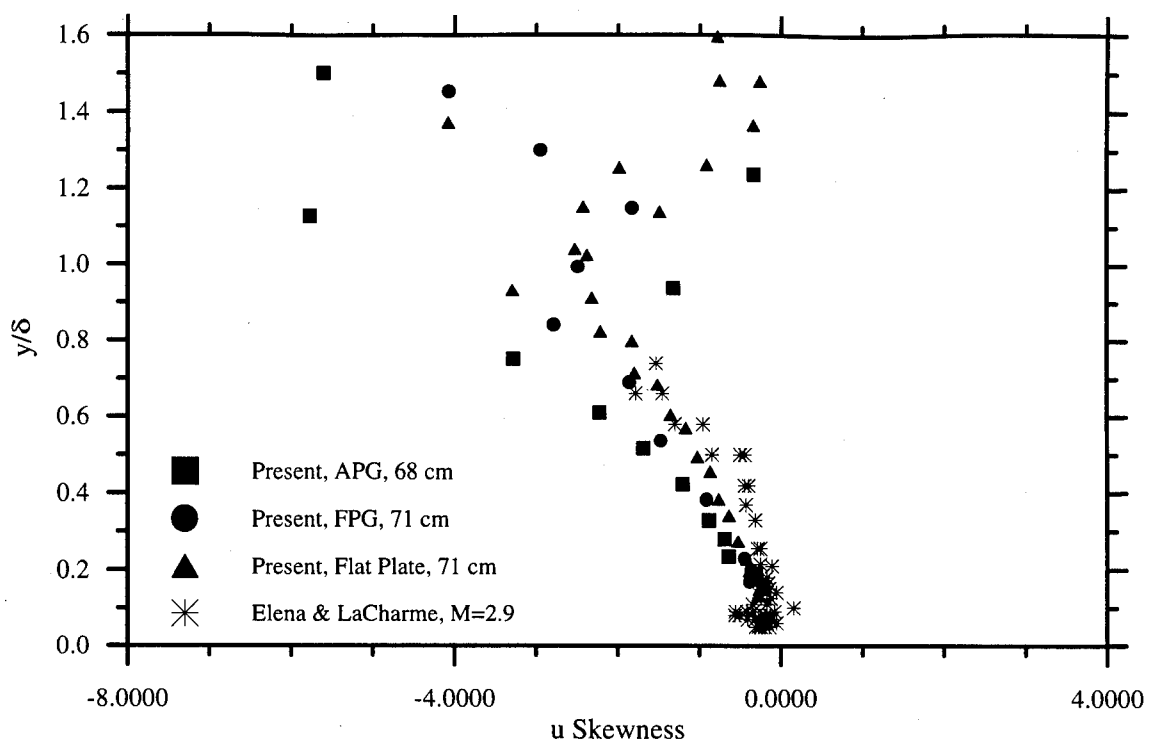


Figure 7-23: Pressure Gradient vs. Flat Plate  $u$ -component Skewness

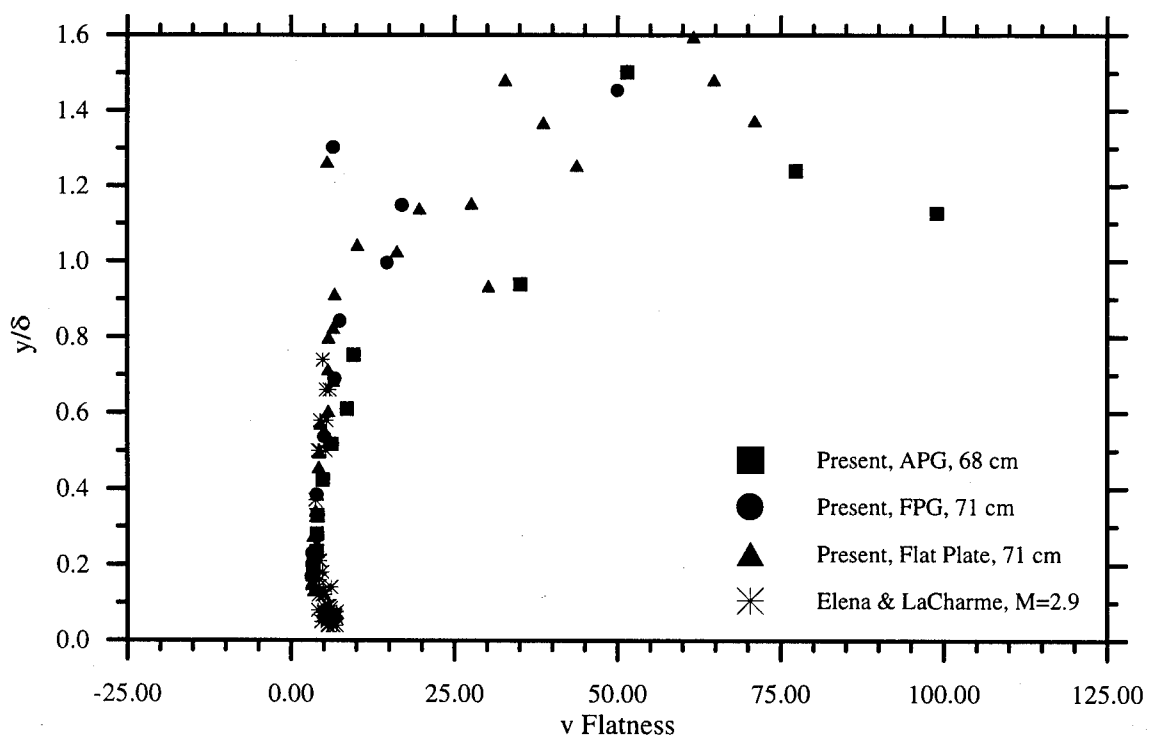


Figure 7-24: Pressure Gradient vs. Flat Plate  $v$ -component Flatness

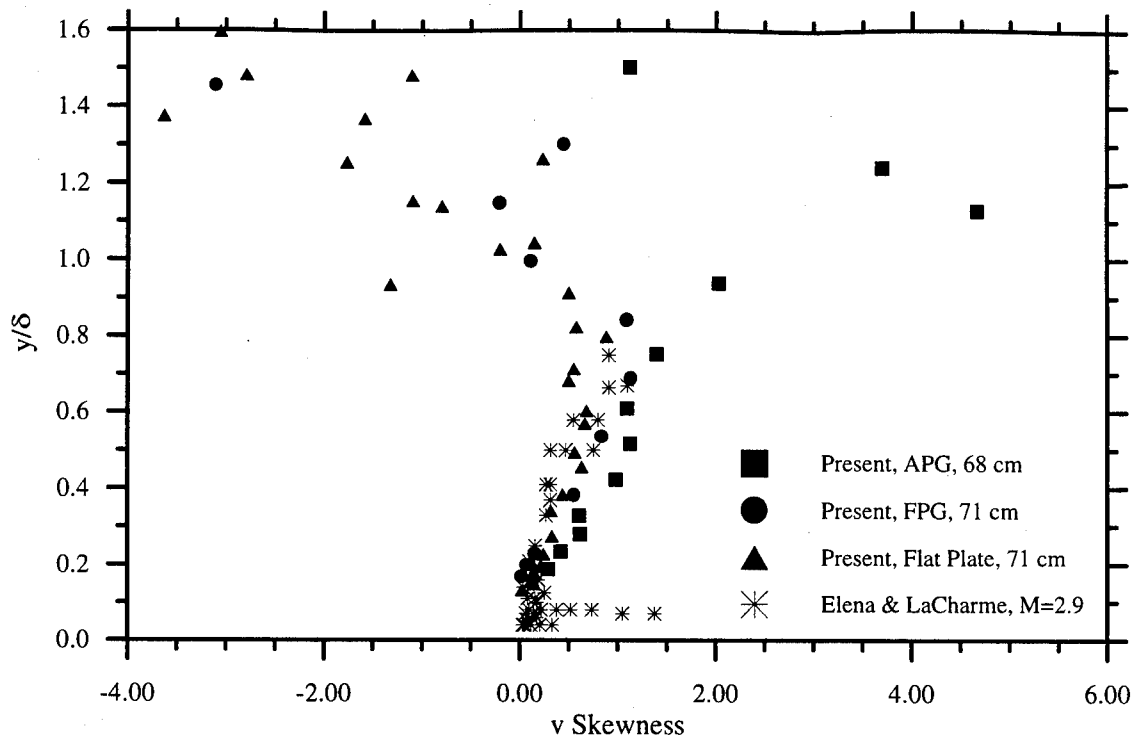


Figure 7-25: Pressure Gradient vs. Flat Plate  $v$ -component Skewness

#### 7.2.4.6 Velocity-Velocity Correlation Coefficient and TKE

These turbulent values are presented in Figures 7-26 and 7-27, respectively. Notice that the  $R_{uv}$  data of Elena and LaCharme scatters much more than their previous turbulent results. The velocity-velocity correlation coefficient results from the present study exhibit a more uniform trend. The coefficient is increased to 65% of the flat plate value at the location of  $y/\delta = 0.3$  for the  $x = 68$  cm station. Yet, for the location at 71 cm, the coefficient decreases by 27% of the flat plate value at  $y/\delta = 0.2$ . These results indicate that the present flow field exhibits incompressible behavior near the wall, as  $-R_{uv} \approx 0.4 - 0.5$  [3].

The TKE, which is a measure of the turbulent kinetic energy of the velocity fluctuations, shows increased values as the wall is approached. This is expected as the boundary layer is more turbulent in this region, than near the boundary layer edge. The flat plate and APG results show

the same trend in the slope at the  $x = 71$  cm location. But, the gradient near the wall at the 68 cm station seems to be larger. In each case, the TKE approach 0.015% as predicted by Eq. (6.29), and u- and v-component turbulence intensities of 1.0%. Recall, that the TKE has been calculated assuming the fluctuations in the w-direction, although not measured with the present LDV study, are of the same magnitude as the v-component fluctuations.

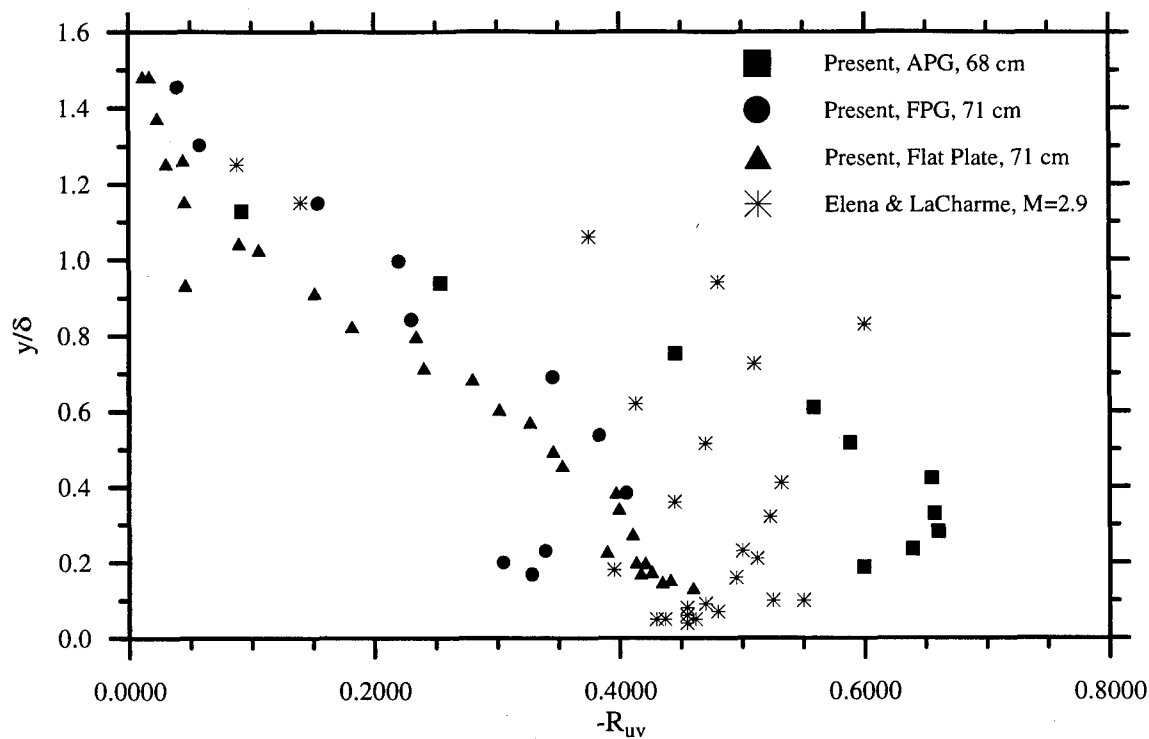


Figure 7-26: Velocity-Velocity Correlation Coefficient

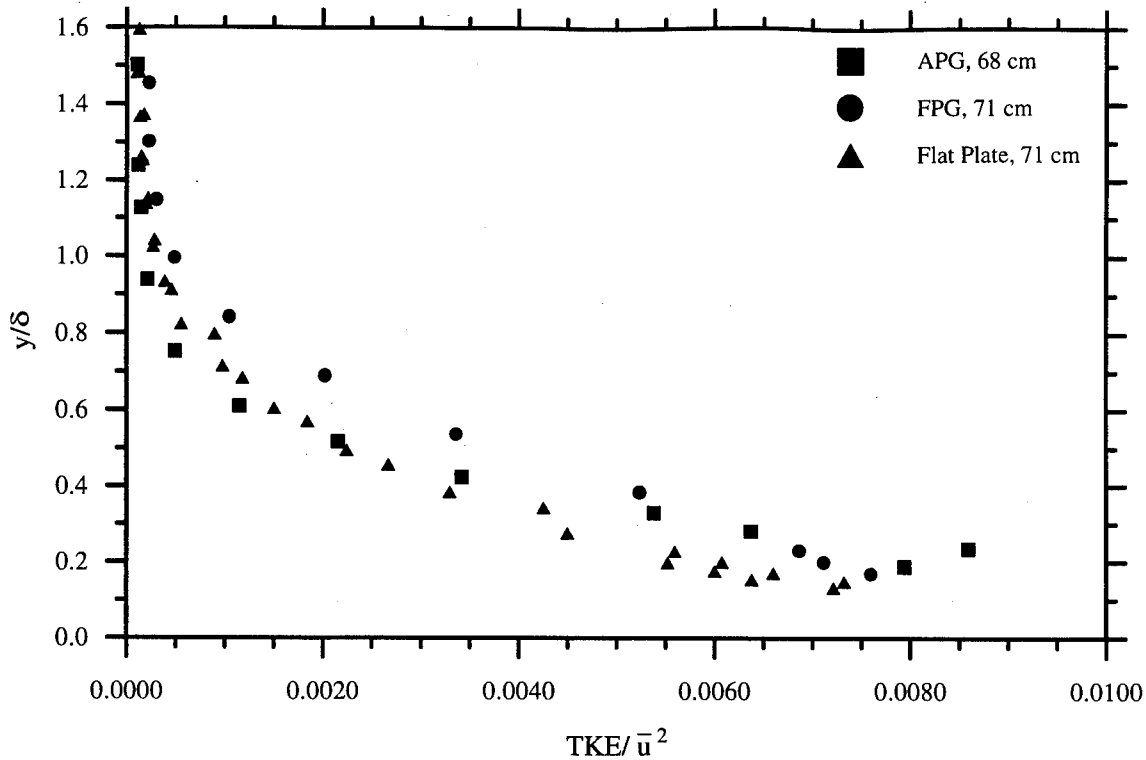


Figure 7-27: Pressure Gradient vs. Flat Plate TKE

#### 7.2.5 Pressure Gradient vs. Flat Plate Strain Rates

Strain rate measurements were made in the vicinity of the 71 cm location for both the compression ramp and flat plate models. Five measurement profiles were required for the pressure gradient station at 71 cm. With reference to the finite-difference grid in Figure 6-1, the distances  $dx_1$  and  $dx_2$  were 4.8 mm and 9.8 mm, respectively. The lateral measurements were made 5 mm on either side of the tunnel centerline. Strain rates were non-dimensionalized by the edge velocity and boundary layer thickness.

To determine the relative strength of these strain rates, the measurements were quantified after the analysis of Ref. [27]. The ratio of each extra strain rate,  $e$ , to the main strain rate in the boundary layer,  $du/dy$ , was calculated. The distortion is classified as weak if the ratio

$e/(du/dy) \approx 0.01$ , and strong if  $e/(du/dy) \approx 0.1$ . For the present study, these ratios revealed that the interactions were strong.

Figure 7-28 presents the rate of change of the u-component of velocity with change in distance down the tunnel. As expected, this flat plate strain rate was calculated as zero. At  $y/\delta = 0.1$ , the strain rate for the APG case has increased to 0.2. The largest gradient occurs below  $y/\delta = 0.5$ .

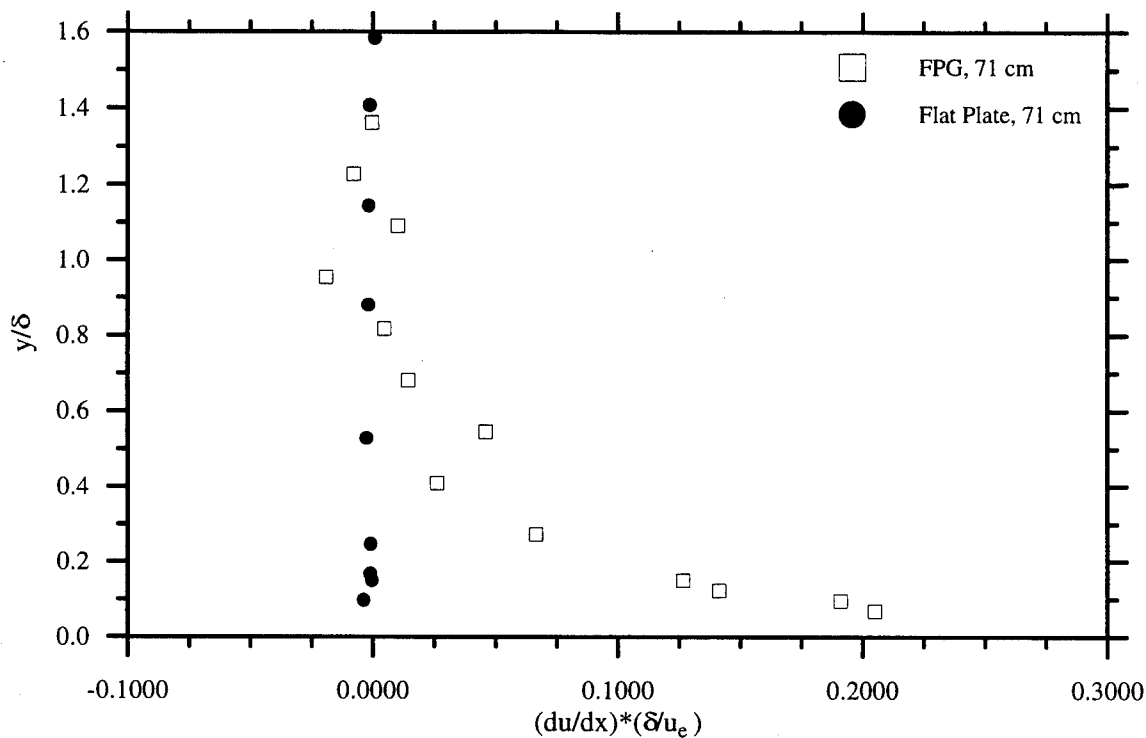


Figure 7-28:  $du/dx$  Strain Rate Comparison

The change in u-component over the boundary layer thickness is given in Figure 7-29. This figure indicates that this strain rate for the pressure gradient case is almost the same as the flat plate case. The quantity  $du/dy$  is used in determining gradient transport formulations such as the eddy viscosity model or Prandtl's mixing length model [3].

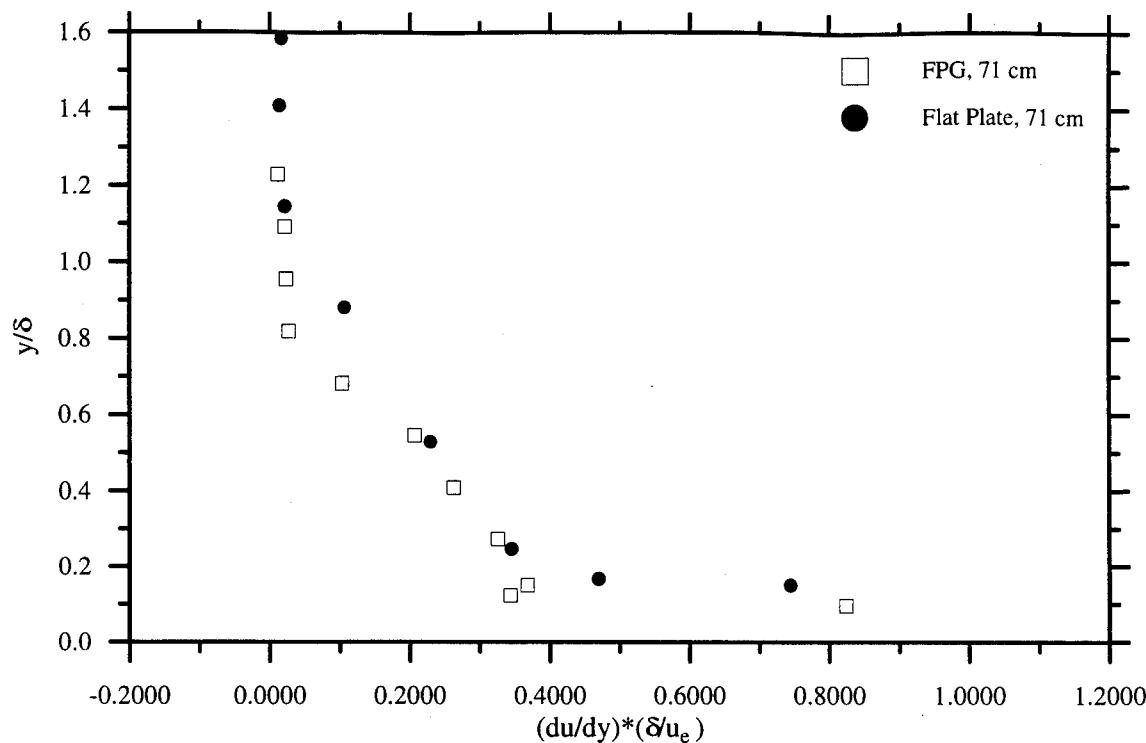


Figure 7-29:  $du/dy$  Strain Rate Comparison

Prandtl proposed that the turbulent fluctuations could be related to a length scale and velocity gradient. The Prandtl mixing length model is given by

$$\tau_{xy}^T \approx -\bar{\rho} l_m^2 \gamma \left| \frac{du}{dy} \right| \frac{du}{dy} \quad (7.4)$$

where  $l_m$  is the mixing length and  $\gamma$  is the intermittency function. The mixing length is constant for  $y/\delta \geq 0.22$  and is given by  $l_m = 0.09\delta$ . For locations below  $y/\delta = 0.22$ ,  $l_m = 0.4y$ .

Using the strain rates at 71 cm and the mean flow results, the turbulent shear stress  $\tau_{xy}^T$  was calculated. The results are presented in Figure 7-30. The Prandtl mixing model, which is primarily an incompressible turbulence model, grossly underpredicts the turbulent shear stress

calculated in the present experiment. This demonstrates the need for valid data so that accurate compressible turbulence models may be developed.

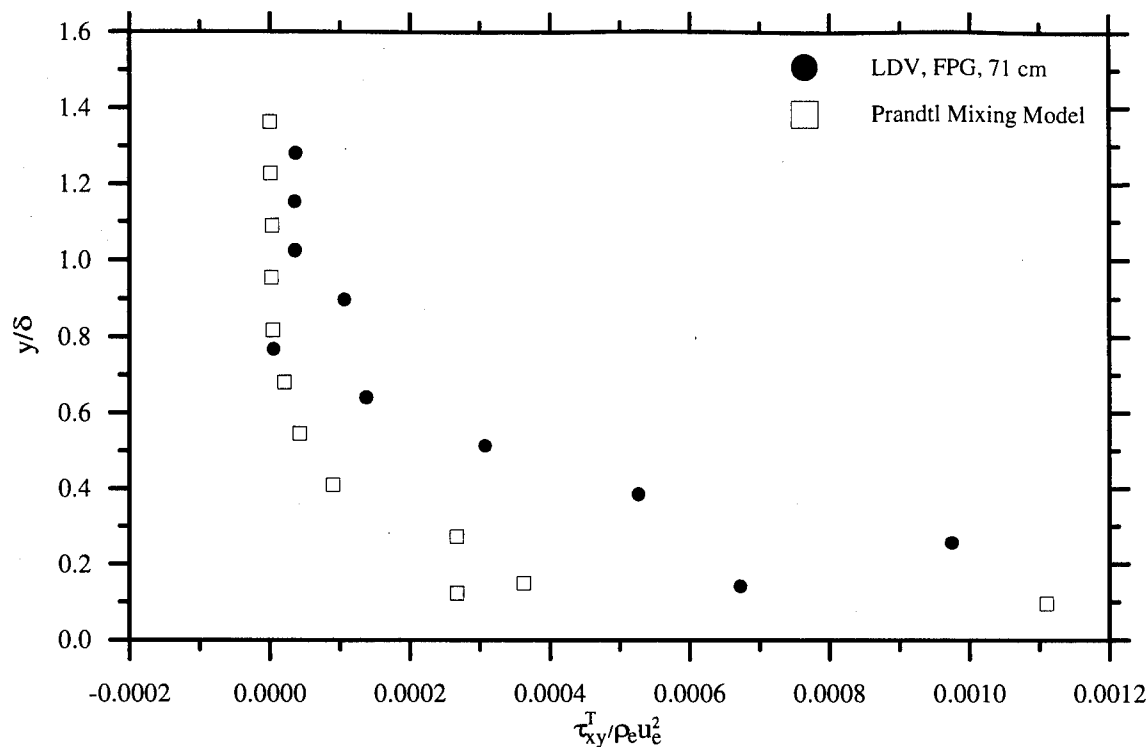
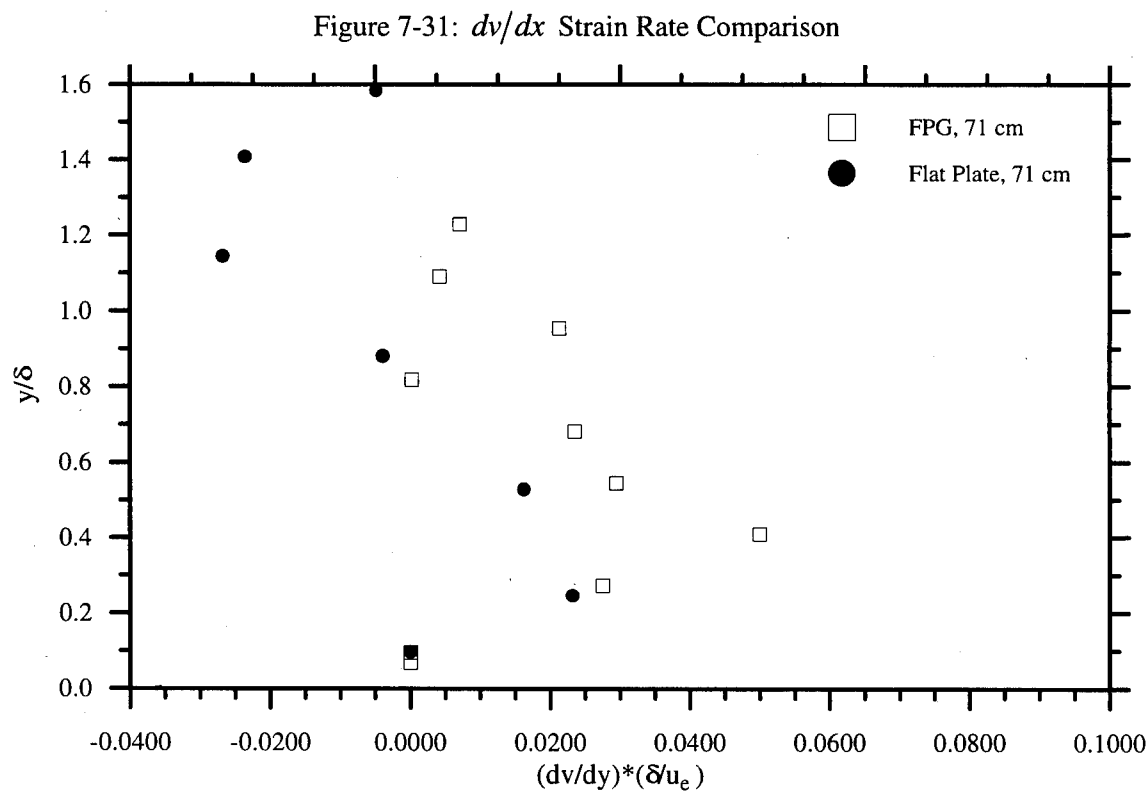
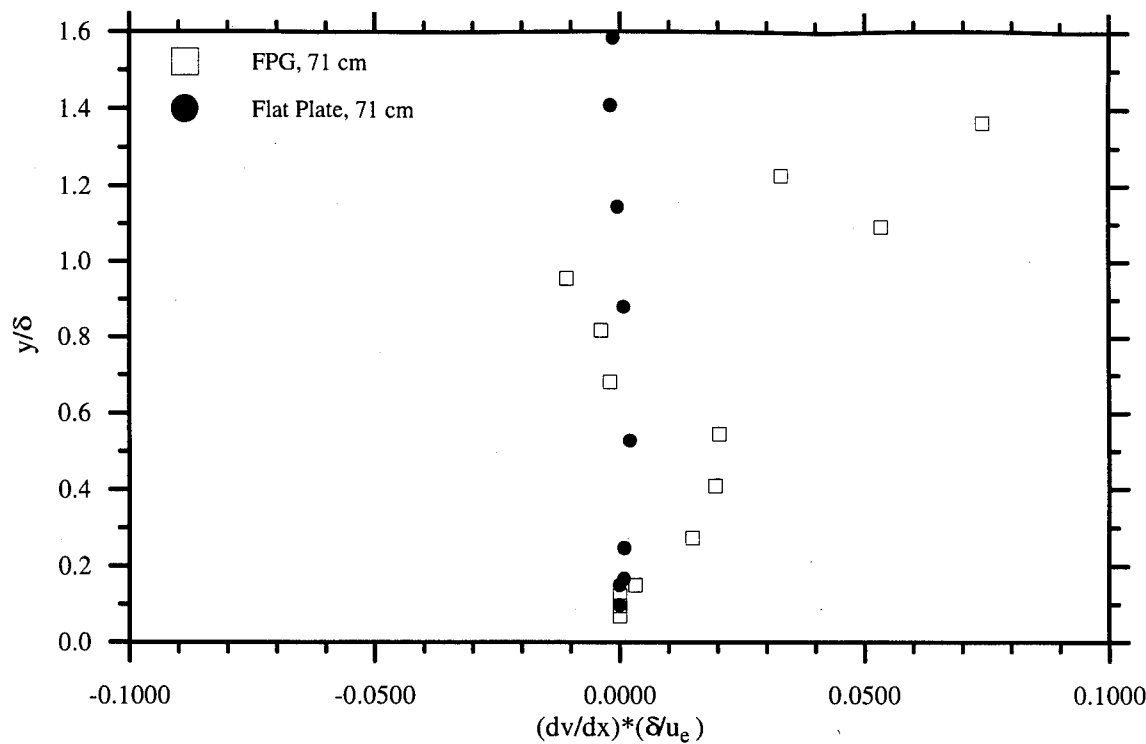


Figure 7-30: Simple Turbulence Model

The strain rates for the v-component of velocity are presented in Figures 7-31 and 7-32. The flat plate streamwise strain rate for both the u- and v-components was zero, as expected. The APG strain rate in Figure 7-30 exhibits an inflection point at  $y/\delta = 0.6$ , and increasing magnitude above the boundary layer edge. The flat plate strain rate in Figure 7-32 also has an inflection point, but closer to the boundary layer edge. The pressure gradient increased the strain rates for both v-component measurements.



## *8. Conclusions and Recommendations*

### *8.1 Conclusions*

An experimental investigation on the effects of adverse pressure gradient on the mean and turbulent flow structure of a Mach 2.9 boundary layer was performed. Laser Doppler Velocimetry was used to measure the mean and fluctuating velocity components, turbulence intensities, skewness, flatness, and intermittency in the axial and transverse directions.

The present study was conducted in the Air Force Institute of Technology Mach 3.0 wind tunnel. LDV profile measurements were made at the same location for a flat plate model, and compression ramp model that generated an adverse pressure gradient. In this manner, the effects of the pressure gradient could be distinguished from the effects of the flat plate boundary layer. LDV profile measurements were also made a few centimeters upstream of the location studied by Dotter [9]. It was determined that the 71 cm measurement station was in a region of favorable pressure gradient.

The flat plate LDV measurements were made for two reasons. The first reason was to provide enable comparison of the data from the present study with other accepted data from the literature. This comparison enabled validation of the technique used in the study. The second reason was to provide a means of distinguishing the effects of the pressure gradient on the turbulent boundary layer from those of the natural progression of the flat plate boundary layer.

Flat plate measurements were taken 44 and 71 cm downstream of the throat of the nozzle. The Mach number decreased from 2.87 at the 44 cm location to 2.79 downstream. The boundary layer thickness increased from 5.74 mm to 9.86 mm at these two stations. The flat plate turbulence results matched those of previous researchers quite well, as evidenced by Figures 7-4

through 7-7. The flat plate LDV results of the present study agreed very well with LDV results of other researchers [12, 19, 25]. The Reynolds shear stress approached the wall value, and did not exhibit the "roll off" in the turbulent shear stress, that was experienced in the previous LDV studies. This problems were avoided by aligning the optics with the mean flow, and using a Bragg cell to create moving fringes in the probe volume. At the  $x = 71$  cm location, the boundary layer was intermittently turbulent to within about  $y/\delta = 0.62$ .

Two Laser Doppler Velocimetry measurements profiles, located 68 and 71 cm downstream of the throat of the nozzle, were taken over the compression ramp model. At  $x = 68$  cm, the flow experienced an adverse pressure gradient. At the second location, the flow was expanding around the top of the model to generate a region of favorable pressure gradient. The mean flow compression ramp results indicate that the Mach number decreased from 2.72 at  $x = 68$  cm to 2.51 at the 71 cm station. The boundary layer thickness decreased from 9.09 mm to 7.48 mm between the two locations. When compared to the  $x = 71$  cm flat plate measurements, the Mach number and boundary layer thickness in the APG region decreased by 2.5% and 7.8%, respectively. In the FPG region, these quantities decreased by 10% and 24%, respectively, from the flat plate values. The change in boundary layer thickness and flow structure was observed with nanosecond shadowgraph and schlieren photography.

The pressure gradient turbulence results indicate that the turbulence intensities and shear stresses increased over the flat plate values. The u-component turbulence intensity in the APG region increased by 24% of the flat plate value, while in the FPG region increased it increased by 14%. The v-component turbulence intensities for both locations increased by 8.1% over the flat plate value. The Reynolds shear stresses increased by 190% and 67% over the flat plate values for

the APG and FPG regions, respectively. Thus, the FPG reduced the amplification of the turbulence intensities and turbulent shear stresses.

The skin friction estimate indicated that the skin friction was twice the flat plate value at the 68 cm location. Further downstream in the FPG region, the skin friction was almost identical to the flat plate value. In the APG region, the boundary layer was intermittently turbulent to within about  $y/\delta = 0.55$ . Thus, the adverse pressure gradient decreased the mean turbulent location as compared to the flat plate value. In the FPG region, the mean locations were surprisingly identical.

Based on the comparison of the hot-wire anemometry and LDV results, it appears that the turbulence transformation [9] used to extract the hot-wire turbulence data may not be valid for supersonic pressure gradient flow. The hot-wire and LDV results compare quite well for flat plate flow. But, large differences are evident for the pressure gradient region. The LDV technique directly measures the mean and fluctuating velocity components. Hence, the turbulence intensities and Reynolds shear stresses are directly acquired without the need for a transformation on the measured data.

As mentioned in Chapter 1, this investigation was designed to meet the criteria of Settles and Dodson [26]. Table 8-1 shows how each of the criteria were met.

Table 8.1: Settles and Dodson Criteria

Criteria	Compliance
Baseline Applicability	Mach 2.9 Flow
Simplicity	Simple Geometry Modeled in Ref. [14]
Specific Applicability	Compared to CFD Code [14] for Validation
Well Defined Experimental Boundary Conditions	Tables 7-1 through 7-3, Appendix C
Well Defined Error Bounds	Appendix A
Adequate Documentation of Data	Appendix B
Adequate Spatial Resolution	Figures in Chapter 7

## *8.2 Recommendations*

It is recommended that more LDV profile measurements are made at locations between the 68 cm and 71 cm stations. In this manner, the progression of the supersonic turbulent boundary layer may be more fully understood. Also, these results may be compared with CFD results [14] at the same location. Other compression ramp models, which generate higher magnitude adverse pressure gradients, may be studied and compared to this model. Lastly, an imposed adverse pressure gradient like the study of Smith and Smits [27] may be evaluated to distinguish the effects of streamline curvature and the pressure gradient.

## Appendix A: Error Analysis

This section gives estimates of the uncertainty of the measured and calculated quantities of the present study. This analysis follows the well-detailed error analysis of Luker [23].

With any experiment it is necessary to perform an error analysis to determine the validity of the results. The error of a computed quantity depends on the error of the measured quantities that were used in the computation. The absolute error,  $\Delta f$ , in the quantity  $f$  is determined by differentiating  $f$  by  $n$  dependent variables  $x_i$ :

$$\Delta f = \sum_{i=1}^n \left. \frac{\partial f}{\partial x_i} \right|_{f_o} \Delta x_i \quad (\text{A.1})$$

where  $f_o$  is the mean value of  $f$  around which the function is linearized. The error in  $f$  may be expressed as a percentage by using  $\epsilon_f \equiv \Delta f / f_o \times 100\%$ . Thus, Eqn. (A.1) becomes

$$\epsilon_f = \sum_{i=1}^n \left. \frac{\partial f}{\partial x_i} \right|_{f_o} \frac{x_{i_o}}{f_o} \epsilon_{x_i} \quad (\text{A.2})$$

Thus,  $\epsilon_f$  denotes the percent error in the function  $f$ . These equations give the maximum possible error assuming the errors are simultaneously at their maximum values. It is reasonable to expect that the errors are not all maximized at the same time. Thus, the Euclidean norm is used to determine the percent error:

$$\epsilon_f = \left[ \sum_{i=1}^n \left( \left. \frac{\partial f}{\partial x_i} \right|_{f_o} \frac{x_{i_o}}{f_o} \epsilon_{x_i} \right)^2 \right]^{0.5} \quad (\text{A.3})$$

Error calculations throughout this section will be estimated by Eqn. (A.3) unless otherwise indicated.

The error associated with the LDV velocity, temperature, and pressure measurements is given in the next section. Once these errors are defined, their influence on the calculated values is estimated.

#### A.1 LDV Velocity Error

The error in the LDV velocity measurements was attributed to four key sources. These sources included traverse position error, BSA error, angular alignment error, and repeatability error. The traverse error occurred because the BURSTware didn't accurately record the traverse position. For example, LDV measurements were made at the location  $y = 0.09$ ,  $z = -0.76$ . When moving the traverse to the next profile station, the software would read the traverse position as taking measurements at the location  $y = 0.09$ ,  $z = -0.75$ . Thus, the error in the traverse position would increase by 0.01 mm each time the traverse was moved. The location error associated with the  $i^{th}$  data location in the profile, in units of mm, was

$$\Delta y_i = \Delta y_o + 0.01(i - 1) \quad (\text{A.4})$$

where  $\Delta y_o$  is the origin placement error. The origin placement error was estimated by evaluating the possible uncertainty in the alignment of the optics with the wall. When the lasers were aligned with the wall, it was assumed that the "spot pattern" was placed within 25% of the radius of the spot's center. Thus, the angular error,  $\Delta\phi$ , was approximately  $4.3^\circ$  and the origin placement error,  $\Delta y_o$ , was 0.074 mm. This is a rather large error considering the rotation angles used for LDV measurements with the compression ramp test section.

The BSA error in the velocity measurements resulted from limitations in calculating the Doppler frequency. The frequency error of the BSA is [7]

$$\Delta f_D = \frac{n(BW)}{2^8 N} \quad (\text{A.5})$$

where  $N$  is the record length, and  $n$ , based on the bandwidth, were 1.2 and 1.5 for BSA #1 and #2, respectively. Thus the BSA errors for the  $u$ - and  $v$ -components of velocity were 0.095 m/s and 0.090 m/s, respectively.

The repeatability errors were determined by making twenty test runs in the wind tunnel (see Appendix C). The repeatability errors are given in Table A-1. The errors in the mean and fluctuating  $v$ -components of velocity were normalized by  $\bar{u}$ .

Table A-1: Repeatability Velocity Errors

$\epsilon_{\bar{u}}$	$\epsilon_{\bar{v}}$	$\epsilon_{u'}$	$\epsilon_{v'}$	$\epsilon_{\bar{u}'\bar{v}'}$
0.19 %	0.04 %	0.07 %	0.03 %	0.02 %

Another possible source of error was the off-axis angular alignment of  $3.5^\circ$ . Thus, the lasers were measuring a lower velocity component than the actual value. Based on the cosine of the off-axis angle, the actual velocity was 1.002 times the measured value. The resulting error, 0.2%, was ignored when compared to the magnitudes of the other errors.

The total velocity error at each measurement location in the profile is given by the Euclidean norm of each of those errors mentioned above:

$$\epsilon_{u_i} = \sqrt{\epsilon_{traverse,i}^2 + \epsilon_{BSA,i}^2 + \epsilon_{angle}^2 + \epsilon_{repeatability,i}^2} \quad (A.6)$$

The velocity error was calculated at each position in the profile. To simplify further error calculations, the velocity error was assumed constant and equal to the maximum error in the profile. Table A-2 presents the LDV velocity errors, where again the  $v$ -component velocity terms have been normalized by  $\bar{u}$ .

Table A-2: LDV Velocity Errors

$\epsilon_{\bar{u}}$	$\epsilon_{\bar{v}}$	$\epsilon_{u'}$	$\epsilon_{v'}$
8.1 %	8.1 %	2.0 %	8.0 %

### *A.2 Total Pressure and Temperature Errors*

The pressure and temperature were also recorded for each traverse location. The error in stagnation pressure was estimated as 0.3 % based on the fluctuation from the mean. Also, the maximum error in total temperature was estimated as 4.0 %. This estimate was based on the accuracy of the measured temperature, and the assumption of constant total temperature across the boundary layer.

### *A.3 Calculated Parameter Errors*

With the errors in the measured quantities (velocity, temperature, and pressure) determined, the next step was to estimate the errors of the calculated quantities, such as Mach number, intermittency, skewness, and boundary layer thickness. By substituting the previously defined errors into the data reduction equations of Chapter 6, the errors for the calculated quantities were determined. These errors, which were determined by the error analysis of Ref. [23], are summarized in Table A-3.

Table A-3: Error Summary

Variable	% Error
$\bar{u}$	8.1
$\bar{v}$	8.1
$u'$	2.0
$v'$	8.0
$\bar{u}'\bar{v}'$	8.2
$\bar{Q}$	8.0
$\bar{M}$	8.2
$\bar{p}_o$	0.6
$\bar{T}_{o,\infty}$	0.1
$\bar{T}_o$	4.0
$\delta_u$	28.0
$\delta_M$	28.0

Variable	% Error
$u_e$	1.3
$Q_e$	1.5
$\rho_e$	6.6
$T_e$	1.8
$p_e$	6.4
$M_e$	1.5
$\bar{T}$	11.7
$\bar{p}$	6.6
$\bar{\rho}$	13.5
$\tau_w$	17.0
$d\bar{u}/dz$	12.4
$d\bar{v}/dz$	12.0

Variable	% Error
$u_{RMS}$	2.0
$v_{RMS}$	8.0
$Sk_u$	8.5
$Sk_v$	33.9
$Fl_u$	11.3
$Fl_v$	45.3
$\gamma_u$	11.3
$R_{uv}$	11.6
$d\bar{u}/dx$	14.0
$d\bar{v}/dx$	14.0
$d\bar{u}/dy$	16.3
$d\bar{v}/dy$	16.3

## *Appendix B: Data Files*

This section includes a listing of the data sets from the present study. Included are the flat plate and APG processed data files used to generate the figures throughout this document. Table B-1 presents which data sets, given as Tables B-2 through B-8, were used in each figure. For example, the data files listed in Tables B-3 and B-4 were used in Figure 7-6. Due to the number of measurement stations for the flat plate case at  $x = 71$  cm, the data set has been presented in two separate tables (Tables B-3 and B-4). The  $y/\delta_u$  data column has been repeated in Table B-4 for convenient comparison. This section satisfies the criteria of Settles and Dodson [26], by providing documented and tabulated data in machine-readable form.

Table B-1: Tabulated Data by Figure Number

Figure(s)	Table(s)
7-1, 7-2, 7-3	B-2, B-3, B-4
7-4, 7-5, 7-6, 7-7	B-3, B-4
7-12, 7-13, 7-14, 7-15	B-2, B-3, B-4, B-6, B-7
7-16	B-2, B-3, B-4, B-6, B-7, B-8
7-17, 7-18, 7-19, 7-20	B-3, B-4, B-6, B-7
7-21	B-6, B-7
7-22, 7-23, 7-24, 7-25, 7-26, 7-27	B-3, B-4, B-6, B-7
7-28, 7-29	B-3, B-4, B-7
7-30	B-3, B-4
7-31, 7-32	B-3, B-4, B-7
C-1, C-2	B-3, B-4, B-5
C-3, C-4, D-1, D-2	B-6

Table B-2: Flat Plate,  $x = 44$  cm

$y$ (mm)	$y/\delta_M$	$\rho$ ( $\text{kg/m}^3$ )	Temp (K)	Mach #	M# <sub>maxing</sub>	$U_{\text{bar}}$ (m/s)	$U_{\text{bar}}/U_{\text{bar,ref}}$	$(U')_{\text{max}}/U_{\text{bar}}$	$u/\text{u}_{\text{bar}}$	$u/\text{u}_{\text{bar,ref}}$	$u/\text{u}_{\text{bar}}$	$u/\text{u}_{\text{bar,ref}}$	$u/\text{u}_{\text{bar}}$	$u/\text{u}_{\text{bar,ref}}$	
1	0.174228	0.12192	168.64	1.8947	0.30984	496.13	0.82011	0.092989	0.076261	-0.2661	2.5727	1.1661	1.1661	1.1661	
1.2	0.209913	0.1463	186.02	1.6277	1.976	0.31966	508.28	0.84019	0.088543	0.074393	-0.3933	2.6141	1.1476	1.1476	1.1476
1.4	0.243399	0.17068	191.58	1.5805	2.0426	0.32353	517.87	0.85604	0.084419	0.072266	-0.4447	2.5784	1.1635	1.1635	1.1635
1.7	0.292667	0.20141	150.34	2.1587	0.33050	553.17	0.88134	0.078229	0.068846	-0.7175	3.2676	0.91816	0.91816	0.91816	
2	0.348555	0.24383	209.85	1.4429	2.2536	0.33707	544.9	0.90072	0.072226	0.052265	-0.8242	3.4103	0.87021	0.87021	0.87021
2.5	0.45569	0.30479	225.18	1.3447	2.415	0.33714	563.46	0.93134	0.062768	0.058462	-1.1189	3.7165	0.80721	0.80721	0.80721
3	0.52283	0.36575	233.16	129.87	2.4957	0.31531	571.96	0.94546	0.054574	0.051768	-2.0349	9.0323	0.33214	0.33214	0.33214
4	0.69711	0.48767	2.2552	118.65	2.7121	0.23261	562.19	0.9789	0.033405	0.0327	-2.3164	10.3933	0.28866	0.28866	0.28866
5	0.87139	0.60959	264.94	114.29	2.8066	0.14935	569.89	0.99165	0.019439	0.019439	-3.1140	20.403	0.14704	0.14704	0.14704
6	1.0457	0.7315	268.19	112.9	2.8415	0.092288	602.32	0.99565	0.011509	0.011459	-2.8885	31.102	0.096458	0.096458	0.096458
7	1.2199	0.85342	269.06	112.54	2.8525	0.07765	602.96	0.9967	0.009216	0.0091855	-2.6837	60.65	0.049464	0.049464	0.049464
8	1.3942	0.97534	269.41	112.39	2.856	0.065036	603.22	0.99712	0.007776	0.0077377	-1.0573	15.124	0.19835	0.19835	0.19835
9	1.5685	1.0973	2.27181	111.4	2.874	0.061644	604.94	0.9998	0.007118	0.0071178	-0.2644	4.7974	0.62534	0.62534	0.62534
10	1.7428	1.2192	2.27224	111.22	2.8764	0.073297	605.25	0.99987	0.008967	0.008967	-0.7314	22.129	0.071917	0.071917	0.071917
11	1.9171	1.3411	0.277168	111.46	2.8681	0.06602	604.85	0.99982	0.007293	0.0072917	-0.525	12.444	0.24109	0.24109	0.24109

$V_{\text{bar}} \text{ (m/s)}$	$V_{\text{bar}}/u_{\text{edge}}$	$(V')_{\text{rms}}/u_{\text{edge}}$	$\nu$	Skewness	Flatness	$\tau_{\text{v}}/\tau_{\text{bar}}$	$\tau_{\text{v}}/\tau_{\text{edge}}$	$\tau_{\text{v}}/\tau_{\text{wall}}$	$R_{\text{in}}$	$TKE/u_{\text{bar}}^2$	$u_{\text{bar}} \text{ (m/s)}$	$u_{\text{eff}}/u$	$y^*$
42.144	0.0696644	0.0290201	0.1991	3.3673	0.0013673	7.74E-04	0.91309	0.41551	5.58E-03	38.333	21.404	142.63	
42.658	0.0705144	0.0363436	0.030537	0.2169	3.5228	0.0010598	6.52E-04	0.76958	0.32931	5.24E-03	11.683	22.042	171.15
42.157	0.069686	0.03177	0.027196	0.1539	3.3842	7.77E-04	5.11E-04	0.60332	0.38975	0.0045726	11.834	22.554	199.68
44.301	0.07323	0.03299	0.029075	0.1317	5.1269	9.04E-04	6.64E-04	0.78341	0.35089	4.15E-03	12.116	23.388	242.47
45.975	0.075998	0.0305376	0.0257504	0.5253	3.5485	0.0008662	6.91E-04	0.81551	0.39275	3.54E-03	11.96	24.042	285.26
47.903	0.079185	0.025623	0.023865	0.4737	3.02	3.65E-04	3.34E-04	0.39406	0.22682	2.63E-03	11.283	20.105	356.57
47.926	0.079223	0.023033	0.021777	0.5679	2.6747	0.0004057	3.96E-04	0.46759	0.32169	2.03E-03	10.561	25.66	427.89
50.303	0.083151	0.018443	0.018054	0.2421	13.276	1.91E-04	2.18E-04	0.25769	0.30931	8.98E-04	10.335	26.833	570.52
53.337	0.091473	0.01332	0.01332	0.8468	5.32E-05	4.64E-05	0.076579	0.20187	3.73E-04	0.5394	27.316	713.14	
59.316	0.097837	0.010516	0.010516	0.4089	4.9956	1.47E-05	1.83E-05	0.021594	0.112136	1.77E-04	9.3178	27.47	855.77
62.237	0.10288	0.012142	0.012142	-6.6554	141.74	8.16E-06	1.02E-05	0.012059	0.072673	1.91E-04	9.3777	27.511	998.4
62.133	0.10271	0.0095793	0.0095517	-1.9077	49.787	6.62E-06	8.31E-06	0.0098113	0.089104	1.22E-04	9.4769	27.527	1141
59.316	0.098805	0.010696	0.010696	-0.2519	249.77	4.70E-06	5.99E-06	0.0070701	0.061784	1.40E-04	9.2934	27.638	1283.7
57.523	0.095087	0.010526	0.010526	-7.8767	192.62	8.74E-07	1.12E-07	0.13264	0.956674	1.48E-04	8.5937	27.653	1426.7
54.92	0.090784	0.0078746	0.0078731	-0.1721	5.5872	4.33E-07	-5.53E-07	-0.00275724	8.86E-05	8.76555	27.631	1568.9	

Table B-3: Flat Plate, x = 71 cm (Part 1)

y (mm)	$y/\delta_0$	$\rho$ (kg/m <sup>3</sup> )	Temp (K)	Mach #	M#/ $Re_{\text{free}}$	$U_{\text{far}}$ (m/s)	$U_{\text{far}}/U_{\text{edge}}$	$(u')_{\text{far}}/U_{\text{far}}$	$(u')_{\text{far}}/U_{\text{edge}}$	u Skewness	u Flatness	%	
1.2	0.13177	0.11848	0.16338	185.11	0.27418	460.76	0.76998	0.10482	0.080712	-0.2803	2.6619	1.127	
1.3	0.14818	0.13442	0.16121	187.82	0.26941	456.58	0.76037	0.10487	0.079739	-0.2629	2.6994	1.1114	
1.4	0.15373	0.13823	0.16843	179.78	0.27371	472.63	0.78981	0.097307	0.076554	-0.2402	2.5746	1.1652	
1.5	0.17097	0.1551	0.16564	182.8	0.27159	467.92	0.77925	0.097761	0.076168	-0.2287	2.5568	1.1733	
1.6	0.17569	0.15798	0.17228	175.25	0.27968	482.48	0.80627	0.093767	0.075602	-0.3337	2.7026	1.11	
1.75	0.19947	0.18095	0.17158	176.48	1.799	0.27784	481.83	0.80242	0.093176	0.074766	-0.3425	2.6709	1.1232
1.8	0.19765	0.17773	0.17696	171.11	1.8508	0.27945	491.34	0.82109	0.088967	0.07305	-0.3839	2.822	1.0631
2	0.22796	0.2068	0.17633	171.52	1.8658	0.28188	492.49	0.82017	0.088558	0.072632	-0.415	2.813	1.0665
2.5	0.27452	0.24684	0.18968	159.64	2.009	0.28813	515.16	0.86089	0.078783	0.067824	-0.5227	3.0266	0.99121
3	0.34195	0.3102	0.19242	157.37	2.0651	0.29004	521.82	0.869	0.075339	0.065447	-0.6319	3.1669	0.9473
3.5	0.38433	0.34558	0.20724	146.11	2.2105	0.28875	541.99	0.90573	0.065581	0.059399	-0.7582	3.4069	0.88057
4	0.45593	0.4136	0.21268	142.37	2.2968	0.28004	551.28	0.91807	0.058934	0.054106	-0.8633	3.4906	0.85938
4.5	0.49414	0.44432	0.22273	135.95	2.3728	0.27033	561.36	0.9381	0.053171	0.04988	-1.0216	4.0848	0.73443
5	0.56991	0.517	0.22669	133.45	2.4475	0.26156	568.14	0.94615	0.04824	0.045642	-1.1665	4.4818	0.66937
5.5	0.60394	0.54306	0.23623	128.18	2.5074	0.24464	575.76	0.96216	0.042847	0.041226	-1.3525	5.2961	0.56645
6	0.68389	0.6204	0.23881	126.8	2.5681	0.22464	580.41	0.96659	0.037356	0.036108	-1.5129	5.9105	0.50247
6.5	0.71375	0.64179	0.24745	122.37	2.6146	0.21131	586.32	0.97981	0.033797	0.033115	-1.8001	7.6577	0.39176
7	0.79788	0.7238	0.24606	123.06	2.6397	0.20533	587.21	0.9779	0.032094	0.031385	-1.8296	7.6434	0.3925
7.5	0.82356	0.74053	0.25638	118.1	2.6973	0.16171	593.95	0.99256	0.024089	0.02391	-2.2166	11.065	0.27113
8	0.91186	0.8272	0.25451	119.17	2.7146	0.14512	594.19	0.98954	0.021269	0.021046	-2.321	12.195	0.24599
8.5	0.93337	0.83927	0.25639	118.1	2.7231	0.12514	593.96	0.99257	0.018141	0.018006	-3.2953	30.181	0.0994
9	1.0258	0.93059	0.25865	117.07	2.7571	0.10356	597.93	0.99576	0.014573	0.014511	-2.3802	15.925	0.18839
9.5	1.0432	0.93801	0.25897	116.93	2.7496	0.11025	596.04	0.99606	0.015596	0.015534	-2.5271	18.281	0.16411
10	1.1398	1.034	0.26095	116.04	2.779	0.079867	599.76	0.9988	0.010948	0.010948	-1.4895	15.386	0.19498
10.5	1.153	1.0367	0.26093	116.05	2.7696	0.090136	597.6	0.99866	0.012473	0.012456	-2.4761	22.908	0.13096
11	1.2538	1.1374	0.26155	115.77	2.7838	0.071168	600.23	0.9996	0.009694	0.009601	-1.9863	26.139	0.11477
11.5	1.2628	1.1555	0.26171	115.7	2.7779	0.070991	598.21	0.99968	0.009709	0.009709	-0.9118	7.9998	0.37501
12	1.3678	1.2408	0.26159	115.76	2.7835	0.059622	600.26	0.99964	0.00808	0.008071	-0.33883	5.4266	0.55283
12.5	1.3726	1.2242	0.26192	115.61	2.779	0.075181	598.38	0.99996	0.01027	0.01027	-4.0829	77.242	0.038839
13	1.4818	1.3442	0.26095	116.04	2.7769	0.054832	599.76	0.99881	0.007452	0.007431	-0.7545	15.108	0.19856
13.5	1.4824	1.333	0.26119	115.93	2.7719	0.055337	597.81	0.999	0.007594	0.007564	-0.2595	4.7504	0.63153
14	1.5958	1.4476	0.26033	116.31	2.7706	0.054918	599.27	0.99799	0.007523	0.0075079	-0.7833	16.509	0.18172

Table B-4: Flat Plate,  $x = 71$  cm (Part 2)

$y/\delta_0$	$V_{bar}$ (m/s)	$V_{bar}/U_{edge}$	$(V')_{max}/U_{bar}$	$(V')_{max}/U_{edge}$	v Skewness	$\tau_{xy}/\rho U_{bar}^2$	$\tau_{xy}/\rho U_{edge}^2$	$R_{uv}$	$TKE/U_{bar}^2$	$u_{rms}$ (m/s)	$u_{eff}/u^*$	$y^*$
0.13177	10.3	0.017213	0.041493	0.031948	0.0201	3.4639	8.04E-04	0.0295	0.45993	7.22E-03	29.316	19.417
0.14818	9.5631	0.015926	0.042734	0.032494	0.1445	3.203	0.0019484	7.67E-04	0.98103	0.43476	6.38E-03	27.332
0.15373	10.381	0.017348	0.040583	0.032053	0.1059	3.1904	0.001743	7.59E-04	0.97185	0.44139	6.00E-03	8.8906
0.17097	9.2678	0.015434	0.042689	0.033266	0.1374	3.272	0.0017408	7.39E-04	0.94592	0.41714	5.52E-03	9.0244
0.17569	10.396	0.017372	0.040994	0.032327	0.133	3.1984	0.0016011	0.0007456	0.95429	0.42587	4.50E-03	8.9037
0.19947	8.9868	0.014966	0.041661	0.03343	0.1353	3.4241	0.0016038	7.48E-04	0.95714	0.41317	3.29E-03	9.0136
0.19765	10.105	0.016886	0.039563	0.032485	0.2148	3.2478	0.0014807	7.32E-04	0.93745	0.42068	2.24E-03	8.3272
0.22796	8.2369	0.013717	0.040924	0.033565	0.243	3.3633	0.0014115	7.08E-04	0.90546	0.38946	1.50E-03	7.7452
0.27452	9.8718	0.016497	0.037316	0.032125	0.3277	3.3892	0.0012058	7.03E-04	0.89955	0.41017	9.77E-04	8.1086
0.34195	8.1675	0.013602	0.037608	0.032682	0.316	3.7158	0.0011322	6.94E-04	0.88872	0.3996	5.57E-04	7.9853
0.38433	9.2697	0.015491	0.033827	0.030638	0.4384	3.9535	8.81E-04	0.0006209	0.79469	0.39707	3.89E-04	7.7333
0.45593	8.5542	0.013913	0.030502	0.028801	0.6319	4.1838	6.35E-04	4.80E-04	0.61467	0.35311	2.81E-04	7.742
0.49414	9.2981	0.015538	0.028801	0.027018	0.5595	4.2503	5.29E-04	4.30E-04	0.55062	0.34568	2.15E-04	7.2792
0.56591	9.2564	0.015415	0.026032	0.02463	0.661	4.493	4.10E-04	3.52E-04	0.45003	0.32661	1.48E-04	7.0163
0.60394	9.752	0.016297	0.024217	0.023301	0.6802	5.6621	3.13E-04	2.84E-04	0.36304	0.30147	1.72E-04	6.9559
0.66389	10.394	0.017309	0.021966	0.021232	0.4983	6.4293	2.30E-04	2.16E-04	0.27696	0.28004	1.05E-04	6.615
0.71375	10.743	0.017953	0.020153	0.019746	0.5512	5.6279	1.64E-04	1.61E-04	0.20635	0.24032	7.32E-03	6.7132
0.79788	12.99	0.021633	0.019524	0.019993	0.8823	5.7098	1.47E-04	1.46E-04	0.1864	0.23401	6.60E-03	6.5491
0.82356	12.689	0.021205	0.016327	0.016206	0.575	6.4066	7.15E-05	7.48E-05	0.095772	0.18167	6.08E-03	6.1425
0.91186	14.026	0.0223358	0.015129	0.014971	0.4967	6.6521	4.85E-05	5.11E-05	0.065355	0.15111	5.60E-03	6.4975
0.95337	15.143	0.025305	0.014899	0.014879	-1.3246	30.199	1.24E-05	1.30E-05	0.016668	0.045725	4.25E-03	5.88823
1.02558	16.133	0.026868	0.012703	0.012649	-0.2047	16.188	1.96E-05	2.12E-05	0.02719	0.10602	2.67E-03	6.28885
1.0432	18.042	0.030315	0.012643	0.012593	0.1461	10.13	1.77E-05	1.89E-05	0.024151	0.089835	1.84E-03	6.2685
1.1398	17.916	0.029837	0.011556	0.011542	-0.7989	19.635	-6.20E-06	-6.81E-06	-0.008715	-0.048929	1.18E-03	6.1639
1.1553	19.619	0.032786	0.01173	0.011714	-1.0961	27.589	6.65E-06	7.17E-06	0.0091802	0.045436	8.96E-04	6.2736
1.2538	19.369	0.032256	0.010652	0.010648	-1.7714	43.722	3.13E-06	3.45E-06	0.0044193	0.030314	4.55E-04	6.1131
1.2628	20.994	0.035083	0.010662	0.010059	0.2299	5.5082	4.31E-06	4.67E-06	0.0059781	0.044091	2.68E-04	6.2505
1.3678	19.736	0.032868	0.010691	0.010087	-1.5873	38.623	-7.66E-07	-8.45E-07	-0.001082	-0.0093989	1.94E-04	6.0441
1.3726	20.533	0.034313	0.010929	0.010929	-3.6333	71.029	2.63E-06	2.86E-06	0.003656	0.023436	1.60E-04	6.0946
1.4818	19.387	0.032286	0.010035	0.010024	-2.7925	64.819	1.28E-06	1.40E-06	0.0017949	0.017066	1.34E-04	5.9564
1.4824	19.99	0.033406	0.0087174	0.0087087	-1.1066	32.773	7.71E-07	8.33E-07	0.0010668	0.01165	1.28E-04	6.0928
1.5958	18.078	0.030105	0.010053	0.010053	-3.0564	61.659	-5.95E-07	-6.49E-07	-8.30E-04	-0.0078349	1.29E-04	5.9603
												2005.3

Table B-5: Flat Plate,  $x = 71$  cm, 8 Samples

$y$ (mm)	$y/\delta_m$	$y/\delta_m$	$\rho$ ( $\text{kg}/\text{m}^3$ )	Temp (K)	Mach #	$M/\#_{\text{Reynolds}}$	$u_{\text{bar}}$ (m/s)	$u_{\text{bar}}/u_{\text{inlet}}$	$(u')_{\text{rms}}/u_{\text{bar}}$	$(u')_{\text{rms}}/u_{\text{bar}}$	$u$ Skewness	$u$ Flatness	$\gamma_u$
1.2	0.15545	0.10248	0.1657	182.74	1.7126	0.28399	467.1	0.78589	0.10461	0.082211	-0.1387	2.9165	1.0286
1.35	0.17489	0.11529	0.16907	179.1	1.7591	0.27957	475.14	0.79492	0.097543	0.079778	-0.286	2.7895	1.0755
1.5	0.19432	0.1281	0.17218	175.86	1.8026	0.28819	482.18	0.81126	0.096272	0.078102	-0.2646	2.9722	1.0094
1.65	0.21375	0.14091	0.17467	173.36	1.8359	0.28678	487.57	0.82033	0.092676	0.076025	-0.3505	2.9156	1.0289
1.8	0.23318	0.15372	0.17758	170.52	1.8745	0.29447	493.62	0.83051	0.091607	0.076081	-0.3673	3.0431	0.98584
2	0.25909	0.1708	0.18073	167.54	1.9154	0.29206	499.88	0.84104	0.087035	0.073427	-0.4317	2.9377	1.0212
2.5	0.32386	0.2135	0.19018	159.22	2.033	0.29133	517.01	0.86987	0.078786	0.067742	-0.5068	3.0318	0.98951
3	0.38863	0.2562	0.19896	152.19	2.1373	0.28182	531.08	0.89354	0.069846	0.06241	-0.6425	3.4252	0.87586
3.5	0.45341	0.2989	0.20681	146.42	2.2254	0.29625	542.38	0.91255	0.066345	0.060543	-0.8528	4.0089	0.74833
4	0.51818	0.3446	0.21254	142.46	2.2884	0.29424	549.99	0.92536	0.062553	0.057699	-0.1043	4.7567	0.63069
4.5	0.58295	0.38429	0.22122	136.88	2.3801	0.27997	560.58	0.94318	0.054699	0.051591	-1.1395	5.1026	0.58794
5	0.64772	0.42699	0.22648	133.7	2.4347	0.29614	566.53	0.95319	0.055206	0.052622	-1.7934	9.4802	0.31645
5.5	0.7125	0.46969	0.23299	129.96	2.5007	0.26689	573.44	0.96482	0.047336	0.045671	-1.7619	9.3764	0.31995
6	0.77727	0.51239	0.23801	127.22	2.5507	0.26136	578.46	0.97327	0.040476	0.042898	-2.1167	12.474	0.2405
7	0.90681	0.59779	0.24971	121.26	2.6628	0.21249	589.25	0.99142	0.032552	0.032273	-3.2434	25.59	0.11723
8	1.03644	0.68319	0.25496	118.76	2.7127	0.20295	593.71	0.99892	0.029762	0.02973	-5.2728	55.647	0.053912
9	1.1659	0.76859	0.24982	121.21	2.6745	0.20107	589.35	0.99158	0.02976	0.029509	-4.3783	42.755	0.070166
10	1.2954	0.85399	0.25425	119.1	2.7182	0.17266	593.12	0.99793	0.024514	0.024463	-5.0917	62.368	0.048102
11	1.425	0.93939	0.25664	117.99	2.7409	0.16602	595.1	1.0012	0.023503	0.023232	-6.8305	93.002	0.032257
12	1.5545	0.9248	0.25785	117.43	2.7516	0.20485	596.08	1.0029	0.028643	0.028726	-7.3686	81.323	0.036889
13	1.6841	1.1102	0.25917	116.83	2.7627	0.20769	597.14	1.0047	0.028843	0.028978	-7.652	87.234	0.03439

$v_{\text{bar}}$ (m/s)	$v_{\text{bar}}/u_{\text{inlet}}$	$(v')_{\text{rms}}/u_{\text{bar}}$	$\text{Skewness}$	$\text{Flatness}$	$\tau_{xy}/\rho u_{\text{bar}}^2$	$\tau_{xy}/\rho u_{\text{bar}}^2$	$\tau_{xy}/\rho u_{\text{bar}}^2$	$R_{\text{uv}}$	$TKE/u_{\text{bar}}^2$	$u_{\text{bar}}(m/s)$	$u_{\text{eff}}/u$	$y^*$	
9.2253	0.015538	0.046246	0.036344	-0.313	5.2811	5.15E-04	2.09E-04	0.26479	0.10654	7.61E-03	30.347	19.31	176.49
9.2978	0.015644	0.043409	0.034702	-0.0566	4.2319	0.0016376	7.02E-04	0.8827	0.38576	6.64E-03	8.5893	19.702	198.55
9.048	0.015223	0.04679	0.037959	-0.3815	5.5723	6.63E-04	2.98E-04	0.37708	0.14713	6.82E-03	2.2971	20.048	220.61
9.3847	0.015159	0.044077	0.036158	-0.1747	4.9385	0.001063	4.69E-04	0.59379	0.24435	6.24E-03	8.4244	20.316	242.67
9.4576	0.015912	0.046111	0.038295	-0.194	5.1961	3.51E-04	1.71E-04	0.21605	0.083183	6.32E-03	8.5278	20.619	264.73
9.6953	0.016312	0.043353	0.036462	-0.1024	4.6646	0.0011623	0.0005896	0.74596	0.30709	5.69E-03	8.779	20.934	294.14
9.2605	0.015581	0.041024	0.035685	-0.0827	5.27778	0.0010499	5.99E-04	0.75846	0.32863	4.72E-03	8.8611	21.814	367.68
8.6575	0.014566	0.04025	0.035965	-0.2109	6.2997	6.62E-04	4.17E-04	0.52807	0.23554	4.06E-03	8.3934	22.553	441.21
9.3099	0.015664	0.038533	0.034593	-0.1042	6.402	6.13E-04	4.19E-04	0.52963	0.24403	3.63E-03	7.7872	23.16	514.75
7.9526	0.013358	0.038464	0.035593	-0.3771	7.6727	2.13E-04	0.0001536	0.19433	0.088682	3.42E-03	7.8154	23.575	588.29
8.947	0.015053	0.032851	0.030985	-0.1334	7.2077	4.21E-04	3.29E-04	0.41593	0.23429	2.58E-03	7.8627	24.163	661.82
9.3499	0.015731	0.031282	0.029818	-0.2496	7.7828	0.0001531	0.000125	0.15815	0.088651	0.002024	7.4263	24.499	735.36
9.8697	0.016606	0.02854	0.027536	-0.3124	9.3292	0.0002118	1.82E-04	0.23061	0.15677	1.93E-03	7.4651	24.894	808.89
10.629	0.017883	0.027158	0.026432	-0.4447	10.224	1.73E-04	1.55E-04	0.19577	0.1445	1.71E-03	7.395	25.184	882.43
12.69	0.021351	0.022344	0.022152	-0.855	14.987	7.13E-05	6.95E-05	0.087819	0.098058	1.03E-03	7.1125	25.819	1029.5
14.255	0.023983	0.022439	0.022415	-2.008	23.887	1.12E-05	1.13E-05	0.014316	0.016784	9.46E-04	5.6423	26.086	1176.6
35.415	0.059586	0.021604	0.021422	-2.0336	26.825	8.15E-05	0.0000794	0.1046	0.12671	9.10E-04	7.1167	25.825	1323.6
35.287	0.059597	0.020587	0.020544	-2.5937	32.377	2.34E-05	2.35E-05	0.029679	0.046268	7.24E-04	7.9061	26.051	1470.7
35.027	0.058934	0.018585	0.018608	-2.5661	32.503	7.35E-06	7.50E-06	0.009494	0.017045	6.15E-04	7.5758	26.17	1617.8
34.107	0.057385	0.018756	0.01881	-2.9737	39.561	6.07E-06	6.25E-06	0.007968	0.011304	7.62E-04	7.409	26.229	1764.9
32.067	0.053953	0.018789	0.018877	-3.5149	42.899	-1.16E-05	-1.21E-05	-0.015277	-0.021464	274.2101	6.9935	26.294	1911.9

Table B-6: Adverse Pressure Gradient,  $x = 68$  cm

y (mm)	$y/\delta_0$	$y/\delta_M$	$\rho$ (kg/m <sup>3</sup> )	Temp (K)	Mach #	M#flameing	$U_{bar}$ (m/s)	$U_{bar}/U_{edge}$	$(U')_{ms}/U_{bar}$	$(U')_{ms}/U_{edge}$	u Skewness	u Flatness	%
1.7117	0.18825	0.17057	0.22911	186.4	1.7297	0.29788	472.87	0.79291	0.10801	0.08564	-0.3028	2.4306	1.2343
2.1347	0.23477	0.21271	0.23252	180.8	1.8007	0.33156	484.77	0.81287	0.11185	0.090921	-0.63668	3.0229	0.99242
2.5577	0.28128	0.24263	0.24986	170.51	1.9239	0.311801	505.69	0.84795	0.0949381	0.080031	-0.68779	3.0739	0.97596
2.9906	0.32889	0.298	0.24994	162.8	2.039	0.31715	521.02	0.87365	0.085337	0.074555	-0.8804	3.4122	0.8792
3.8464	0.42302	0.38328	0.26205	150.13	2.2209	0.28583	545.07	0.91397	0.065268	0.059653	-1.2035	4.5418	0.66053
4.7023	0.51714	0.46836	0.27132	140.02	2.3771	0.24654	563.49	0.94487	0.049287	0.04657	-1.6885	7.2162	0.41573
5.5482	0.61017	0.55286	0.27823	131.75	2.5139	0.1826	578.03	0.96925	0.032746	0.031739	-2.2288	11.11	0.27002
6.837	0.75191	0.68128	0.27519	125.82	2.6187	0.11296	588.29	0.98545	0.018882	0.018626	-3.2832	34.728	0.086386
8.5388	0.93907	0.85085	0.26139	122.2	2.6849	0.063271	594.09	0.99617	0.010328	0.010288	-1.3197	9.6861	0.30972
10.25	1.1273	1.0214	0.24278	120.45	2.7174	0.052906	596.5	1.0002	0.008573	0.0085748	-5.7767	139.64	0.021483
11.267	1.2391	1.1227	0.22979	120.28	2.7214	0.038692	596.77	1.0007	0.006436	0.0064403	-0.3353	7.0772	0.4239
13.664	1.5027	1.3616	0.1975	120.81	2.7117	0.040464	595.95	0.9993	0.006717	0.0067123	-5.6131	209.29	0.014335

$V_{bar}$ (m/s)	$V_{bar}/U_{edge}$	$(V')_{ms}/U_{bar}$	$(V')_{ms}/U_{edge}$	$v$ Skewness	v Flatness	$\tau_{xy}/\rho U_{bar}^2$	$\tau_{xy}/\rho U_{edge}^2$	$\tau_y/\rho U_{bar}^2$	$\tau_y/\tau_{wall}$	$R_{uv}$	TKE/ $U_{bar}^{1/2}$	$u_{rms}$ (m/s)	$u_{rms}/U_{bar}$	$y^*$
-0.3687	-6.18E-04	0.045923	0.036413	0.2862	3.3723	0.0029713	0.0016593	2.0896	0.59904	7.94E-03	29.514	23.51	313.65	
1.0158	0.0017033	0.048347	0.0393	0.4187	3.8759	0.0034547	0.0020579	2.5915	0.633886	8.59E-03	8.6308	24.21	391.15	
-1.4137	-0.0023705	0.037158	0.037158	0.6158	3.9207	0.0027229	0.0018459	2.3246	0.65985	6.37E-03	9.4691	25.469	468.65	
-3.2131	-0.0053818	0.041717	0.036446	0.6036	4.0142	0.0023395	0.0017304	2.1791	0.65717	5.38E-03	8.1738	26.414	547.98	
-5.8758	-0.0098526	0.035875	0.032788	0.9797	4.819	0.0015329	0.001301	1.6383	0.65468	3.42E-03	7.5772	27.944	704.8	
-9.8882	-0.016597	0.030609	0.028922	1.1267	6.1796	8.87E-04	8.33E-04	1.0492	0.58804	2.15E-03	6.7701	29.16	861.63	
-14.543	-0.024387	0.024722	0.023962	1.092	8.4848	4.32E-04	4.58E-04	0.57651	0.55801	1.15E-03	5.3751	30.15	1016.6	
-21.943	-0.036794	0.017739	0.017499	1.3968	9.5121	0.0001492	1.55E-04	0.19508	0.44545	4.93E-04	3.8639	30.867	1252.8	
-30.963	-0.05192	0.012467	0.012419	2.0302	35.039	3.26E-05	3.28E-05	0.041349	0.25556	2.09E-04	2.7098	31.279	1564.6	
-38.855	-0.065153	0.010415	0.010417	4.6607	98.922	8.20E-06	7.72E-06	0.091795	1.45E-04	1.8703	31.452	1878.3		
-41.772	-0.070043	0.0096794	0.00966859	3.6934	77.319	-8.11E-07	-7.24E-07	-9.12E-04	1.14E-04	1.4186	31.472	2064.6		
-42.075	-0.070552	0.0091657	0.0091592	1.1144	51.459	-2.43E-06	-1.86E-06	-0.0023396	-0.039463	1.07E-04	1.4239	31.413	2503.7	

Table B-7: Adverse Pressure Gradient,  $x = 71$  cm

$y$ (mm)	$y/\delta_a$	$y/\delta_m$	$\rho$ (kg/m <sup>3</sup> )	Temp (K)	Mach #	M#flameout	$u_{bar}$ (m/s)	$u_{bar}/u_{edge}$	$(u')_{rms}/u_{bar}$	$(v')_{rms}/u_{bar}$	$v$ Skewness	$u$ Skewness	$u$ Flatness	$\gamma$
1.2548	0.16778	0.14862	0.23893	187.47	1.6956	0.28297	464.78	0.80931	0.10523	0.08516	-0.3781	2.6647	1.1258	
1.4857	0.19865	0.17596	0.24425	182.93	1.7532	0.28324	474.68	0.82654	0.09932	0.08209	-0.3581	2.5221	1.1895	
1.7166	0.22952	0.2033	0.24866	179.24	1.8005	0.28941	482.54	0.84023	0.09682	0.08135	-0.4407	2.6499	1.1321	
2.8699	0.38254	0.33983	0.26859	163.86	2.0042	0.30327	513.69	0.89446	0.08322	0.07443	-0.9056	3.5241	0.85128	
4.0053	0.53555	0.47437	0.28747	151.15	2.1847	0.28465	537.94	0.93669	0.06599	0.06181	-1.4669	5.4708	0.54837	
5.1497	0.68857	0.6099	0.3005	142.14	2.3127	0.25706	553.39	0.96359	0.04875	0.04697	-1.8395	7.3985	0.40549	
6.2941	0.84158	0.74544	0.31105	136.11	2.4197	0.17822	565.37	0.98445	0.033196	0.03268	-2.7865	15.437	0.19434	
7.4385	0.99459	0.88097	0.31448	132.72	2.4764	0.11046	571.26	0.99447	0.019339	0.01923	-2.4874	18.396	0.16308	
8.5828	1.1476	1.0165	0.31381	131.36	2.5004	0.082716	573.7	0.9895	0.01404	0.014025	-1.8246	21.709	0.13819	
9.7272	1.3006	1.152	0.31068	130.88	2.5085	0.069657	574.34	1.0001	0.011643	0.011644	-2.9517	62.602	0.047922	
10.872	1.4536	1.2876	0.30663	130.94	2.5076	0.0638869	574.18	0.99979	0.010931	0.010929	-4.0711	112.24	0.026727	
12.006	1.6053	1.4219	0.30207	130.94	2.5076	0.058635	574.15	0.99973	0.009624	0.0096214	0.0489	3.708	0.80906	
13.15	1.7583	1.5575	0.29805	130.83	2.5094	0.064066	574.35	1.0001	0.010626	0.010627	-2.3781	49.427	0.060696	

$v_{bar}$ (m/s)	$v_{bar}/u_{edge}$	$(v')_{rms}/u_{bar}$	$(v')_{rms}/u_{edge}$	$v$ Skewness	$v$ Flatness	$\tau_{xy}/\rho u_{bar}^2$	$\tau_{xy}/\rho u_{edge}^2$	$R_{uv}$	$TKE/u_{bar}^2$	$R_{uv}$	$u_{edge}$ (m/s)	$u_{eff}/u$	$y^*$
10.141	0.017657	0.045405	0.036746	0.0166	3.1102	0.0015678	7.69E-04	0.92423	0.32813	7.60E-03	37.581	21.257	249.64
10.118	0.017618	0.046755	0.038645	0.0676	3.1827	0.0014149	7.40E-04	0.96086	0.3047	7.12E-03	8.81	21.79	295.57
9.8407	0.017135	0.046713	0.03925	0.1552	3.2722	0.0015339	8.43E-04	1.0343	0.33915	6.87E-03	7.9812	22.217	341.5
10.652	0.018547	0.042692	0.03765	0.5523	3.9372	0.0014208	9.56E-04	1.1727	0.40561	5.23E-03	8.0027	23.957	569.17
12.194	0.021233	0.034397	0.032219	0.8345	5.0709	8.70E-04	6.88E-04	0.84306	0.38336	3.36E-03	7.5554	25.369	796.84
16.407	0.028568	0.028881	0.02783	1.1301	6.6437	4.87E-04	4.25E-04	0.52158	0.34554	2.02E-03	7.3357	26.3	1024.5
20.008	0.03484	0.022274	0.021928	1.089	7.4754	1.70E-04	1.61E-04	0.19714	0.23027	1.05E-03	7.1304	27.039	1252.2
24.156	0.042062	0.017436	0.017344	0.1091	14.696	7.43E-05	7.25E-05	0.088862	0.22028	4.91E-04	6.8384	27.409	1479.8
27.879	0.048545	0.014358	0.014343	-0.2108	16.974	3.11E-05	3.05E-05	0.037427	0.15435	3.05E-04	6.7506	27.564	1707.5
31.74	0.05268	0.012516	0.012517	0.443	6.4742	8.44E-06	8.22E-06	0.010074	0.057923	2.24E-04	6.838	27.604	1935.2
32.904	0.057294	0.012991	0.012988	-3.1062	49.98	5.68E-06	5.45E-06	0.0066814	0.040111	2.28E-04	6.8664	27.594	2162.8
33.376	0.058116	0.013251	0.013247	-4.1999	66.185	8.89E-06	8.40E-06	0.010306	0.069688	2.22E-04	6.9351	27.592	2388.5
33.16	0.057741	0.012338	0.012339	-0.5834	5.3148	4.48E-06	4.19E-06	0.0051323	0.034188	2.09E-04	6.904	27.605	2616.2

Table B-8: APG, x = 71 cm, Single Component

y (mm)	$y/\delta_0$	$y/\delta_M$	$\rho$ (kg/m <sup>3</sup> )	Temp (K)	Mach #	M/ $f_{\text{friction}}$	$U_{\text{bar}}$ (m/s)	$U_{\text{bar}}/U_{\text{edge}}$	$(U')_{\text{max}}/U_{\text{bar}}$	$(U')_{\text{max}}/U_{\text{edge}}$	u Flatness	v Skewness	$\chi_u$
0.23087	0.030333	0.028926	0.19873	228.11	1.2028	0.22743	364.13	0.63489	0.4666	0.09311	0.7292	2.7837	1.0777
0.23087	0.030333	0.028926	0.18846	240.53	1.038	0.081612	328.92	0.57349	0.063025	0.036144	5.9286	42.033	0.071372
0.46174	0.060666	0.057853	0.18708	241.91	1.043	0.0049672	325.18	0.56697	0.0039111	0.002174	0.0061	3.9645	0.75672
0.46174	0.060666	0.057853	0.18704	241.96	1.043	0.0075963	325.21	0.56702	0.005982	0.0033919	6.5827	459.84	0.0065241
0.68264	0.08969	0.085531	0.20781	217.45	1.3329	0.25674	393.99	0.68695	0.42111	0.097626	-0.1932	2.5563	1.1736
0.91351	0.12002	0.11446	0.22361	201.75	1.5179	0.26571	432.17	0.75351	0.11983	0.090294	-0.21112	2.6161	1.1467
1.1444	0.15036	0.14338	0.23474	191.87	1.6371	0.27294	454.55	0.79253	0.10854	0.086024	-0.3036	2.6396	1.1228
2.2988	0.30071	0.28677	0.26147	170.86	1.9042	0.29724	498.93	0.86991	0.090484	0.078713	-0.6659	3.0135	0.99552
3.4331	0.45107	0.43015	0.283337	156.38	2.1035	0.29158	527.29	0.91936	0.073537	0.067607	-1.1666	4.384	0.68431
4.5775	0.60142	0.57554	0.30125	145.89	2.2589	0.25475	546.9	0.95356	0.055818	0.053226	-1.7378	6.5669	0.43048
5.7219	0.75178	0.71692	0.31554	138.13	2.3812	0.19255	560.97	0.97809	0.037893	0.037063	-2.4216	12.384	0.24224
6.8663	0.90213	0.86031	0.32223	134.1	2.448	0.1346	568.24	0.99076	0.025009	0.024778	-2.8971	20.074	0.14945
8.0106	1.0525	1.0037	0.32472	131.98	2.4838	0.0922	571.97	0.99727	0.016618	0.016573	-2.8639	34.424	0.087149
9.155	1.2028	1.1471	0.32278	131.65	2.492	0.076389	575.14	0.99931	0.013672	0.013663	-2.9512	51.946	0.057753
10.299	1.3532	1.2905	0.32	131.65	2.4928	0.064145	573.33	0.99963	0.011474	0.01147	-2.3421	55.829	0.054123
11.434	1.5022	1.4326	0.31769	131.48	2.4953	0.063813	573.54	0.99981	0.011389	0.011389	-3.894	97.639	0.030726
12.578	1.6526	1.576	0.31486	131.5	2.4949	0.061654	573.5	0.99993	0.011008	0.011007	-4.1969	119.1	0.025189

$V_{\text{bar}}$ (m/s)	$V_{\text{bar}}/U_{\text{edge}}$	$(V')_{\text{max}}/U_{\text{bar}}$	$(V')_{\text{max}}/U_{\text{edge}}$	$\tau_{xy}/\rho U_{\text{bar}}^2$	$\tau_{xy}/\tau_{\text{wall}}$	$R_{uv}$	$TKE/U_{\text{bar}}^2$	$R_{uv}$	$U_{\text{eff}}/U_{\text{bar}}$	$U_{\text{eff}}/U_{\text{edge}}$	$y^*$
0	0	0	0	0	0	0	0	0	1.08E-02	108.26	16.021
0	0	0	0	0	0	0	0	0	1.99E-03	-11.603	14.349
0	0	0	0	0	0	0	0	0	7.65E-06	1.0298	14.174
0	0	0	0	0	0	0	0	0	1.79E-05	34.939	14.176
0	0	0	0	0	0	0	0	0	1.01E-02	30.005	17.475
0	0	0	0	0	0	0	0	0	7.18E-03	19.608	19.391
0	0	0	0	0	0	0	0	0	5.89E-03	10.002	20.55
0	0	0	0	0	0	0	0	0	4.09E-03	22.942	459.01
0	0	0	0	0	0	0	0	0	2.70E-03	7.2908	24.548
0	0	0	0	0	0	0	0	0	6.6243	25.702	918.03
0	0	0	0	0	0	0	0	0	7.18E-04	5.9386	26.555
0	0	0	0	0	0	0	0	0	3.13E-04	5.2553	1147.5
0	0	0	0	0	0	0	0	0	0	27.004	13771
0	0	0	0	0	0	0	0	0	1.38E-04	4.8148	27.237
0	0	0	0	0	0	0	0	0	9.35E-05	4.5287	27.311
0	0	0	0	0	0	0	0	0	6.58E-05	4.4462	27.322
0	0	0	0	0	0	0	0	0	6.49E-05	4.4276	27.336
0	0	0	0	0	0	0	0	0	6.06E-05	4.4106	27.333
0	0	0	0	0	0	0	0	0	0	0	2522.6

## *Appendix C: LDV and Flow Field Quality Analysis*

### *C.1 8 vs. 16 Sample Record Length*

While learning to use the LDV system, various parameters were adjusted to determine which BSA settings would optimize the analysis. One of these adjustable, and user defined, parameters was the record length. Recall, the record length specified the number of samples used to generate a Fast-Fourier Transform of the Doppler signal. Each BSA was restricted to record lengths of 8, 16, 32, and 64 [7]. Record lengths of 32 and 64 samples were not used in the present study because the time required to sample the signal exceeded the traverse time of the particle. Thus, because of the high velocities the analysis was restricted to either 8 or 16 samples. The results of flat plate LDV measurements made at the same location with both 8 and 16 sample record lengths are presented in Figures C-1 and C-2.

Both record lengths gave close agreement on the mean flow measurements. The Mach number profile for both the 8 and 16 sample settings were very close, with the 8 sample record length predicting slightly lower velocities, and hence, slightly lower Mach number. The largest difference between the two record lengths was discovered upon comparison of the turbulence parameters. Figure C-2 shows a comparison of the u-component turbulence intensities for the flat plate. There is close agreement between the profiles below  $y/\delta = 0.4$ . As the measurement station approached the freestream, the 8 sample case predicted freestream turbulence intensities that were three times those given by the 16 sample case. This difference may be attributed to noise levels that were too high. Based on this analysis, only 16 sample record length LDV measurements were made after this discovery. The 8 sample data is only presented in this appendix.

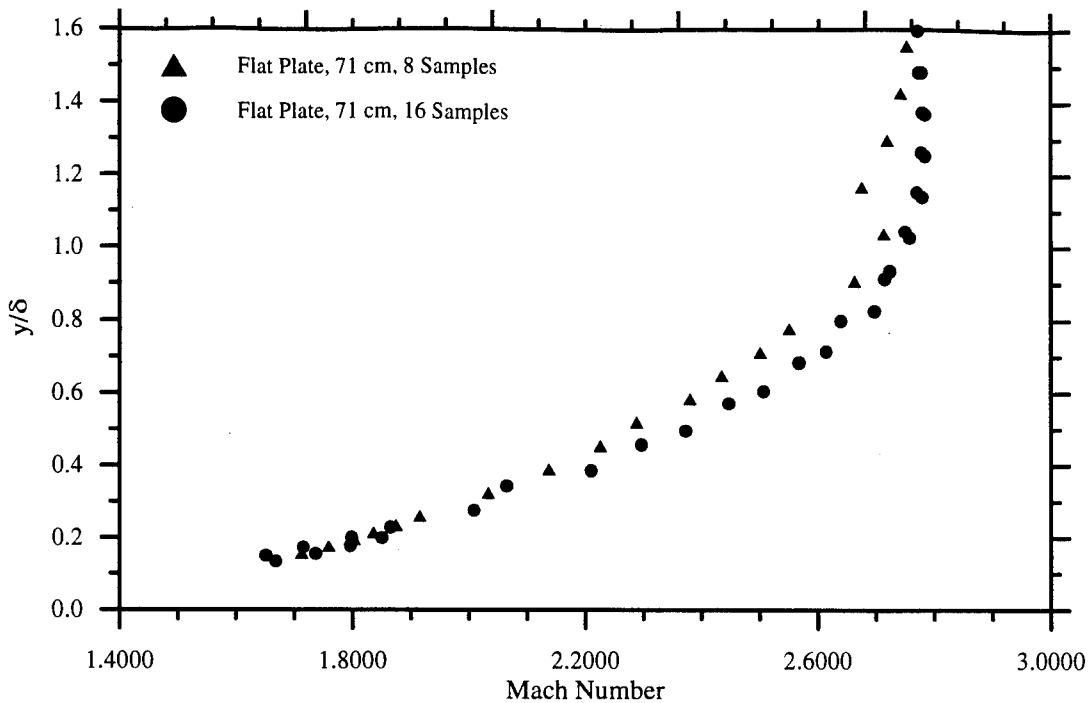


Figure C-1: Record Length Influence on Mach Number

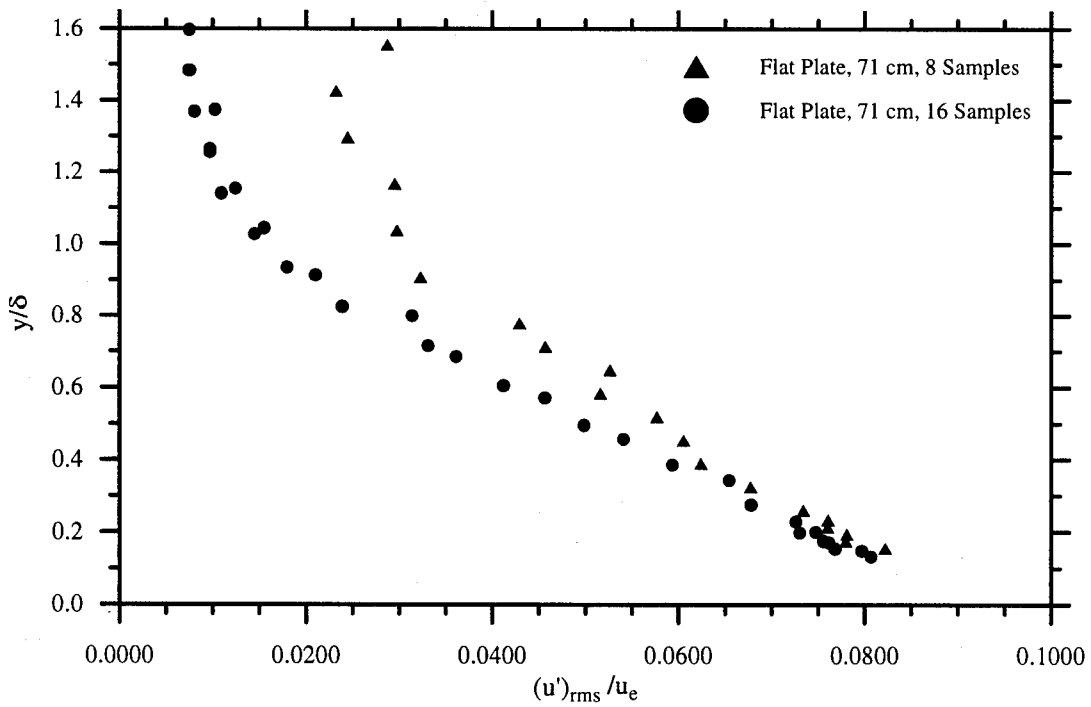
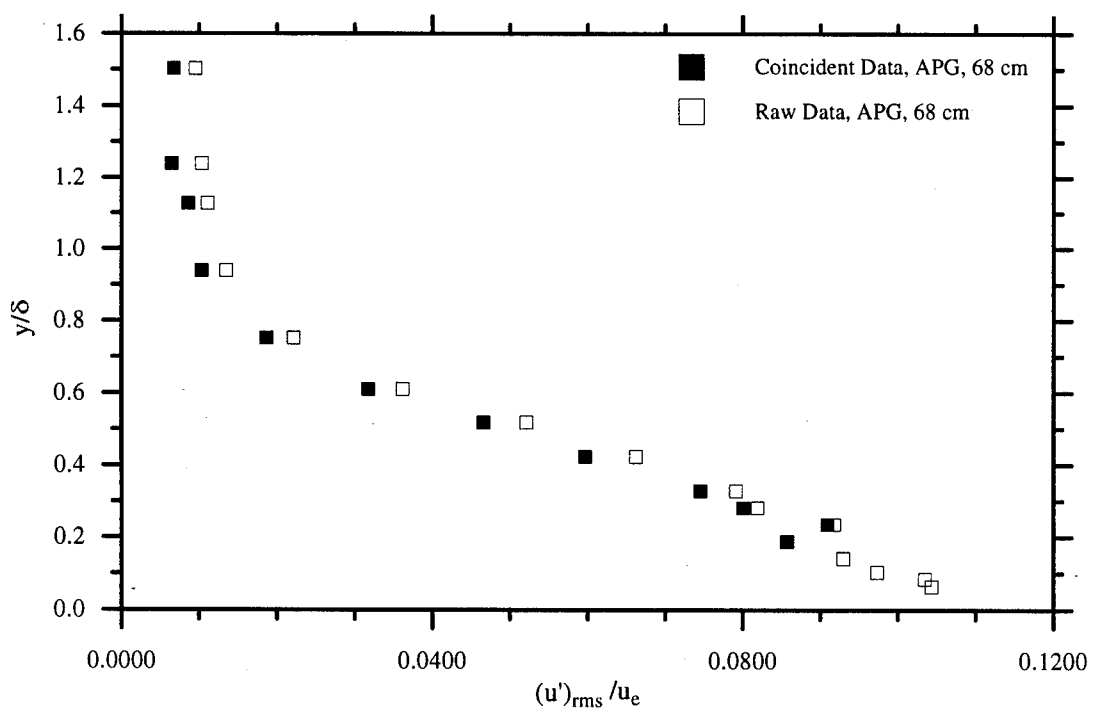
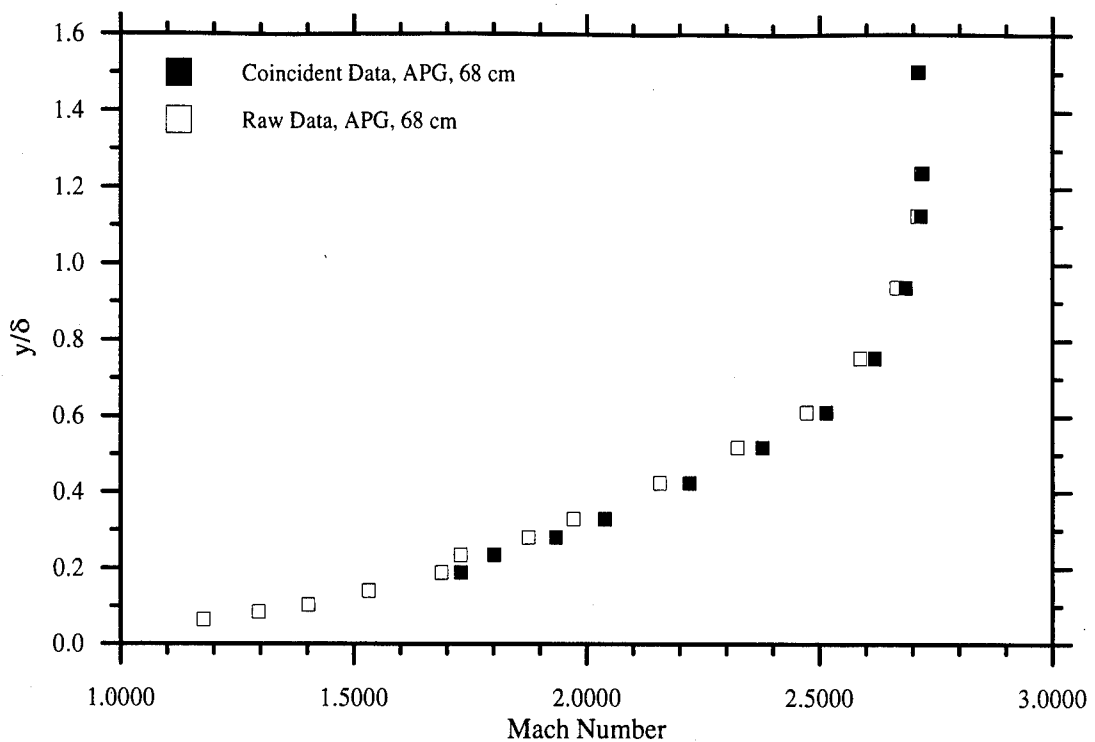


Figure C-2: Record Length Influence on Turbulence Intensity

### *C.2 Raw vs. Coincident Data*

As was mentioned in Chapter 3, coincidence filtering is a method of validating the Doppler signals. Coincidence filtering determines whether or not the BSA's are tracking the same particle. Raw data is the data that was collected by the BSA's. Coincident data is that which has passed the coincidence filtering criteria. Thus, the coincident data is a subset of the raw data. Therefore, the raw and coincident data were compared to determine if the coincident data were accurately representing the raw data.

Figures C-3 and C-4 present Mach number and u-component turbulence intensity comparison between the raw and coincident data. The profiles for both data are very similar. From the raw data, all turbulence statistics except  $\overline{u'v'}$  are calculated by the BURSTware. Because this term appears in the turbulent shear stress, it was necessary that the coincident data be used in the data reduction procedures of Chapter 6. In these figures, it appears as if the raw data LDV measurements were made closer to the wall than the coincident data. Actually, coincident data could not be calculated for the single component LDV measurements because only one component of velocity was measured, and the coincidence filtering process required comparison of the Doppler bursts received by two separate BSA's. These figures show that, in fact, the coincident data have the same trends as the raw data. Therefore, the coincident data may be used to present the processed results.



### C.3 Two-Dimensionality check

Another criteria for Ref. [26] is validation of two-dimensionality of the flow field. If the spanwise flow variations ( $du/dz, dv/dz$ ) are smaller than the order of the other strain rates, then two dimensionality of the flow field is verified. Strain rates in the spanwise, or w-direction, were in fact smaller than in the other directions.

LDV measurements were made at 5 mm on either side of the tunnel centerline for the strain rate measurements. These results are presented in Figures C-5 and C-6. The comparison of the fluctuating cross-correlation term,  $\overline{u'v'}$ , which was very sensitive to variations in the flowfield, is very good. In both cases, the agreement is remarkable. Thus, the flow was considered two-dimensional.

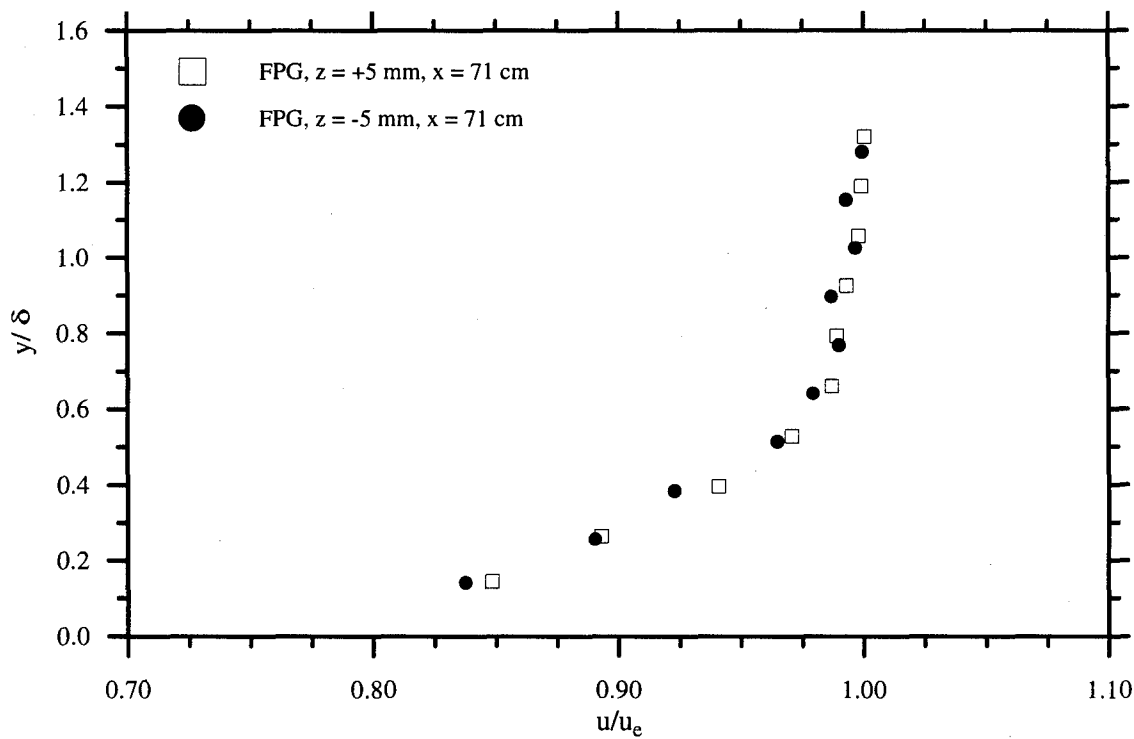


Figure C-5: 2D Comparison of Velocity Profiles

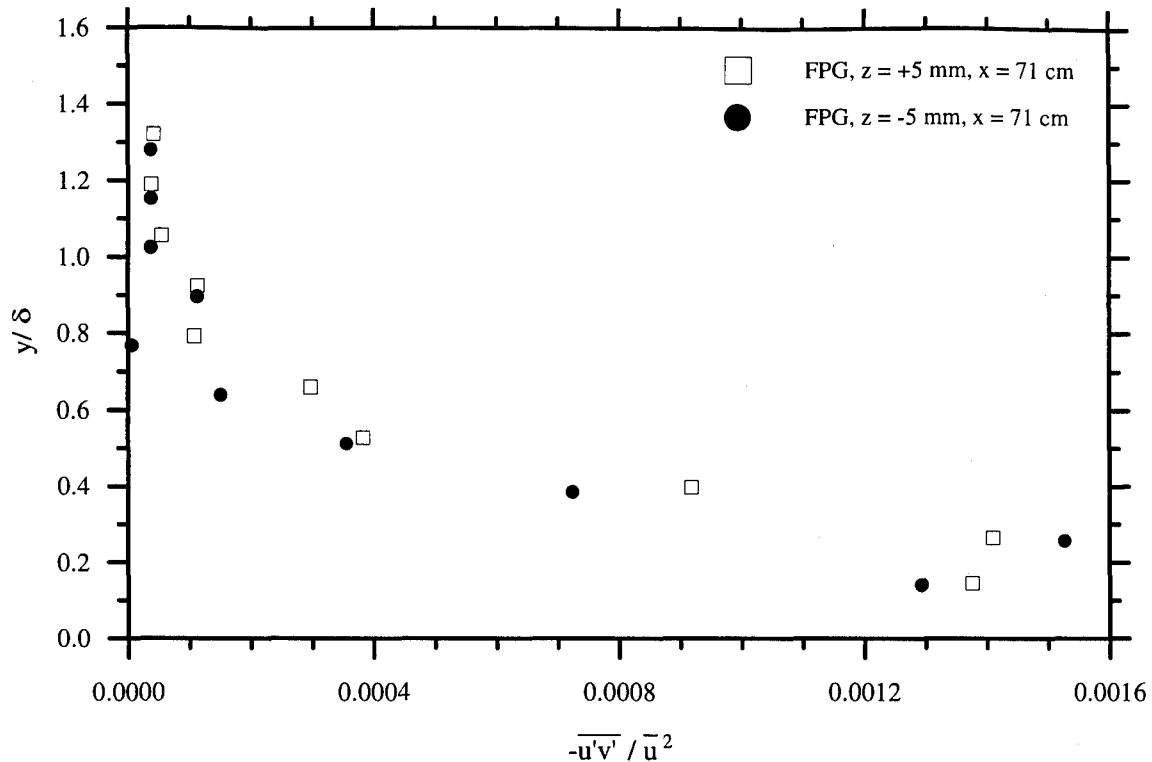


Figure C-6: 2D Comparison of Turbulent Shear Stresses

#### C. 4 Repeatability

Two methods were used to determine the repeatability of the present study. The first method was to compare different LDV measurement profiles, which were measured days, and even weeks apart. These  $x = 71$  cm flat plate profiles are presented in Figures C-7 and C-8. The agreement between the four test runs is very good, especially for the  $-\bar{u}'v' / \bar{u}^2$  term, which is very sensitive to flow variations.

For the second method of repeatability validation, confidence intervals for several of the mean flow and turbulence statistics were calculated. Twenty sets of data were taken at the same traverse location. Two of these sets were discarded because the mean velocity was much lower

than the remaining mean velocities. This probably occurred because data acquisition began before the tunnel had reached steady state.

A confidence interval is a measure of the probability that the error in the measured mean,  $\bar{x}$ , will be less than a certain value when compared to the actual value,  $\mu_x$  [2]. Thus, a 95% confidence interval of 5% indicates that there is a 95% probability that

$$\left| \frac{\bar{x} - \mu_x}{\bar{x}} \right| \leq 0.05 \quad (\text{C.1})$$

Because the value  $\mu_x$  was not known, the value of the confidence interval in Eq. (C.1) could not be directly calculated. Thus, to Student's t-distribution[2] was used:

$$\left| \frac{\mu_x - \bar{x}}{\bar{x}} \right| \leq \frac{st_{n,\alpha/2}}{\bar{x}\sqrt{N}} \quad (\text{C.2})$$

where  $N$  was the number of data points to calculate  $\bar{x}$ , and  $s$  was the standard deviation of  $x$ . The t-distribution was a tabulated function based on  $n = N - 1$  and  $\alpha$ , which described the accuracy of the confidence interval. Thus, for a 99% confidence interval,  $\alpha = 0.01$ . The results of the 99% confidence interval for the mean flow and turbulence statistics of the 18 valid data sets are presented in Table C-1.

Table C-1: Repeatability Confidence Intervals

Variable	Confidence Interval
$\bar{u}$	0.15%
$\bar{v}$	0.076%
$(u')_{rms}$	1.53%
$(v')_{rms}$	0.99%
$\bar{u}'\bar{v}'$	13.6%

Variable	Confidence Interval
$u$ Skewness	2.60%
$u$ Flatness	3.23%
$v$ Skewness	14.1%
$v$ Flatness	8.00%

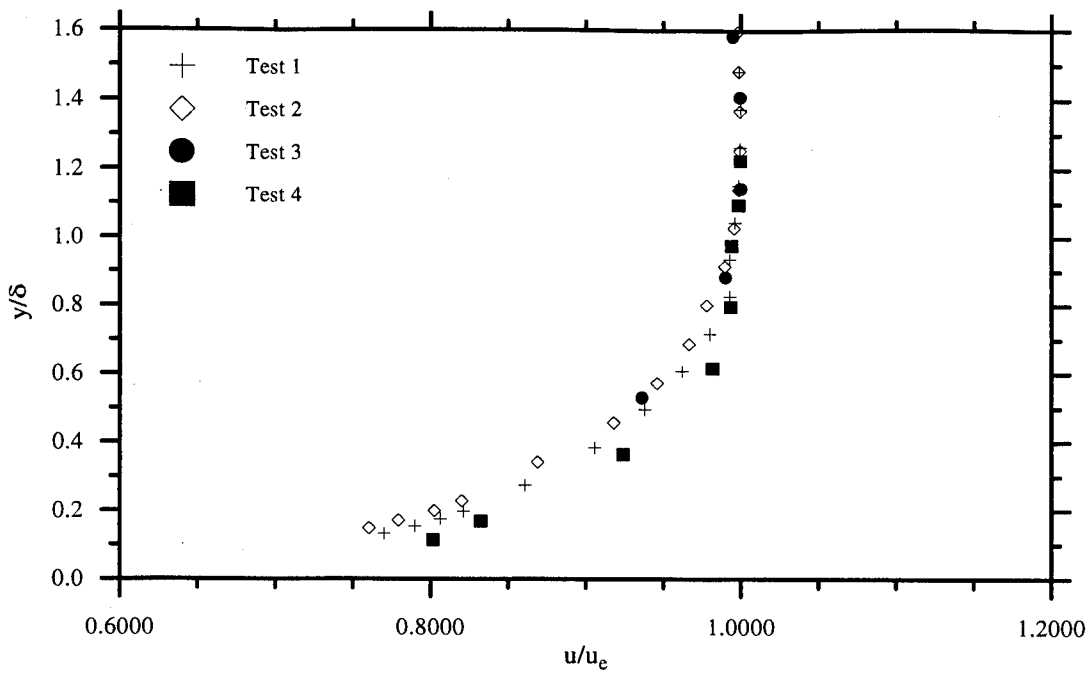


Figure C-7: Velocity Profile Repeatability Comparison

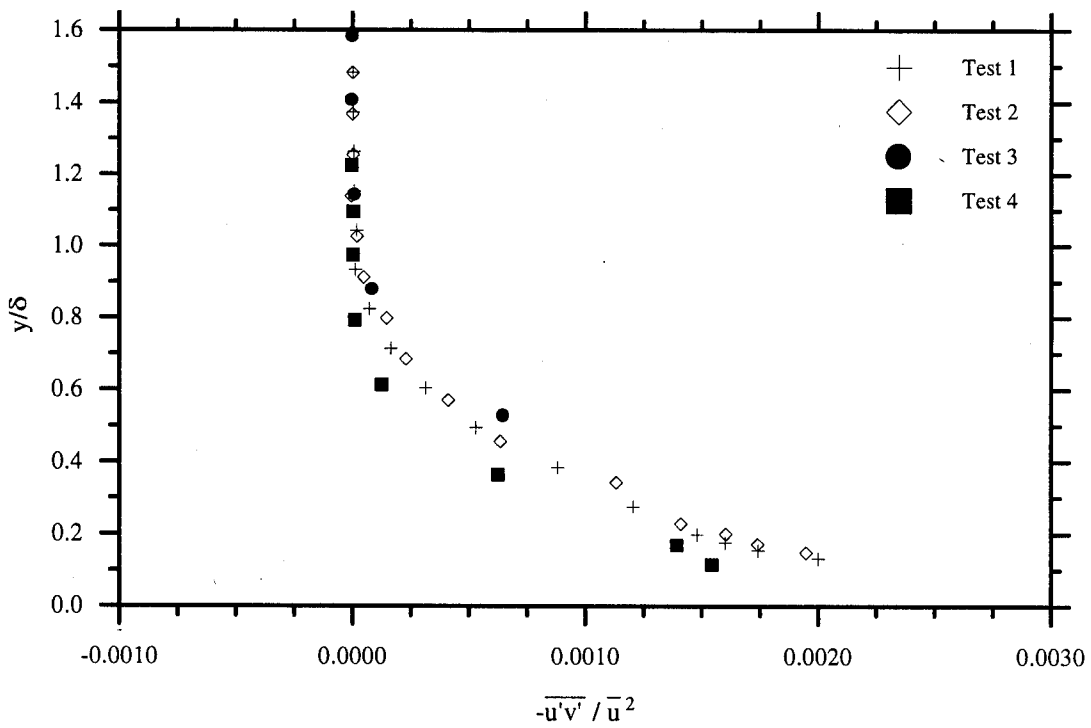


Figure C-8: Turbulent Shear Stress Repeatability Comparison

#### Appendix D: CFD Validation

As mentioned in Chapter 1, accurate empirical data is required to help validate turbulence models. The experimental LDV data of the present study were used by Fick[14] to validate a compressible turbulence model. He numerically studied the influence of pressure gradients on Mach 3.0 turbulent boundary layers generated by the same geometry as in the present investigation. Baldwin-Lomax and  $k-\omega$  turbulence models were used in a cell-centered finite volume flow solver to analyze the turbulent flow structure. Agreement between the experimental and numerical results of the  $k-\omega$  model was excellent for the flat plate and adverse pressure gradient cases[14]. The numerical results are presented in Figures D-1 and D-2. The numerical analysis predicted the velocity profile very well. The CFD analysis underpredicted the turbulent shear stress between 40% and 80% of the boundary layer thickness.

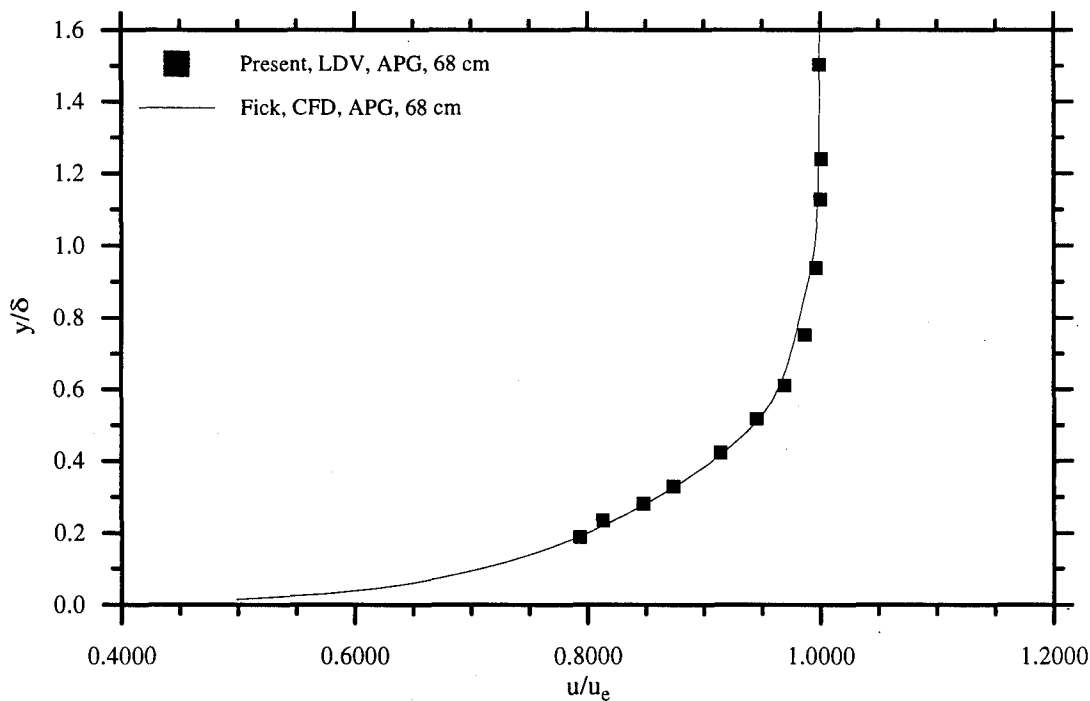


Figure D-1: LDV vs. CFD Velocity Profile

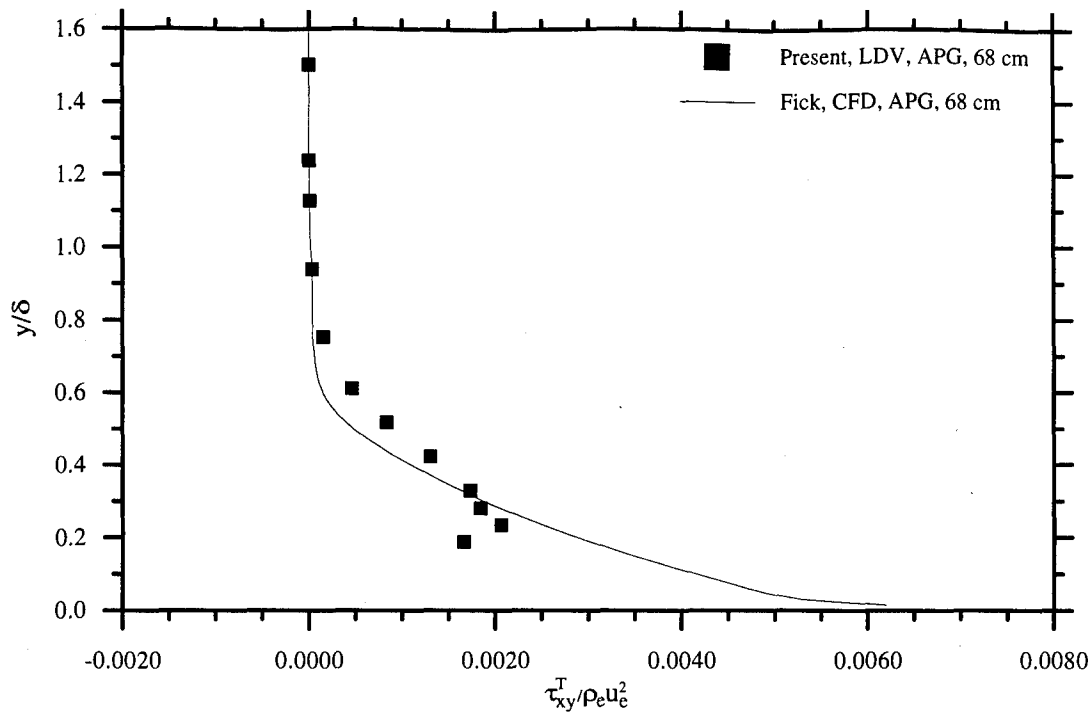


Figure D-2: LDV vs. CFD Turbulent Shear Stress

## Bibliography

1. Anderson, D. A., et al. *Computational Fluid Mechanics and Heat Transfer*. New York: McGraw-Hill, 1984.
2. Bendat, J. and A. Piersol. *Random Data Analysis and Measurement Procedures* (Second Edition). New York: John Wiley & Sons, 1986.
3. Bowersox, R. D. W. Course notes, AERO 827, Turbulent Flow. School of Engineering, Air Force Institute of Technology, Wright-Patterson AFB OH, Winter Quarter 1995.
4. Clauser, F. H. "Turbulent Boundary Layers in Adverse Pressure Gradients," *Journal of the Aeronautical Sciences*, Vol. 21: 91-108 (February 1954).
5. Dantec Measurement Technology. *BURSTware 2.00 User's Manual*. Skovlunde, Denmark, 1992.
6. Dantec Measurement Technology. *User's Guide 55x Modular LDA Optics*. Skovlunde, Denmark, 1992.
7. Dantec Measurement Technology. *User's Guide 57N20/57N35 BSA Enhanced*. Skovlunde, Denmark, 1992.
8. Dantec Measurement Technology. *User's Guide 60X Series FiberFlow*. Skovlunde, Denmark, 1992.
9. Dotter, J. *Compressible Turbulence Measurements in a Supersonic Flow with Adverse Pressure Gradient*. MS Thesis. School of Engineering, Air Force Institute of Technology (AU), Wright-Patterson AFB OH, December 1994.
10. Durst, F. , et al. *Principles and Practices of Laser-Doppler Anemometry* (Second Edition). London: Academic Press, 1976.
11. Elena, M. "Laser Doppler Anemometry in Supersonic Flows: Problems of Seeding and Angular Bias," AGARDograph-AG-315, Chap. 7, AGARD, 1989.
12. Elena, M. and LaCharme, J. "Experimental Study of a Supersonic Turbulent Boundary Layer using a Laser Doppler Anemometer," *Journal of Theoretical and Applied Mechanics*, Vol. 7, No. 2: 175-190 (1988).
13. Fernando, E. M. and A. J. Smits. "A Supersonic Turbulent Boundary Layer in an Adverse Pressure Gradient," *J. Fluid Mech.*, Vol. 211: 285-307 (1990).
14. Fick, E. T. *Numerical Simulation of Supersonic Turbulent Boundary Layer Flow Under the Influence of Mild Pressure Gradients*. MS Thesis. School of Engineering, Air Force Institute of Technology (AU), Wright-Patterson AFB OH, December 1995.

15. Huffman, R. E. *Mach 2.9 Investigation Into the Flow Structure in the Vicinity of a Wrap-Around Fin*. MS Thesis. School of Engineering, Air Force Institute of Technology (AU), Wright-Patterson AFB OH, December 1995.
16. Ion Laser Technology. *Ion Laser Technology Model 5500A Operations Manual*. Salt Lake City, Ion Laser Technology, 1993.
17. Johnson, D. A. "Laser Doppler Anemometry," AGARDograph-AG-315, Chap. 6, AGARD, 1989.
18. Johnson, D. A. "Turbulence Measurements in a Mach 2.9 Boundary Layer Using Laser Velocimetry," *AIAA Journal*, Vol. 12, No. 5: 711-714 (May 1974).
19. Johnson, D. A. and W. C. Rose. "Laser Velocimetry and Hot-Wire Anemometer Comparison in a Supersonic Boundary Layer," *AIAA Journal*, Vol. 13, No. 4: 512-515 (April 1975).
20. Kistler, A. L. "Fluctuation Measurements in a Supersonic Turbulent Boundary Layer," *The Physics of Fluids*, Vol. 2: 290-296 (May-June 1959).
21. Klebanoff, P. S. "Characteristics of Turbulence in a Boundary Layer with Zero Pressure Gradient," *National Committee for Aeronautics, Report 1247*. NASA-TN 3178, (July 1954).
22. Laderman, A. J. "Adverse Pressure Gradient Effects on Supersonic Boundary-Layer Turbulence," *AIAA Journal*, Vol. 18, No. 11: 1186-1195 (October 1980).
23. Luker, J. *Compressible Turbulence Measurements in a Supersonic Flow with Favorable Gradient*. MS Thesis. School of Engineering, Air Force Institute of Technology (AU), Wright-Patterson AFB OH, December 1995.
24. McLafferty, G. H. and R. E. Barber. "The Effects of Adverse Pressure Gradients on the Characteristics of Turbulent Boundary Layers in Supersonic Streams," *Journal of the Aerospace Sciences*, Vol. 29: 1-10 (January 1962).
25. Robinson, S. K., H. L. Seegmiller, and M. I. Kussoy. "Hot-wire and Laser Doppler Anemometer Measurements in a Supersonic Boundary Layer," *AIAA 16th Fluid and Plasma Dynamics Conference*. 1-10. in AIAA Paper (83-1723), (1983).
26. Settles, G. S. and L. J. Dodson. "Supersonic and Hypersonic Shock/Boundary-Layer Interaction Database," *AIAA Journal*, Vol. 32, No. 7: 1377-1383 (July 1994).
27. Smith, D. R. and A. J. Smits. "The Effects of Streamline Curvature and Pressure Gradient on the Behavior of Turbulent Boundary Layers in Supersonic Flow," *AIAA 25th Fluid Dynamics Conference*. 1-13. in AIAA Paper (94-2227), (1994).
28. Spina, E. F., A. J. Smits, and S. K. Robinson. "The Physics of Supersonic Turbulent Boundary Layers," *Annu. Rev. Fluid Mech.*, Vol. 26: 287-319 (1994).

29. Sturek, W. B. and J. E. Danberg. "Supersonic Turbulent Boundary Layer in Adverse Pressure Gradient. Part I: The Experiment," *AIAA Journal*, Vol. 10, No. 4: 475-480 (April 1972).
30. Sturek, W. B. and J. E. Danberg. "Supersonic Turbulent Boundary Layer in Adverse Pressure Gradient. Part II: Data Analysis," *AIAA Journal*, Vol. 10, No. 5: 630-635 (May 1972).
31. TSI Incorporated. *Model 9306 Six-Jet Atomizer Instruction Manual*, 1983.
32. Van Driest, E. R. "Turbulent Boundary Layers in Compressible Fluids," *Journal of the Aeronautical Sciences*, Vol. 18, No. 3: 145-160 (March 1951).
33. Waltrip, P. J. and J. A. Schetz. "Supersonic Turbulent Boundary Layer Subjected to Adverse Pressure Gradients," *AIAA Journal*, Vol. 11, No. 1: 50-57 (January 1973).
34. White, Frank M. *Viscous Fluid Flow* (Second Edition). New York: McGraw-Hill, Inc., 1991.
35. Wilcox, David C. *Turbulence Modeling for CFD*. La Cañada, California: DCW Industries, Inc., 1993.

*Vita*

Second Lieutenant Chad Stuart Hale [REDACTED] to Lt. Col. Gary C. and Kathy C. Hale. He graduated from Apple Valley High School in Apple Valley, Minnesota in June 1987. He attended two semesters at Brigham Young University in Provo, Utah on a full Air Force ROTC Scholarship. From September 1988 through August 1990, he served a Mandarin Chinese-speaking mission for the Church of Jesus Christ of Latter-Day Saints near Los Angeles, California. Lieutenant Hale resumed his undergraduate studies at BYU in September 1990. He married the former Camille Taylor in Idaho Falls, Idaho in August 1993. On 23 April 1994, he graduated with a Bachelor of Science degree in Mechanical Engineering and received his Air Force commission.

Lieutenant Hale entered the School of Engineering, Air Force Institute of Technology in May 1994. He completed three courses of study, which included Structural Analysis, Aircraft Aerodynamics, and Hypersonics. During the pursuit of this degree, Chad and Camille became the parents of a daughter, Taylor McKenzie, [REDACTED]. He completed his Master's degree in December 1995. His follow-on assignment is at Aeronautical Systems Center at Wright-Patterson AFB, OH.

VITA

# REPORT DOCUMENTATION PAGE

*Form Approved  
OMB No. 0704-0188*

Public reporting burden for this collection of information is estimated to average 1 hour per response, including the time for reviewing instructions, searching existing data sources, gathering and maintaining the data needed, and completing and reviewing the collection of information. Send comments regarding this burden estimate or any other aspect of this collection of information, including suggestions for reducing this burden, to Washington Headquarters Services, Directorate for Information Operations and Reports, 1215 Jefferson Davis Highway, Suite 1204, Arlington, VA 22202-4302, and to the Office of Management and Budget, Paperwork Reduction Project (0704-0188), Washington, DC 20503.

<b>1. AGENCY USE ONLY (Leave blank)</b>			<b>2. REPORT DATE</b> December 1995		<b>3. REPORT TYPE AND DATES COVERED</b> Master's Thesis	
<b>4. TITLE AND SUBTITLE</b>  EXPERIMENTAL INVESTIGATION OF A SUPERSONIC TURBULENT BOUNDARY LAYER WITH ADVERSE PRESSURE GRADIENT			<b>5. FUNDING NUMBERS</b>			
<b>6. AUTHOR(S)</b>  Chad S. Hale, Second Lieutenant, USAF						
<b>7. PERFORMING ORGANIZATION NAME(S) AND ADDRESS(ES)</b>  Air Force Institute of Technology 2750 P Street, WPAFB OH 45433-7765				<b>8. PERFORMING ORGANIZATION REPORT NUMBER</b>  AFIT/GAE/ENY/95D-12		
<b>9. SPONSORING/MONITORING AGENCY NAME(S) AND ADDRESS(ES)</b>  Dr. James McMichael/AFOSR/NA 110 Duncan Ave, Suite B115 Bolling AFB, Washington, D.C. 20332-0001				<b>10. SPONSORING/MONITORING AGENCY REPORT NUMBER</b>		
<b>11. SUPPLEMENTARY NOTES</b>						
<b>12a. DISTRIBUTION / AVAILABILITY STATEMENT</b>  Approved for public release; distribution unlimited					<b>12b. DISTRIBUTION CODE</b>	
<b>13. ABSTRACT (Maximum 200 words)</b>  Laser Doppler Velocimetry (LDV) measurements were made to quantify the effect of adverse pressure gradient on the compressible turbulent flow structure in a Mach 2.9 boundary layer ( $Re/m = 1.75 \times 10^7$ ). Measurements included profiles of 2-D mean velocities, turbulence intensities, Reynolds shear stresses, intermittency, flatness and skewness. In addition, mean strain rates were also measured. The boundary layer measurements were acquired for both flat plate and compression ramp models. LDV measurements were made at two locations on the compression ramp model at 68 cm and 71 cm downstream of the nozzle throat. At these locations, $\beta \approx 1.12$ and -0.94, respectively. Flow visualization was accomplished by nanosecond shadowgraph and schlieren photography. Results indicate that the adverse pressure gradient increased the Reynolds shear stresses by 190% and turbulence intensities by 24% of the flat plat values. In the favorable pressure gradient region, these quantities were decreased by 52% and 7% with respect to the adverse pressure gradient values, respectively.						
<b>14. SUBJECT TERMS</b> Supersonic turbulent boundary layers, Laser Doppler Velocimetry (LDV), Adverse pressure gradient, Mach 3.0, Compressible flow					<b>15. NUMBER OF PAGES</b> 140	
					<b>16. PRICE CODE</b>	
<b>17. SECURITY CLASSIFICATION OF REPORT</b> Unclassified	<b>18. SECURITY CLASSIFICATION OF THIS PAGE</b> Unclassified	<b>19. SECURITY CLASSIFICATION OF ABSTRACT</b> Unclassified	<b>20. LIMITATION OF ABSTRACT</b> UL			

## GENERAL INSTRUCTIONS FOR COMPLETING SF 298

The Report Documentation Page (RDP) is used in announcing and cataloging reports. It is important that this information be consistent with the rest of the report, particularly the cover and title page. Instructions for filling in each block of the form follow. It is important to **stay within the lines** to meet **optical scanning requirements**.

**Block 1. Agency Use Only (Leave blank).**

**Block 2. Report Date.** Full publication date including day, month, and year, if available (e.g. 1 Jan 88). Must cite at least the year.

**Block 3. Type of Report and Dates Covered.**

State whether report is interim, final, etc. If applicable, enter inclusive report dates (e.g. 10 Jun 87 - 30 Jun 88).

**Block 4. Title and Subtitle.** A title is taken from the part of the report that provides the most meaningful and complete information. When a report is prepared in more than one volume, repeat the primary title, add volume number, and include subtitle for the specific volume. On classified documents enter the title classification in parentheses.

**Block 5. Funding Numbers.** To include contract and grant numbers; may include program element number(s), project number(s), task number(s), and work unit number(s). Use the following labels:

C - Contract	PR - Project
G - Grant	TA - Task
PE - Program Element	WU - Work Unit Accession No.

**Block 6. Author(s).** Name(s) of person(s) responsible for writing the report, performing the research, or credited with the content of the report. If editor or compiler, this should follow the name(s).

**Block 7. Performing Organization Name(s) and Address(es).** Self-explanatory.

**Block 8. Performing Organization Report Number.** Enter the unique alphanumeric report number(s) assigned by the organization performing the report.

**Block 9. Sponsoring/Monitoring Agency Name(s) and Address(es).** Self-explanatory.

**Block 10. Sponsoring/Monitoring Agency Report Number. (If known)**

**Block 11. Supplementary Notes.** Enter information not included elsewhere such as: Prepared in cooperation with...; Trans. of...; To be published in.... When a report is revised, include a statement whether the new report supersedes or supplements the older report.

**Block 12a. Distribution/Availability Statement.**

Denotes public availability or limitations. Cite any availability to the public. Enter additional limitations or special markings in all capitals (e.g. NOFORN, REL, ITAR).

**DOD** - See DoDD 5230.24, "Distribution Statements on Technical Documents."

**DOE** - See authorities.

**NASA** - See Handbook NHB 2200.2.

**NTIS** - Leave blank.

**Block 12b. Distribution Code.**

**DOD** - Leave blank.

**DOE** - Enter DOE distribution categories from the Standard Distribution for Unclassified Scientific and Technical Reports.

**NASA** - Leave blank.

**NTIS** - Leave blank.

**Block 13. Abstract.** Include a brief (**Maximum 200 words**) factual summary of the most significant information contained in the report.

**Block 14. Subject Terms.** Keywords or phrases identifying major subjects in the report.

**Block 15. Number of Pages.** Enter the total number of pages.

**Block 16. Price Code.** Enter appropriate price code (**NTIS only**).

**Blocks 17. - 19. Security Classifications.** Self-explanatory. Enter U.S. Security Classification in accordance with U.S. Security Regulations (i.e., UNCLASSIFIED). If form contains classified information, stamp classification on the top and bottom of the page.

**Block 20. Limitation of Abstract.** This block must be completed to assign a limitation to the abstract. Enter either UL (unlimited) or SAR (same as report). An entry in this block is necessary if the abstract is to be limited. If blank, the abstract is assumed to be unlimited.